Technische Universität München

Fakultät für Chemie, Lehrstuhl für Anorganische und Metallorganische Chemie

Defect Engineering of Zr-based MOFs

Stefano Dissegna

Vollständiger Abdruck der von der Fakultät Chemie der Technischen Universität München zur Erlangung des akademischen Grades eines Doktors der Naturwissenschaften (Dr. rer. nat.) genehmigten Dissertation.

Vorsitzender:	Prof. Dr. Dr. h. c. Bernhard Rieger
Prüfende der Dissertation:	1. Prof. Dr. Dr. h. c. Roland A. Fischer
	2. Prof. Dr. Johannes A. Lercher

Die Dissertation wurde am 22/10/2018 bei der Technischen Universität München eingereicht und durch die Fakultät für Chemie am 20/11/2018 angenommen.

Defect Engineering of Zr-based MOFs

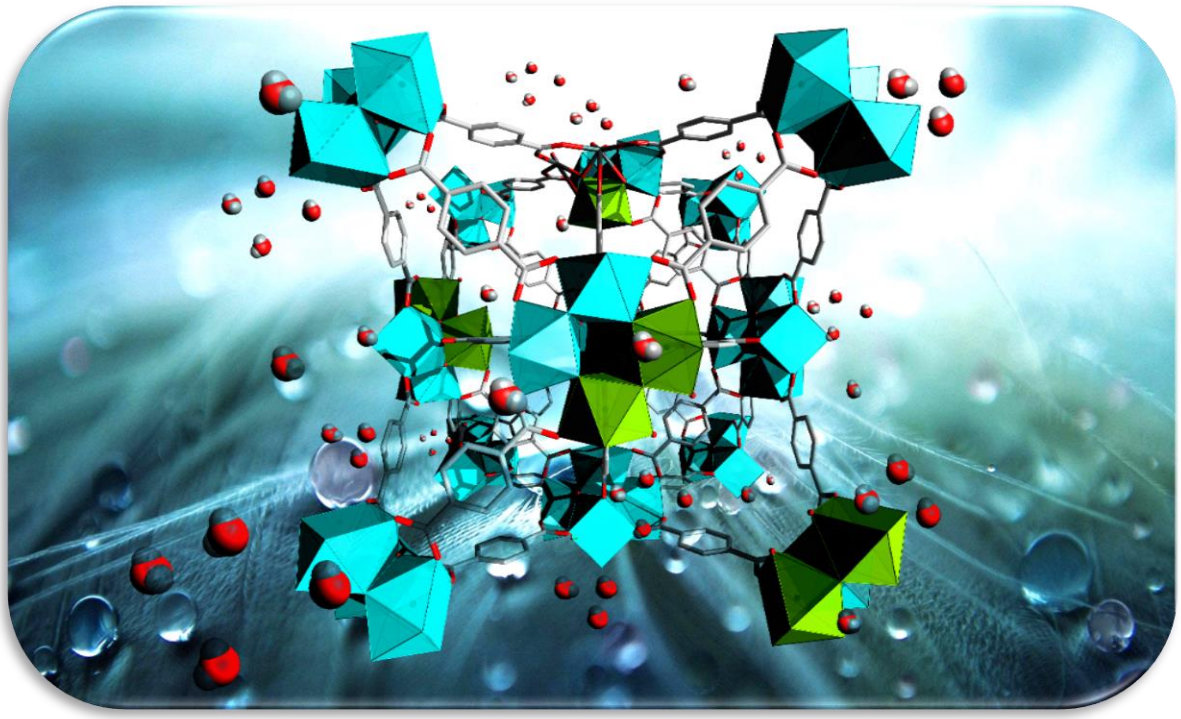

Dissertation

Submitted by

Stefano Dissegna

October 2018

Anhang I
Eidesstattliche Erklärung

Ich erkläre an Eides statt, dass ich die bei der Fakultät für Chemie der TUM zur Promotionsprüfung vorgelegte Arbeit mit dem Titel:

Defect Engineering of Zr-based MOFs

in der Fakultät für Chemie, Lehrstuhl für Anorganische und Metallorganische Chemie

unter der Anleitung und Betreuung durch Prof. Dr. Roland A. Fischer ohne sonstige Hilfe erstellt und bei der Abfassung nur die gemäß § 6 Ab. 6 und 7 Satz 2 angebotenen Hilfsmittel benutzt habe.

(X) Ich habe keine Organisation eingeschaltet, die gegen Entgelt Betreuerinnen und Betreuer für die Anfertigung von Dissertationen sucht, oder die mir obliegenden Pflichten hinsichtlich der Prüfungsleistungen für mich ganz oder teilweise erledigt.

(X) Ich habe die Dissertation in dieser oder ähnlicher Form in keinem anderen Prüfungsverfahren als Prüfungsleistung vorgelegt.

(X) Ich habe den angestrebten Doktorgrad noch nicht erworben und bin nicht in einem früheren Promotionsverfahren für den angestrebten Doktorgrad endgültig gescheitert.

Die öffentlich zugängliche Promotionsordnung der TUM ist mir bekannt, insbesondere habe ich die Bedeutung von § 28 (Nichtigkeit der Promotion) und § 29 (Entzug des Doktorgrades) zur Kenntnis genommen. Ich bin mir der Konsequenzen einer falschen Eidesstattlichen Erklärung bewusst.

Mit der Aufnahme meiner personenbezogenen Daten in die Alumni-Datei bei der TUM bin ich einverstanden,

Stefano Dissegna

Garching 10/10/2018

Acknowledgement

During the time of the PhD thesis I have faced many challenges, which gave me the opportunity to learn many different lessons. What I learnt in these three years, besides doing research, is that the cultural differences are big only if you want to make them big. I had the luck, thanks to my supervisor Prof. Roland A. Fischer, to be in an innovative European training program called DEFNET which allowed me to travel a lot and know wonderful people coming from all over the world. Thanks to this experience (and privilege) I have learnt that at the end of the story we are really all the same. It may sound predictable and cheesy, but when you get over with the stereotypes that every culture has, we all share the same goals and fears. I really believe that.

I have to say that my PhD experience was extraordinary, and I am not talking about research (that one let's say was good), but I am talking about all the colleagues that are part of the Chair of Inorganic and Metal-organic Chemistry. I have been probably in the best research group at TUM. The working atmosphere was one of the best I ever experienced among all other institutes I have been. Nice and comprehensive colleagues (well I can call them friends) with which you can share the sadness of a failed experiments (even little explosions), and a beer to celebrate a success, made this possible.

I want to thank the European Union for making projects like DEFNET possible.

I want to thank the colleagues at ITQ in Valencia starting from Xesc for the scientific support, Anna, Hans and Victor for the wonderful time and nice coffee breaks during the months I have spent there.

Also I want to thank all the colleagues in Augsburg and prof. Dirk Volkmer for the hospitality showed to the CRC refugees and for the nice time me and Rifan we had there.

I really want to thank again my supervisor, Prof. Roland A. Fischer for the motivation and trust that he gave me during these three years.

I also want to thank Prof. Johannes A. Lercher for accepting to be my second examiner.

Moreover, I would like to thank all the other colleagues from the Kuhn´s groups for sharing their coffee room in the moment of need, and of course for the crazy seminar room raves that they organize in these years.

I want to thank all AC1 members: Stefan, Joao, Michi, Konstantin, Emma, Shengyang, Werner, Julius, Kathrin, David, Fabian, Christian, Max, Lisa, Lena, Dardan, Pia, Zheng, Zhenyu, Raghav, Zahid, Margit, Patricia, Maxi, Dominik and Sebi.

I also want to thank the “non-scientific” members Rodica, Toby, Maria, Gabi and Martin for the enormous help that they gave me in dealing with the non-so friendly German bureaucracy.

I want to thank the “hateful eights” Mirza, Christian, Gabi, Alex, RiFi, Gregor, Markus and RoFi for all the scientific discussion/ seminars/1o1talks/ suggestions and help in general they gave me. They certainly contribute in solving many scientific problem with their suggestions.

I want to thank, in particular, Werner, Zahid and Konstantin for their help in- and outside the University, nice evenings/weekend/road trips and for their precious friendship.

Furthermore, I want to thank my family for the support that they gave me during all these years. I really have to thank them for the strength they were able to infuse me that allowed me to finish this important chapter of my life.

Finally, I want to thank my girlfriend Irene for her continuous and endless support. Without her encouragement, motivation and patience, in all these years, I could not complete this thesis and be the person that I am today.

Stefano Dissegna

Per la mia famiglia e per Irene

“Nel mezzo del cammin di nostra vita
mi ritrovai per una selva oscura,
ché la diritta via era smarrita.”

Dante Alighieri, Divina commedia, Inferno, Canto I.

Table of Contents

List of Figures

List of tables

List of abbreviations

AA	Acetic acid
BDC	Benzene dicarboxylic acid / terephthalic acid
BDC^{2-}	1,4-benzenedicarboxylate
BET	Brunauer- Emmet-Teller
BPDC	Biphenyl-4,4-dicarboxylic acid
bpy	4,4-bipyridine
BTC^{3-}	1,3,5-tricarboxylate
CE	Conventional electrical
CN	Coordination number
CP	Coordination polymers
CWA	Chemical warfare agents
DFA	Difluoro acetic acid
DMMP	Dimethyl methylphosphonate
DMF	Dimethylforamide
DRIFTS	Diffuse reflectance infrared Fourier transform spectroscopy
DUT	Technische Universität Dresden
EPR	Electro paramagnetic resonance
EXAFS	Extended x-ray absorption fine structure
FA	Formic acid
HIF-3	Hydrogen bonded imidazole framework
HKUST	Hong Kong University of Science and Technology
HPPXRD	High pressure powder x-ray diffraction
ICP	Induced coupled plasma
IFP	Imidazole framework potsdam
IRMOF	Isopreticular metal-organic framework
IUPAC	International union of pure applied chemistry
MIL	Material of the institute Lavoisier
MMPA	Methy methylphosphgonate
MOFs	Metal-organic frameworks
MPV	Meerwein-Ponndorf-Verley

MW	Microwave assisted
NPs	Nanoparticles
NTE	Negative thermal expansion
NU	North-Western University
PALS	Positron annhilation spectroscopy
PCN	Porous coordination network
PDF	Pair distribution function
PXRD	Powder x-ray diffraction
$pydc^{2-}$	pyridine-3,5-dicarboxylate
ROX	Roxarsone
RUMs	Rigid unit modes
SALE	Solvent assisted linker exchange
SALI	Solvent assisted ligand incorporation
SEM	Scanning electron microscopy
STEM	Scanning trasmission electron microscopy
TBAPy4	1,3,6,8-tetrakis(p-benzoate)pyrene
TEM	Transmission electron microscopy
TFA	Trifluoro acetic acid
TGA	Thermogravimetric analysis
TPDC	Terphenyl-4,4-dicarboxylic acid
UiO	Universitetet i Oslo
VTXRD	Variable temperature x-ray diffraction
ZIF	Zeolitic imidazolate framework

1 Motivation

"Defect" is a word that has its origin in Latin, where the verb "deficiere" ("de-" meaning "reversal" + "facere" meaning "do") was used to define the action of abandoning a country or a cause in favour of an opposing one. During the Roman Empire, when having a successful military career was a pre-requisite to become a ruler or have any influence in politics, "deficiere" had a negative use. Later in time, with the influence of ancient French, "defect" started to be used as a noun and acquired the meaning that it has today; however, during the centuries, the word kept the original negative connotation. In science, and more general in nature, "defect" acquired also a neutral or positive feature.

It was the discovery of the chemical structure of beautiful materials such as gemstones to finally give a neutral or positive connotation to the concept of "defect". Corundums, better known as ruby or sapphires, have the general formula α-Al_2O_3 but what gives them their beautiful colours is the presence defects in the crystalline framework. These are considered precious, beautiful and yet, these stunning colours are given by defects; where different impurities are trapped inside the gemstone crystal structure. If the impurity is Cr then a gemstone will acquire red colour and will be commonly called ruby. On the contrary, if other metals like Ti and Fe replace some of the Al atoms then the gemstone will acquire a stunning deep blue colour and would be called sapphire.

These processes of "defect engineering" occurs naturally but we can reproduce them artificially for many other crystalline materials. The targeted incorporation of defects into crystalline materials is at the core of material science. For instance, defects are systematically introduced in Si to produce semiconductors that are essential in computer chips. A stunning example is steel where C is added to Fe in order to improve the material performance under mechanical stress. Having these remarkable examples in mind, is it apparent that defects can significantly affect material properties. This is also true for metal-organic frameworks (MOFs), a new class of porous crystalline materials where defects were recently shown to alter their reactive properties such as catalysis and gas adsorption. Every year, different ways to include defects in MOFs and many intriguing properties related to them are discovered. However, little has been done to uncover the relationship between defects and material properties. An explanation to this is the intrinsic difficulty to characterize them which force scientists to use a plethora of different characterization

techniques. This, added to the novelty of the research field, makes this topic challenging but at the same time interesting with many open questions, which for the purposes of this thesis were divided in two milestones (M1 and M2):

M1: Understanding which type of defects are present in MOFs and gain control over their incorporation.

- Which type of defects are present in MOFs?
- Can we achieve control over defects incorporation?
- Which is the best way to incorporate defects?

M2: Understanding the impact of defects in MOFs reactive properties.

- How do they impact their physical and chemical properties?
- Do defects have only a beneficial effect on MOFs?

These are questions at the core of this thesis, which main task is trying to give an answer or at least give hints to other scientists that will work in this field. To address these questions, defects were successfully artificially introduced in two different MOFs, and the resulting materials were characterized by water adsorption, high pressure powder x-ray diffraction and variable temperature x-ray diffraction. These techniques allowed us to correlate the catalytic activity of the material with its hydrophilicity and explaining the impact of defects on mechanical stability. It is worth to mention that, uncover the influence of defects on activity and stability, is extremely important since these two parameters define a catalyst if it is suitable or not for industry.

In conclusion, research on defective MOFs is still making its first steps towards and industrial application. Therefore, is no surprise that every year new properties related to defective MOFs are discovered, and maybe, one of them might become a game changer in applied science.

2 General Introduction

2.1 Defects in crystalline solid materials

Crystals are made from the infinite periodic repetition of identical groups of atoms resulting in a symmetric 3D lattice. This nearly perfect formation process is favoured around 0 K, but it is not respected under real conditions.[1] Perfect crystals do not exist in nature and there is a fundamental reason why. While a perfect crystalline structure may be preferred energetically at absolute temperatures, all of the crystals present on Earth are formed at much higher temperatures. The presence of defects becomes more likely at these conditions and, as crystals are relatively immobile solids, it is difficult to eliminate whatever imperfections are introduced during their growth. The fact that real crystals are not perfect is critical in applied sciences. Intuitively, scientist tried to make engineered materials as perfect as possible, thinking that avoiding completely the formation defects was the solution to make the "perfect material" with a desired property. Indeed, this is true for some application like opto-electronics where pure and defect free materials are preferred. However, scientist also realized that the possibility of making imperfectly crystalline materials allowed them to tailor material properties into diverse combinations. Giving them another "tool" to create materials that modern engineering devices require. One of the most fascinating example that originates from the elaborate control of defect chemistry are doped semiconductors (which will be discussed in more detail in chapter 2.1.1) and cuprates, such as $YBa_2Cu_3O_{7-x}$, in which the level of oxygen deficiency determines the temperature where these materials become superconducting.[2]

Crystal defects have been scientifically defined as:

"sites that locally break the regular periodic arrangement of atoms or ions of the crystalline parent framework because of missing or dislocated atoms or ions."[3]

They also have been classified by their dimension[1]:

1. Point defects: the simplest type of imperfection is 0-dimensional and affect isolated sites in the crystal structure. An example is a solute or impurity atom, which alters the crystal pattern in a single point.

2. Line defects: 1-dimensional defects or “dislocation” such as lines along which the crystal pattern is broken. An example is an edge dislocation which creates a deformation of the crystal lattice also in surroundings of its location.
3. Surface defects: 2-dimensional imperfection such as the external surface and the grain boundaries along which distinct crystallites are joined together. An example can be the external surface which actually represents the biggest defect in any crystal.
4. Volume defects: 3-dimensional defects which change the crystal pattern over a finite volume. They include precipitates, which are small volumes of a different crystal structure, and also include large voids or inclusions of second-phase particles (see scheme 2.1 for clarity).[4]

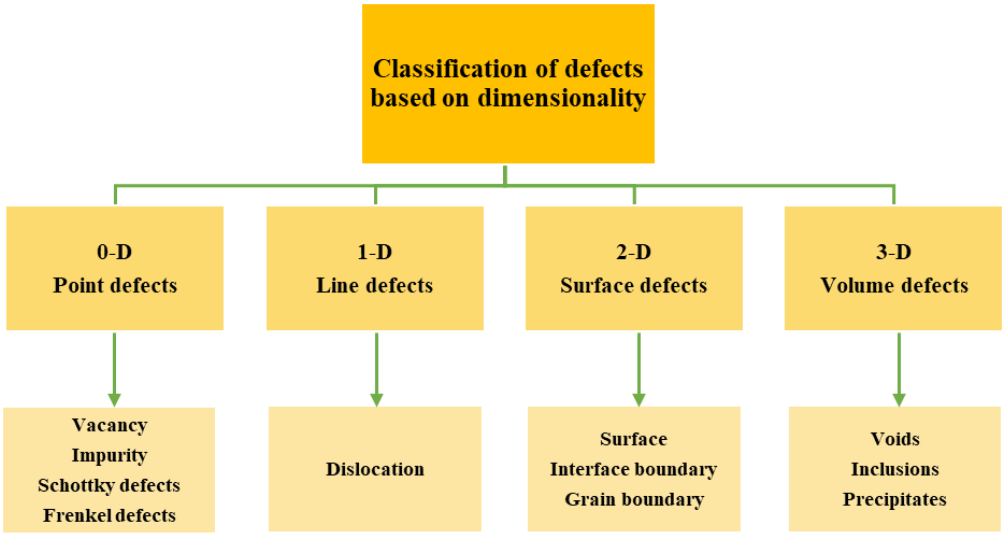

Scheme 2.1: Classification of crystal lattice defect based on the dimensionality.

The detailed discussion of the four types of defects is reported in the following paragraphs. It is worth to keep in mind that during this project, the attention has been placed only on the first class of defects, where the systematic addition of point defects in UiO-66 and MOF-808 metal-organic frameworks and their characterization will be presented.

2.1.1 Point defects

As previously seen, point defects are originated by the presence (or absence) of a single atom or molecule inside the crystal lattice. Two subclasses of point defects can be identified:

(i) Intrinsic defects can appear in a pure material, they are formed when an atom is missing from a position that is supposed to be filled in the crystal, thus creating a vacancy.

On the contrary, when an atom occupies an interstitial site where no atom would ordinarily appear, it causes the so called interstitialcy. An example is shown in figure 2.1.

A point defect disturb the crystal pattern in an isolated fashion. In particular, in most crystalline solids, interstitial sites are relatively uncommon since they have an unfavourable bonding configuration and therefore they are considered high-energy defects.[1] On the other hand, vacancies are present in significant concentration in all crystalline materials. Their most pronounced effect is to govern the migration of atoms on the crystal lattice (solid state diffusion). In fact, for an atom to move easily from one crystal lattice site to another, the target site must be vacant. Three dimensional compounds have more complex point defects, meaning for example that for an ionic compound like NaCl an isolated vacancy creates an excess charge. This excess charge can be compensated by a paired vacancy on the sublattice of other species. For instance, the excess charge associated with a Na^+ vacancy is balanced if there is a Cl^- vacancy nearby. A neutral defect that involves paired vacancies on the cation and anion sublattices is called a Schottky defect. On the contrary, the charge imbalance caused by the vacancy can be corrected by adding an interstitial of the same species; a Na^+ vacancy is compensated by a Na^+ interstitial. A neutral defect that is made up of a paired vacancy and interstitial is called a Frenkel defect.[1] In compounds where atoms are less strongly ionized it is energetically possible for species to exchange sites, so that an A-atom appears on the B sublattice or vice-versa. This type of point defect is called an anti-site defect, and is fairly common in semiconducting compounds such as GaAs.

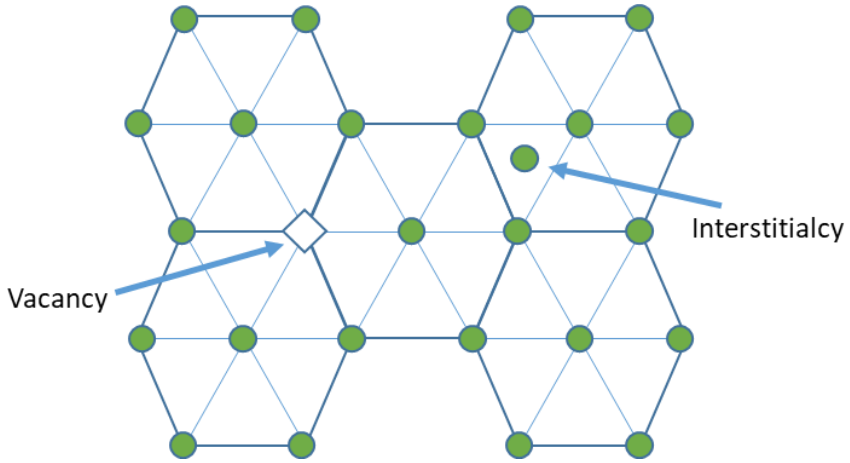

Figure 2.1: Schematic representation of two different type of point defects: a vacancy and an interstitial site in a 2D hexagonal lattice.

(ii) Extrinsic defects are caused by foreign atoms (called impurities if not added intentionally), which can occupy a lattice site or it can fill an interstitial site. In the first case

it is called a substitutional solute, in the second case it is called an interstitial solute. The interstitial sites are usually relatively small and the type of solute is largely determined by its size. Therefore, small atoms like hydrogen, carbon and nitrogen are often found in interstitial sites while larger atoms are usually substitutional. It is worth to mention that the extrinsic point defects affect most of the material properties. In fact, they are particularly important in semiconducting crystals, where they are used to control electrical properties and in structural metals and alloys, where they are added to increase mechanical strength.[1] For example, boron (B) atoms are added to increase the conductivity in Si crystals. If B is added, a valence electron is missing in the immediate B environment, causing a hole in the bonding pattern. In this way electrons can move from bond to bond by filling the hole caused by the foreign atom. This process requires a little bit of energy, but it is small if compared to the energy required to excite an electron from a Si-Si bond into a high-energy state. The same result can be achieved when doping Si crystals with phosphorus (P). P brings more electrons than are needed to fill the covalent bonds, with one electron left over. This electron requires a little bit of energy to be excited into the valence band where it can travel through the lattice.[4] Another example has its roots back in the ancient age when Roman military as well as some Asiatic population stationed in Turkey discovered a way to increase the mechanical strength of iron-made weapons. This process was called later in modern age solution hardening. The explanation for this relies on the fact that the solute atom is always a bit too large or a bit too small to fit perfectly into the crystal lattice site that it is supposed to occupy, and distorts the crystal lattice in its attempt to fit as nicely as possible. This distortion blocks the motion of the linear defects (dislocations) that are responsible for plastic deformation and, consequently, hardens the crystal.[1]

2.1.2 Line defects (dislocations)

Dislocations are lines formed through the crystal along which the crystallographic registry is lost. Their role in the microstructure is to control the yield strength and subsequent plastic deformation of crystalline solids at ordinary temperatures. Dislocations also participate in the growth of crystals and in the structures of interfaces between crystals. They can act as electrical defects in optical materials and semiconductors, in which they are often undesirable.

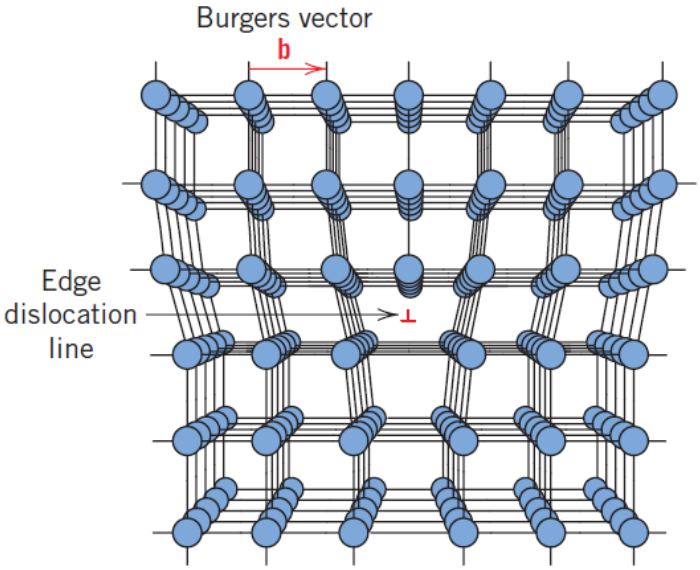

Figure 2.2: Schematic representation of a formation of an edge dislocation. Reprinted with the permission of ref.[4] Copyright 2007 John Wiley & Sons.

There are two different types of dislocations: edge and screw dislocations. The edge dislocation shown in figure 2.2 has the characteristic that the Burgers vector (b)* is perpendicular to the dislocation line which is perpendicular to the plane of the page. This perpendicularity is characteristic of an edge dislocation. In the region around the dislocation line there is some localized lattice distortion. The atoms above the dislocation line in Figure 2.2 are squeezed together, and those below are pulled apart. The magnitude of this distortion decreases with the distance away from the dislocation line.

More difficult to visualize is a screw dislocation which may be formed by a shear stress that is applied to produce the distortion as shown in figure 2.3. The right region of the crystal is shifted to the bottom portion and the dislocation line is parallel to the Burgers vector. The screw dislocation derives its name from the ramp that is traced around the dislocation line by the atomic planes of atoms. As in the case of an edge dislocation the line energy of a screw dislocation is proportional to the square of its Burgers vector.

It is worth to mention that dislocations in real materials are most commonly neither pure edge nor pure screw in their character, but are mixed dislocations whose Burgers vectors lie at an intermediate angle to the local direction of the dislocation line.

* The Burgers vector denoted as b, represents the magnitude and direction of the lattice distortion. The direction of the vector depends on the plane of dislocation, while the magnitude depends on the crystal lattice packing. In most metallic materials, the magnitude of the Burgers vector for a dislocation is equal to the interatomic spacing of the material.

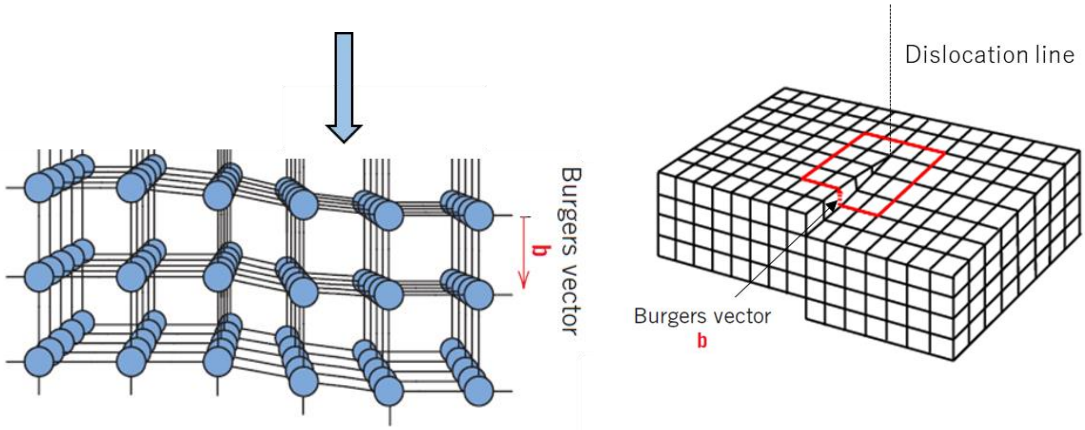

Figure 2.3: Left panel: schematic representation of a formation of a screw dislocation. The blue arrow represent the shear stress applied to the crystal in order to create the screw dislocation. Right panel: the screw dislocation in another perspective. Reprinted with the permission of ref [4]. Copyright John Wiley & Sons 2007.

2.1.3 Surface defects

The two-dimensional defects (surfaces) that appear in a crystals can be divided into three subtypes: free surfaces, which are the usual external surfaces that describe the end of the solid. Inter-crystalline boundaries, which separate grains or distinct phases within the solid and last but not less important are the internal defects that disrupt the crystalline pattern over a surface within a crystal. These 2D defects have basically two important characteristics. First, since they are surfaces inside a crystal they have peculiar atomic structures that depend on orientation. Second, they have a positive energy which is ordinarily equal to the surface tension of the interface. A detailed discussion of the two sub-types is reported below:

(i) Free surfaces can be considered interfaces between the end of a crystalline solid and vapour or liquid. Being the first part of the solid in contact with another phase allows to dictate the interaction between these two phases, influencing the behaviour of the solid. The structure of the surface is derived from the pattern of atomic packing on the crystal plane that lies parallel to the surface. The behaviour of the surface can often be influenced by that pattern; however, the structure of the surface always differs at least a bit from that of a crystal plane that aligns it within the bulk crystal. Even when the crystal sits in a perfect vacuum, the atoms in the outmost layer are bound only on one side and leave dangling bonds on the outside. The configuration of these atoms adjusts to accommodate the asymmetry of the bonding in the best possible way. This “dangling bonds” provide favourable adsorption sites

for external atoms coming from the other phase. It is therefore very common that the interface is often enriched with foreign species (surfactants) that try to saturate these bonds.

(ii) Interfaces between crystals (see figure 2.4) are regions which are located between small crystallites (grains) with a primary phase (which is possessed by the majority of the grain) and other several grains with a different phase (which can have different composition and crystal structure).

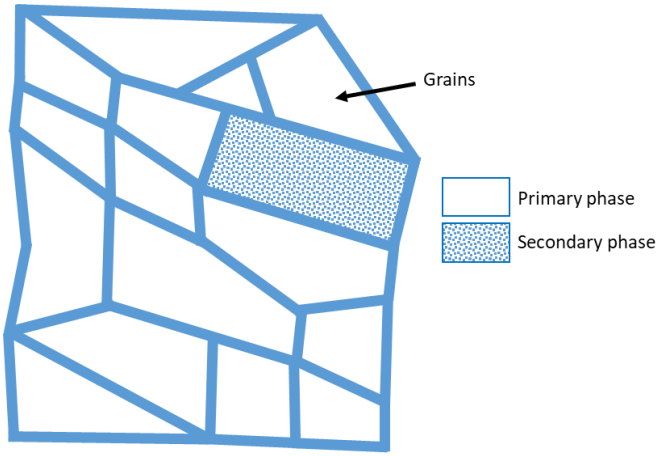

Figure 2.4: Schematic drawing of poly-granular structure showing grain boundaries with two-phase interfaces.

(iii) Internal defects are surface defects that commonly appear in the interior of a single crystal and are of two types: stacking faults and antiphase boundaries. A stacking fault is an error in the sequence of planes of atom positions in the crystal. If we consider the plane sequence ABABAB as perfect, the sequence ABABCAB has an extra C plane which is a stacking fault. On the contrary, the internal defects known as antiphase boundaries only occur in ordered compounds which can be considered as a stacking of parallel planes. This type of defects is created either by omitting one plane in the stacking pattern, or by a slip displacement at the antiphase plane (caused for example by an external mechanical force). When an antiphase boundary occurs it will result in a sequence like ABBAB, where the missing A plane cause a mismatch in the order of the stacking pattern (see figure 2.5).

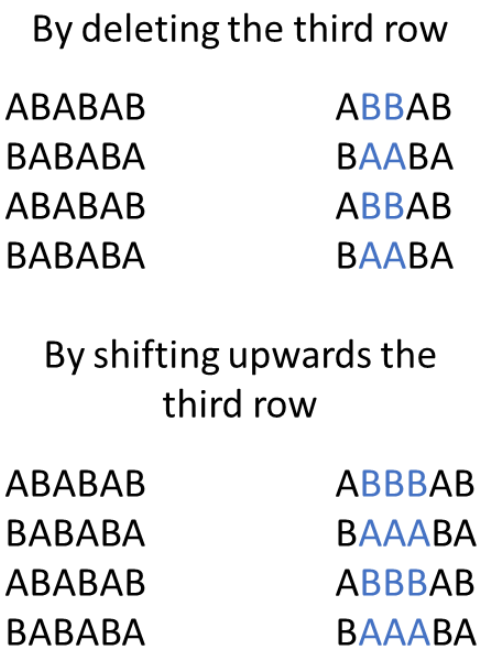

Figure 2.5: schematic representation of a formation of an antiphase boundary in 2D.

2.1.4 Volume defects

Volume defects in crystals are three-dimensional aggregates of atoms or vacancies. There are four subgroups of this type of defects:

(i) Precipitates, are small particles that are present into the matrix of the crystal. When added intentionally, they are used mainly to increase the strength of structural alloys by acting as obstacles to the motion of dislocations. Their role in the microstructure is to modify the behaviour of the matrix rather than to act as separate phases on their own.

(ii) Dispersants are bigger particles which vary in size from a fraction of a micron to the normal grain size (10-100 μm) and behave like a secondary phase which can influence the behaviour of the primary phase. In fact, when a crystal contains dispersants properties of the resulting material are some average of the properties of the dispersant phase and the parent one.

(iii) Inclusions are relatively large, undesirable particles that entered the system as dirt or are formed by precipitation.

(iv) Voids are holes (in the μm range) in the solid formed by trapped gases or by the accumulation of vacancies. Most of the times these are undesired defects that can decrease the mechanical strength and cause fractures of the material at relatively small loads.

2.2 Metal-organic frameworks

Defects of various nature and scale, as well as heterogeneity and structural disorders are key attributes of solid-state materials and strongly affect their physical and chemical properties. In some cases, it is desirable to have crystals as perfect as possible (e.g. optoelectronics), but in others, material properties rely on characteristic imperfections of the host lattice.[3] Metal-organic frameworks (MOFs) being essentially porous crystalline solid-state materials, also carry various kinds of defects which may give them unique properties, as we shall see in the next chapters.

According to the recommendation of International Union of Pure and Applied Chemistry (IUPAC) "MOFs are formally coordination polymers (CP) (or alternatively Coordination Network) with an open framework containing potential voids."
The framework is constructed by organic molecules called linkers that can bridge inorganic metal clusters to form 2D or 3D periodic networks with guest-accessible porosity. The first time that the term MOFs appeared was in 1995 when Yaghi et. al used to describe a new organic-inorganic hybrid material with 4,4'-bipyridine (bpy) linked with Cu-centers ($(Cu(4,4'\text{-}bpy)_{1.5}\cdot NO_3(H_2O)_{1.5})$).[5] Nowadays, a systematic nomenclature of MOFs is still not well defined, however, there is an essential characteristic that defines them such as permanent porosity upon guest removal without the collapse of the structure. Another feature that made MOFs famous in the scientific community is the large tunability of these materials. This characteristic in combination with the powerful concept of reticular chemistry introduced by Yaghi et. al.[6-7] allow MOFs to be designed to meet certain chemical requirements, ranging from increased porosity with the use of bigger linker molecules (see figure 2.6), biocompatibility using non-toxic metal centres to water harvesting.[8] These features since the beginning allowed them to be used for a wide spectrum of different application ranging from gas storage,[9-10] separation,[11] catalysis,[12-14] air purification[15] and even biological application as drug delivery agents.[16]

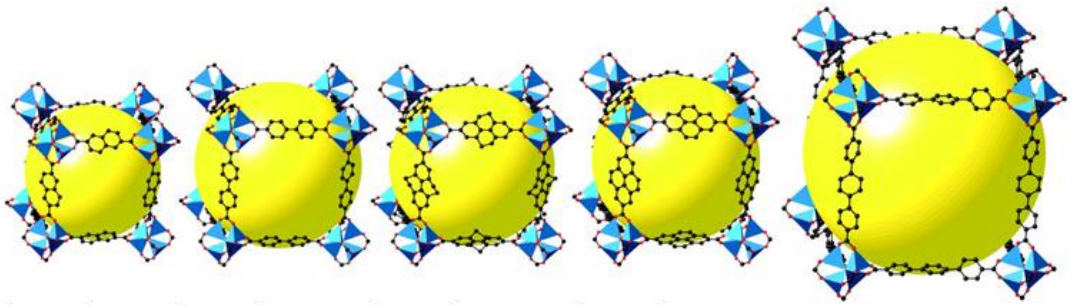

Figure 2.6: The powerful concept of reticular chemistry in MOFs introduced by Yaghi and co-workers, where a series of isoreticular MOFs (in this example some of the IRMOF series) with the same inorganic building block are "expanded" with an altered metrics of the organic linkers. Reprinted with the permission of ref.[7] Copyright 2002, The American Association for the Advancement of Science.

A useful classification of CP was introduced in 1997 by Kitagawa et al. He divided coordination polymers in three generations.

The 1st CP generation includes materials that collapse irreversibly upon guest removal resulting in amorphous structure without porosity. On the contrary, in the 2nd CP generation compounds that own a rigid network and can keep their structure intact after the removal of guest molecules are included (examples that are in this category are MOF-5 and the UiO series). This ability makes them appropriate candidates for industrial application and be used for gas storage or catalysis. Lastly, in the 3rd CP generation are included materials that exhibit permanent porosity which also possess a structural flexibility during the removal of guest molecules or other external stimuli like temperature or pressure change.[17-18] These structures possess the so-called "breathing behaviour" which occurs when the framework structure shrinks and expands during desorption and adsorption processes.[19] This unique property can be useful for gas separation process as it was shown with MOF-5 by Henke et. al where the introduction of flexible alkyl ether side chains at the BDC linker gives the MOF the ability to be selective towards CO_2 while other gasses like N_2 and CH_4 cannot infiltrate the system.[20] Despite all these very promising properties most of the reported MOFs suffer from low thermal and chemical stability. A striking example is MOF-5, which has a thermal stability that can reach 300°C but it is not water stable and thus cannot survive long after exposure to humid air.[21] This is a huge drawback that limit considerably a possible industrial application of MOFs. Steps forwards in this aspect were made with Zr-based MOFs which are chemically and thermally stable. One of the first reported Zr-based MOF was UiO-66 discovered in 2008 by Lillerud and co-workers.[22] It cons ists of $[Zr_6O_4(OH)_4]^{12+}$ metal-nodes

in 12-fold coordination of terephthalic acid (BDC^{2-}) and crystallizes in a face-centered cubic framework in fcu topology (see figure 2.7).

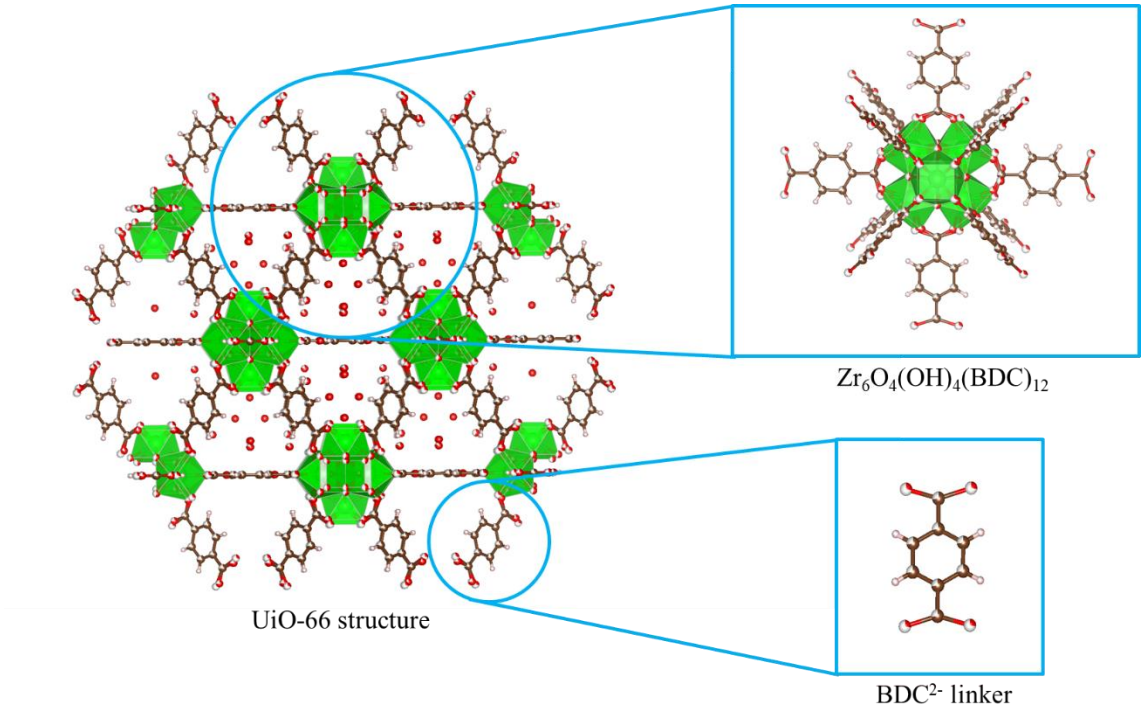

Figure 2.7: Structure of UiO-66 with Zr_6 clusters (green polyhedral), where in the bottom inset the BDC^{2-} linker is highlighted; while in the upper inset the secondary building unit (SBU) of UiO-66 is shown.

Isoreticular expansions of this material were also reported namely UiO-67, UiO-68 with biphenyl-4,4′-dicarboxylic acid (BPDC) and terphenyl-4,4″-dicarboxylic (TPDC) acid as linker, respectively.[22]All feature the same octahedral Zr_6-oxo-cluster, with a secondary building unit that can be formulated as $Zr_6O_4(OH)_4(-CO_2)_{12}$ where each Zr atom is connected with 8 oxygen atoms. This structure shows two different cavities (tetrahedral and octahedral) with different pore apertures and diameters according to the size of the incorporated linkers (BDC, BPDC or TPDC). Interestingly, when these materials are thermally activated (300°C) the four μ_3-OH groups leave the MOF (see figure 2.8) as water molecules (two OH groups are realised while the other two lose one hydrogen resulting in two water molecules) resulting in a $Zr_6O_6(BDC)_{12}$ distorted, dehydroxylated material with coordinatively unsaturated sites (CUS).[23] These CUS are Lewis acid sites that can be used for catalysis as we shall see in the next chapters of this thesis.

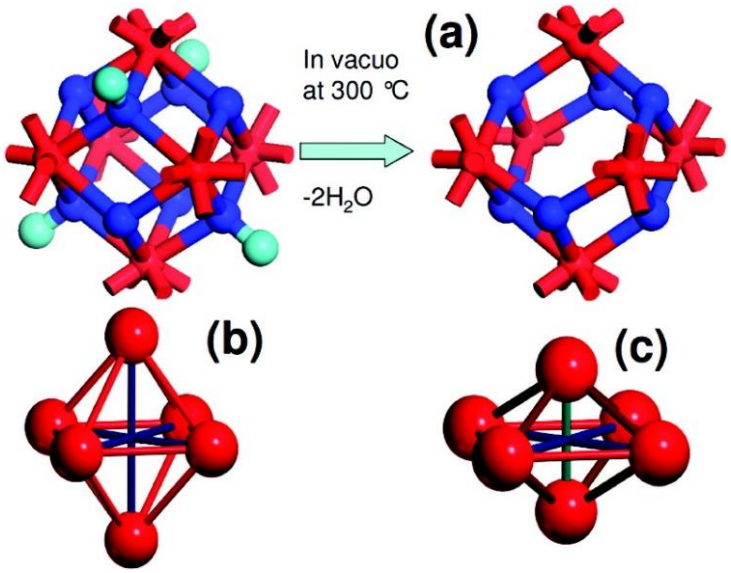

Figure 2.8: (a) dehydroxylation process of the $Zr_6O_4(OH)_4$ cluster upon thermal treatment in vaccum which lead to a distorted Zr_6O_6 cluster. (b) Regular Zr_6 cluster before activation shown as a perfect octahedron. (c) Zr_6 cluster after activation shown as a squeezed octahedron. In red, blue and cyan are depicted Zr, O and H atoms respectively. Reprinted with the permission from ref [23]. Copyright 2011, American Chemical Society.

The high thermal stability of these Zr-based MOFs and in particular of UiO-66 that can reach more than 500°C relies on the strong bond between Zr and O.[24-25] It was shown with TGA-MS that the weakest bond in the structure is between the benzene ring and the carboxylic group.[26] Still today it is one of most stable MOFs present in the literature, however the major limitation of this system is the small pore apertures (< 6Å) which considerably limits the choice of possible reactions that can be catalyzed with this MOF. Researcher have tried to develop other Zr-based MOFs with bigger pores and thus higher surface area and so far more than 50 different structures have been reported (see table 2.1).[27] Stunning examples with high thermal stability and high surface area that can reach more than 4000 m^2g^{-1} have been reported.[27-31] Among them, NU-1000 composed with 1,3,6,8-tetrakis(p-benzoate)pyrene (TBAPy4) ligand and an octahedral Zr_6 cluster has been shown to be active towards diverse catalytic reactions including degradation of a nerve agent simulants.[32] Nevertheless, UiO-66 is still under the spotlight in the MOF community for several reasons. The first one is due to its chemical stability against various solvents (from polar ones like water to non-polar ones like hexane) and also towards acids like HCl. The second one is its tolerance against the intentional introduction of defects e.g missing linker or missing cluster defects. This peculiar characteristic started few years ago a new branch of study in MOFs chemistry called

"defect engineering" with the aim to enhance MOFs reactive properties such as catalysis and gas adsorption. [27]

Table 2.1: List of Zr-based MOFs discovered so far. The table is reprinted with the permission of ref. [27] Copyright 2016 Royal Society of Chemistry. Ligands abbreviation are reported below the table for simplicity.

Zr MOF	Ligand	Zr cluster/core	Topology
UiO-66	BDC^{2-}	$Zr_6O_4(OH)_4$	fcu, 12-connected
UiO-67	$BPDC^{2-}$	$Zr_6O_4(OH)_4$	fcu, 12-connected
UiO-68	$TPDC^{2-}$	$Zr_6O_4(OH)_4$	fcu, 12-connected
NU-1000	$TBAPy^{4-}$	$Zr_6O_4(OH)_4(H_2O)_4(OH)_4$	csq, 8-connected
NU-1100	$PTBA^{4-}$	$Zr_6O_4(OH)_4$	ftw, 12-connected
NU-1101	$Py\text{-}XP^{4-}$	$Zr_6O_4(OH)_4$	ftw, 12-connected
NU-1102	$Por\text{-}PP^{4-}$	$Zr_6O_4(OH)_4$	ftw, 12-connected
NU-1103	$Py\text{-}PTP^{4-}$	$Zr_6O_4(OH)_4$	ftw, 12-connected
NU-1104	$Por\text{-}PTP^{4-}$	$Zr_6O_4(OH)_4$	ftw, 12-connected
MOF-801	FUM^{2-}	$Zr_6O_4(OH)_4$	fcu, 12-connected
MOF-802	$PZDC^{2-}$	$Zr_6O_4(OH)_4$	bct, 10-connected
MOF-804	$BDC\text{-}2OH^{2-}$	$Zr_6O_4(OH)_4$	fcu, 12-connected
MOF-805	$NDC\text{-}2OH^{2-}$	$Zr_6O_4(OH)_4$	fcu, 12-connected
MOF-806	$BPDC\text{-}2OH^{2-}$	$Zr_6O_4(OH)_4$	fcu, 12-connected
MOF-808	BTC^{3-}	$Zr_6O_4(OH)_4$	spn, 6-connected
MOF-812	MTB^{4-}	$Zr_6O_4(OH)_4$	ith, 12-connected
MOF-841	MTB^{4-}	$Zr_6O_4(OH)_4$	flu, 8-connected
MOF-525	$TCPP^{4-}$	$Zr_6O_4(OH)_4$	ftw, 12-connected
MOF-535	XF^{4-}	$Zr_6O_4(OH)_4$	ftw, 12-connected
MOF-545	$TCPP^{4-}$	$Zr_6(O)_8$	csq, 8-connected
MOF-867	$BPYDC^{2-}$	$Zr_6O_4(OH)_4$	fcu, 12-connected
PCN-56	$TPDC\text{-}2CH_3^{2-}$	$Zr_6O_4(OH)_4$	fcu, 12-connected
PCN-57	$TPDC\text{-}4CH_3^{2-}$	$Zr_6O_4(OH)_4$	fcu, 12-connected
PCN-58	$TPDC\text{-}2CH2N_3^{2-}$	$Zr_6O_4(OH)_4$	fcu, 12-connected
PCN-59	$TPDC\text{-}4CH2N_3^{3-}$	$Zr_6O_4(OH)_4$	fcu, 12-connected
PCN-94	$ETTC^{4-}$	$Zr_6O_4(OH)_4$	ftw, 12-connected
PCN-221	$TCPP^{4-}$	Zr_8O_6	ftw, 12-connected
PCN-222	$TCPP^{4-}$	$Zr_6(OH)_8$	csq, 8-connected
PCN-223	$TCPP^{4-}$	$Zr_6O_4(OH)_4$	shp, 12-connected
PCN-224	$TCPP^{4-}$	$Zr_6O_4(OH)_4$	she, 6-connected
PCN-225	$TCPP^{4-}$	$Zr_6O_4(OH)_4$	sqc, 8-connected
PCN-228	$TCP\text{-}1^{4-}$	$Zr_6O_4(OH)_4$	ftw, 12-connected
PCN-229	$TCP\text{-}2^{4-}$	$Zr_6O_4(OH)_4$	ftw, 12-connected
PCN-230	$TCP\text{-}3^{4-}$	$Zr_6O_4(OH)_4$	ftw, 12-connected
PCN-521	$MTBC^{4-}$	$Zr_6(OH)_8$	flu, 8-connected
PCN-700	Me_2BPDC^{2-}	$Zr_6O_4(OH)_4$	bcu, 8-connected
PCN-777	$TATB^{3-}$	$Zr_6O_4(OH)_4$	spn, 6-connected
DUT-51	$DTTDC^{2-}$	$Zr_6O_4(OH)_4$	reo, 8-connected
DUT-52	$2,6\text{-}NDC^{2-}$	$Zr_6O_4(OH)_4$	fcu, 12-connected
DUT-84	$2,6\text{-}NDC^{2-}$	$Zr_6(O)_8$	(4,4)IIb, 6-connected
DUT-67	TDC^{2-}	$Zr_6O_4(OH)_4$	reo, 8-connected
DUT-68	TDC^{2-}	$Zr_6O_4(OH)_4$	8-connected

DUT-69	TDC^{2-}	$Zr_6O_4(OH)_4$	bct, 10-connected
BUT-10	$FDCA^{2-}$	$Zr_6O_4(OH)_4$	fcu, 12-connected
BUT-11	$DTDAO^{2-}$	$Zr_6O_4(OH)_4$	fcu, 12-connected
BUT-30	$EDDB^{2-}$	$Zr_6O_4(OH)_4$	fcu, 12-connected
MIL-140A	BDC^{2-}	$Zr(\mu_3\text{-}O)_3O_4$	/
MIL-140B	$2,6\text{-}NDC^{2-}$	$Zr(\mu_3\text{-}O)_3O_4$	/
MIL-140C	$BPDC^{2-}$	$Zr(\mu_3\text{-}O)_3O_4$	/
MIL-140D	Cl_2ABDC^{2-}	$Zr(\mu_3\text{-}O)_3O_4$	/
MIL-153	$pgal^{3-}$	ZrO_8	/
MIL-154	$Hgal^{3-}$	ZrO_8	/
MIL-163	$TzGal^{6-}$	ZrO_8	/
CPM-99	$TCBPP^{4-}$	$Zr_6O_4(OH)_4$	ftw, 12-connected
UMCM-309a	BTB^{3-}	$Zr_6O_4(OH)_4$	kgd, 6-connected
Zr-TTMC	$TTMC^{2-}$	$Zr_6O_4(OH)_4$	fcu, 12-connected
Zr-BTB	BTB^{3-}	$Zr_6O_4(OH)_4$	kgd, 6-connected
Zr-ABDC	$ABDC^{2-}$	$Zr_6O_4(OH)_4$	fcu, 12-connected
PIZOF	$PEDC^{2-}$	$Zr_6O_4(OH)_4$	fcu, 12-connected
BPV-MOF	BPV^{2-}	$Zr_6O_4(OH)_4$	fcu, 12-connected
mBPV-MOF	$BPHV^{2-}$	$Zr_6O_4(OH)_4$	fcu, 12-connected
mPT-MOF	PT^{2-}	$Zr_6O_4(OH)_4$	fcu, 12-connected
ZrBTBP	$H3BTBP^{3-}$	ZrO_6	/
UPG-1	$H4TTBMP^{2-}$	ZrO_6	/
UiO-66(AN)	AN^{2-}	$Zr_6O_4(OH)_4$	fcu, 12-connected
UiO-66-1,4-Naph	$1,4\text{-}NDC^{2-}$	$Zr_6O_4(OH)_4$	fcu, 12-connected
Zr-ADC	ADC^{2-}	$Zr_6O_4(OH)_4$	fcu, 12-connected
Zr-DTDC	$DTDC^{2-}$	$Zr_6O_4(OH)_4$	fcu, 12-connected
Zr-TCPS	$TCPS^{4-}$	$Zr_6O_4(OH)_4$	flu, 8-connected
Zr-BTDC	$BTDC^{2-}$	$Zr_6O_4(OH)_4$	fcu, 12-connected
Zr-BTBA	$BTBA^{4-}$	$Zr_6O_4(OH)_4$	ftw, 12-connected
Zr-PTBA	$PTBA^{4-}$	$Zr_6O_4(OH)_4$	ftw, 12-connected
MMPF-6	$TCPP^{4-}$	Zr_6O_8	csq, 8-connected
Zr-AP-1	$AP\text{-}CH3^{2-}$	$Zr_6(OH)_8$	bcu, 8-connected
Zr-AP-2	AP^{2-}	$Zr_6(OH)_8$	dia, 4-connected
Zr-AP-3	AP^{2-}	$Zr_6(OH)_8$	bcu, 8-connected

BDC^{2-}= terephthalate; $BPDC^{2-}$= biphenyl-4,4´ -dicarboxylate; $TPDC^{2-}$= terphenyl-4,4´´-dicarboxylate; $TBAPy^{4-}$= 1,3,6,8-tetrakis(p-benzoate)pyrene; $Py\text{-}XP^{4-}$= 4´ ,4´´,4´´´´´,4´´´´´´-(pyrene-1,3,6,8-tetrayl) tetrakis(2´ , 5´ - dimethyl-[1,1´ -biphenyl]-4-carboxylate); $Por\text{-}PP^{4-}$= meso-tetrakis-(4-carboxylatebiphenyl)-porphyrin; $PTBA^{4-}$= 4-[2-[3,6,8-tris[2-(4- carboxylatephenyl)-ethynyl]-pyren-1-yl]ethynyl]-benzoate; $Py\text{-}PTP^{4-}$= 4,4´ ,4´´,4´´´´-((pyrene-1,3,6,8-tetrayltetrakis(benzene-4,1-diyl))tetrakis(ethyne2,1-diyl))tetrabenzoate; $Por\text{-}PTP^{4-}$= meso-tetrakis-(4-((phenyl)ethynyl)benzoate)porphyrin; FUM2 = fumarate; $PZDC^{2-}$= 1H-pyrazole-3,5- dicarboxylate; BTC^{3-}= benzene-1,3,5-tricarboxylate; MTB^{4-}= 4,4´,4´,4´´´´-methanetetrayltetrabenzoate; $TCPP^{4-}$= meso-tetrakis(4-carboxylatephenyl)porphyrin; XF^{4-}= 4,4´ -((1E,1´E)-(2,5-bis((4-carboxylatephenyl)ethynyl)-1,4-phenylene)bis(ethene-2,1-diyl))dibenzoate; $BPYDC^{2}$-= 2,2´-bipyridine 5,5´ -dicarboxylate; $ABDC^{2-}$= 4,4-azobenzenedicarboxylate; $TCBPP^{4-}$= tetrakis(4-carboxylatebiphenyl)porphyrin; $ETTC^{4-}$= 4´ ,4´´,4´´´,4´´´´´-(ethene-1,1,2,2-tetrayl)tetrabiphenyl-4-carboxylate;TDC^{2-}=2,5-thiophenedicarboxylate;
$MTBC^{4}$=4´,4´´,4´´´,4´´´´methanetetrayltetrabiphenyl-4-carboxylate; $TATB^{3-}$= 4,4´ ,4´´-s-triazine-2,4,6-triyl-tribenzoate; $DTTDC^{2-}$= dithieno[3,2-b;2´ ,3´ -d]-thiophene-2,6-dicarboxylate; $2,6\text{-}NDC^{2-}$= naphthalene-2,6-dicarboxylate; $FDCA^{2-}$ = 9-fluorenone-2,7-dicarboxylate; $DTDAO^{2-}$= dibenzo[b,d]thiophene-3,7-dicarboxylate 5,5-dioxide; $EDDB^{2-}$= 4,4´-(ethyne-1,2-diyl)dibenzoate; $H3pgal^{3-}$= pyrogallol; H4gal = gallic acid; H2sal = salicylic acid; H6TzGal = 5,5´ -(1,2,4,5-tetrazine-3,6-diyl)bis(benzene-1,2,3-triol); BTB^{3-}= 5´ -(4- carboxyphenyl)[1,10 :300,100-terphenyl]-4,400-dicarboxylate; $TTMC^{2-}$= (2E,4E)-hexa-2,4-dienedioate; ABDC2-= azobenzenedicarboxylate; H6BTBP = 1,3,5-tris(4-phosphonophenyl)benzene; H_6TTBMP = 2,4,6-tris(4-(phosphonomethyl)phenyl)-1,3,5-triazine; $PEDC^{2-}$= 4,4´-(1,4-phenylenebis-(ethyne-2,1-diyl))dibenzoate; BPV^{2-}= 5,5´-bis(carboxylateethenyl)-2,20 -bipyridine; $BPHV^{2-}$=4,4´-bis(carboxylateethenyl)-1,1´-biphenyl; $TPHN^{2-}$= 4,4´-bis(carboxylatephenyl)-2-nitro-1,1´-biphenyl; ADC^{2-} = 9,10-anthacenyl-bis(benzoate); $DTDC^{2-}$ = 3,4-dimethylthieno[2,3-b]thiophene-2,5-dicarboxylate; $TCPS^{4-}$= tetrakis(4-carboxyphenyl)silane; $BTBA^{4-}$= 4,4´,4´´,4´´´-(biphenyl-3,3´,5,5´ -tetrayltetrakis(ethyne-2,1-diyl))tetrabenzoate; AP^{2-} = 1,6-adipate.

2.3 Defects in metal-organic frameworks*

After defining a defect in a general way in chapter 2.1, it is now important to mention that within the field of MOFs, the most important defects are point defects and are included in this category: (i) missing linker defects, (ii) missing node defects, (iii) modified node defects, and (iv) modified linker defects.

Missing linker defects are generated by the lack of single linker molecules within the structure. When more of these defects are present in a critical concentration and spatial distribution they result in the generation of missing node defects. In other words, a missing node defect is the result of an unequal distribution and special concentration of linker defects within the framework. The equilibrium between these two kinds of defects is extremely difficult to tell and in most cases only indirectly accessible. For this reason, scientists must rely on indirect methods to characterize, e.g., the analysis of the Brunauer-Emmet-Teller (BET) surface area in combination with results from thermogravimetric analysis (TGA) and a range of spectroscopic evidences. It is worth to mention that in MOF field, any modification applied to the linker or to the node that differs from the pristine framework is considered a defect.

In general, the intentional incorporation of defects and the subsequent application of defective MOFs as heterogeneous catalysts is one of the largest areas in MOF research today. The creation of linker defects that introduce Lewis acidic sites together with missing node defects that enhance diffusion of products and educts offers interesting opportunities. Many catalytic reactions with defective MOFs that have been successfully tested, some are the dimerization of ethylene, cyanosilylation of benzaldehyde, isomerization and Meerwein-Ponndorf-Verley (MPV) reactions, just to name a few.[33-35] Nevertheless, it is important to have in mind, that established catalysts still outperform defective MOFs as they would outperform “perfect” MOFs and are reasonably cheap at the same time.[36]

*This chapter is inspired and partially reproduced with permission from the review article: Dissegna, S.; Epp, K.; Heinz, W. R.; Kieslich, G.; Fischer, R. A., *Adv. Mater.* **2018,** 30, 1704501.

Thus, potential applications of (defective) MOFs still seem to be limited to the field of fine chemical catalysis. In this context, it is no surprise that research focus has also been drawn on the chemical manipulation of the inner framework, e.g., by the introduction of different linker functionalities[37] or modification of the metal node.[38] These manipulations allow for accessing the factors such as the hydrophilicity of the framework and access to reactive sites and expanded coordination space in proximity of reactive centers. At the same time, computational scientists also entered the field. However, standard simulation techniques use periodic boundary conditions, which make the explicit treatment of defect sites and their distribution challenging. In principle, choosing a large enough starting unit could account for disorder, but practically the size of this unit is constrained by computational demands. However, there are scale-bridging approaches to circumvent such difficulties and in turn calculate properties such as gas sorption and mechanical properties in dependency of defect incorporation.[39] At this point it is already evident that defect chemistry of MOFs offers a great deal of opportunities for the targeted manipulation of various properties. Although extremely challenging, the rising interest of scientists and the related increase of publications on this topic are self-evident (see Figure 2.9).

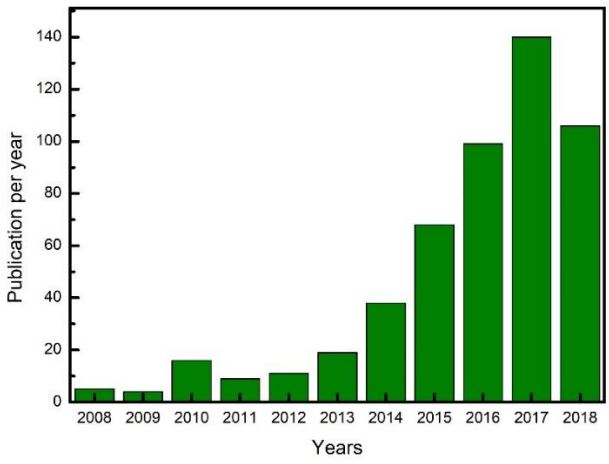

Figure 2.9: Total number of publications on the topic over the past decade. The plot was created based on entries in the Web of Science (20 August 2018) by using the keyword “defect metal-organic frameworks”.

2.3.1 Synthesis of defective MOFs

The targeted incorporation of defects into MOFs, i.e. the synthetic control of defect concentration and chemical nature, is still challenging. Two synthetic routes are generally used for the preparation of MOFs with various types of defects: (i) the "de novo" synthesis and (ii) the use of post-synthetic treatment methods. A schematic representation of all applied methods to create defects in MOFs is given in Scheme 2.2.

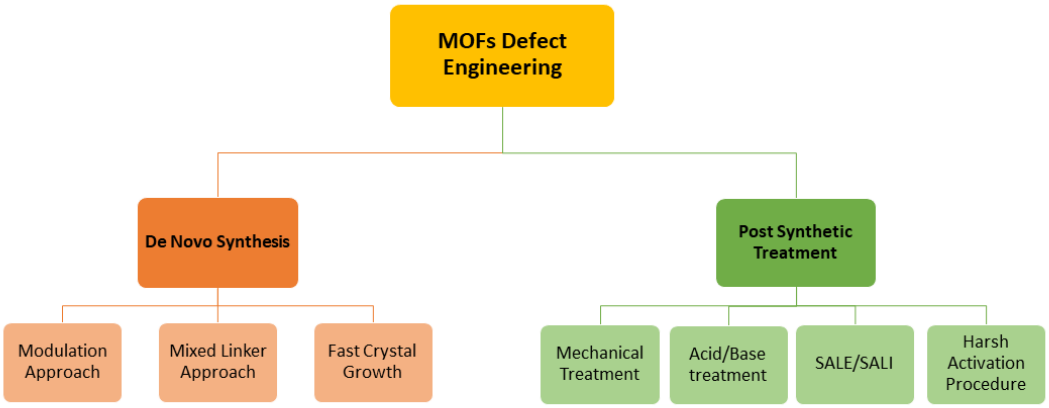

Scheme 2.2: Representation of all main procedures to create defects in MOFs. Reprinted with the permission of ref. [40] Copyright 2018, John Wiley & Sons.

(i) To date, the most common "de novo" approach in the community for the synthesis of defective MOFs is the addition of large amounts of monocarboxylic acids in addition to the linker molecules during the MOF synthesis. This approach, known as "modulation approach", originates from the synthetic attempts of reducing crystallization speed of MOFs to obtain higher degrees of crystallinity. It is established today, that small amounts of monocarboxylic acids, the so-called modulator, slow down the speed of crystallization and provide a material with less defects, while large modulator concentrations result in increased incorporation of these molecules in the framework yielding in higher concentration of defects. The first report using this approach is given by Ravon et al. in 2010, who used 2-methyl-toluic acid as modulator in the synthesis of MOF-5.[41] Since then, many research groups focused on the synthesis of defective MOFs, with typical modulators being formic acid (FA), acetic acid (AA), trifluoro acetic acid (TFA), difluoro acetic acid (DFA), and their derivatives (see Figure 2.10, left panel).

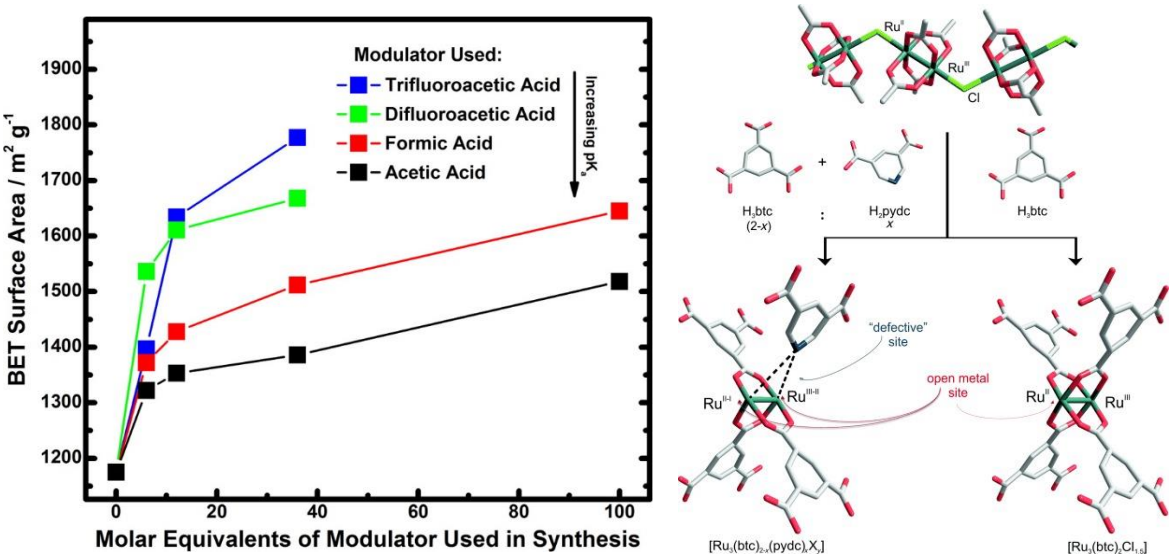

Figure 2.10: Left panel: Plot of the amount of linker deficiencies per Zr6 formula unit against the molar equivalents of modulator in UiO-66. Reproduced with permission of ref. [42] Copyright 2016, American Chemical Society. Right panel: Mixed linker approach in Ru-HKUST-1 leads to modified node defects. Reproduced with permission. of ref. [43] Copyright 2014, John Wiley & Sons.

In 2013, Vermoortele et al. applied the modulator approach to produce highly defective UiO-66, by using TFA as modulator.[44] In their work, the authors subsequently removed TFA by thermal treatment at 320 °C, creating unsaturated sites as highly reactive Lewis acid sites that implicate the application of such systems in catalysis. It was only in 2016 when Shearer et al. systematically studied the impact of different modulators such as FA, AA, TFA, and DFA on the defect chemistry of UiO-66.[42] The authors observed a correlation between the defect concentration and the Brønsted acidity of the modulator. Therewith, based on its pK_a (which is solvent dependent) TFA appears to be the most suitable modulator of the above series for the synthesis of defective UiO-66. It is worth noting that so far research has focused on applying the modulator approach to MOFs with carboxylic acids as linkers, with UiO-66 currently being the model system for many studies. In the so-called mixed linker approach, the linker of the parent framework is partially substituted by a linker with having a different coordinating group, e.g., 1,3,5-tricarboxylate (BTC^{3-}) by pyridine-3,5-dicarboxylate ($pydc^{2-}$).[45] An example for this approach is depicted in Figure 2.10 (right panel), which shows the work of Kozachuk et al. based on Ru-HKUST-1. They find a formal reduction of the Ru centers, induced by the reaction conditions.[43] Following the impact of the modulator on the reaction kinetics and crystallinity of MOFs, it is intuitive that a fast crystallization process similarly leads to the formation of point defects, e.g., missing linker or missing cluster defects. Reaction processes to facilitate a fast crystallization include

microwave assisted synthesis as well as high concentration of the precursors. Point defects created by this approach can then be replaced by other species (counter anions) present in the MOF mother solution to further increase the functionality, e.g., OH groups in MOF-5 and IRMOF-3 (isoreticular metal-organic framework).[46]

(ii) The second synthetic approach toward defective MOFs involves the introduction of defect sites after the synthesis of the parent MOF, hence it is termed post-synthetic treatment. There exist several variations of which all involve a heterogeneous treatment of the parent MOF with modified linkers or acids. For instance, Vermoortele et al. used strong acids such as $HClO_4$ and TFA for the post-synthetic modification of MIL-100 (Fe) (Material of the Institute Lavoisier).[47] The authors observe the formation of additional Brønsted acid sites in close vicinity to the Lewis acidic sites, as proven by CO chemisorption experiments. Furthermore, no loss in crystallinity was observed after this treatment; however, the authors found a decrease in porosity which was ascribed to the presence of larger counter anions such as ClO_4^- and/or disconnected ligands within the pores. The arguably most established post-synthetic treatment method is the so-called "solvent-assisted linker exchange" (SALE). Briefly, SALE (see Figure 2.11) involves the replacement of linkers in an MOF with modified linkers of choice, e.g., functionalized[48] or longer linker,[48] or linker with an incorporated catalyst precursor,[49] via a heterogeneous reaction in a selected solvent. Importantly, SALE facilitates the synthesis of MOFs, that are difficult to obtain with a mixed linker approach, e.g., NU-125-HBTC (NU = Northwestern University).[49-51] In general, it can be summarized that SALE is particularly useful in the modification of very stable MOFs with high coordination numbers such as UiO-66 and also zeolitic imidazolate framework (ZIFs). Stunningly, Karagiaridi et al.[49] reported the successful replacement of 85% of the linkers (methylimidazole) in ZIF-8 with imidazole, resulting in a material with increased pore openings that allow bulkier molecules to react with the CUS sites present in the system.

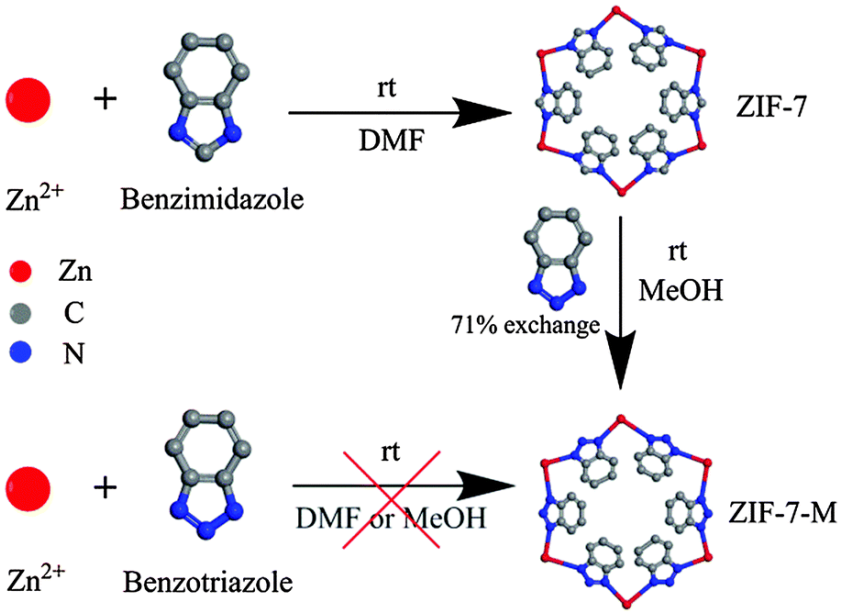

Figure 2.11: Schematic representation of the solvent assistant linker exchange (SALE) method. Where the linker benzimidazole is exchanged by benzotriazole up to 71%. This method proves itself useful when direct attempts to synthesize ZIF-7-M were unsuccessful. Reprinted with the permission of ref.[51] Copyright 2015, The Royal Society of Chemistry.

Similar to the de novo approach reported by Kozachuck et al., SALE also enables the introduction of linkers with different coordination sites, thereby modifying the electronic state of the metal node. Additionally, there are reports where MOF ligands are exchanged by solvent molecules itself (DMF) due to the ability of the solvent to coordinate to CUS as shown by Lee et al.[52] Likewise, the solvent-assisted ligand incorporation (SALI) allows for manipulating the functionality of the metal node with leaving the linker of the framework untouched.[53] For instance, Deria et al. used different perfluorinated carboxylic acids coordinating to vacant sites at the node to increase the hydrophobicity of NU-1000 and its CO_2 capture ability. As described by Deria et al., this new postsynthetic technique relies on acid–base chemistry between the hydroxyl groups on the NU-1000 node and the carboxylate group of the perfluorinated chain. Moreover, extensive washing and harsh activation procedures (especially high temperatures) can produce significant amounts of defects, likely coming from hydrolysis reactions as suggested by Shearer et al.[25] In MOF-5, thermal treatment can induce the in situ decarboxylation of terephthalic acid, generating linker fragments post-synthetically.[54] The main advantage is the simple synthetic procedure; however, a systematic control of defect creation is very difficult due to its intrinsic low reproducibility. Last but not less important, Bennett et al. used ball milling to gradually destroy UiO-66, MIL-140, and MIL-140b frameworks by the breaking of a fraction of

metal–ligand bonds. Interestingly, the inorganic $Zr_6O_4(OH)_4$ clusters of UiO-66 remain intact while the MILs ZrO chains undergo a substantial distortion.[55]

2.3.2 Characterization of defective MOFs

The in-depth characterization of defects, i.e. the elucidation of defect concentration and spatial distribution, challenges common characterization techniques. For instance, diffraction pattern of defective MOFs differs from their respective pristine counterpart only with minor changes which are hardly detected by a laboratory x-ray diffraction due to the instrument resolution limitations. Therefore, experimental techniques like x-ray absorption fine structure (EXAFS) and pair distribution function (PDF) that can probe the local structure should be used. This techniques require the use of synchrotron sources which usually are not readily accessible; therefore, the structural insight into defects in MOFs is limited. Aid to experimentalists might come from computational modelling of defective MOFs which appeared since 2015. So far the systems of choice are mainly UiO-66[39, 56] and its derivatives and some other examples with ZIF-8[57] and HKUST-1.[58] Nevertheless, useful insight on how defects may affect MOFs mechanical properties have been achieved. In particular, Van Speybroeck and co-workers provided a thermodynamic characterization of the high-pressure behaviour of UiO-66 as a function of missing linker defects and linker expansion in the absence of guest molecules. Indeed, for the defect-containing and/or expanded linker samples, a reduced mechanical stability is observed.[39]

It is apparent that the in-depth characterization on defective MOFs bear many problems which equally challenges experimental and computational chemists. Till today, scientists have found many properties that are closely linked to the defect concentration and chemistry. However, the defect structure (including local and correlated) in MOFs is barely investigated. Recently some unconventional characterization technique have been used in order to try to solve this problem. Positron annihilation lifetime spectroscopy (PALS),[59-60] and acid-base titration[61] are few techniques that recently have found their way to the field of MOFs which are worth to be briefly discussed.

PALS is a fascinating technique which uses the release of gamma rays that are produced by the interaction of Positrons (Ps) (the antiparticles of electron) with electrons. In a MOF, the main electron density is located at the framework, coupling the Ps lifetime to the pore size. Already in 2010 PALS was used by Liu et al. for this purpose.[62] However, only in 2016 Mondal et al.,[60] applied PALS to study mesopores formation in hydrogen-bonded imidazolate framework (HIF-3). The authors assigned missing building blocks in HIF-3 as reason for mesopores that are responsible for structural flexibility during gas uptake. In a more recent work the authors were able to detect the small differences in the

inner pore-sizes of Imidazolate Framework Potsdam (IFP) structures and variations of gas sorptions properties, between microwave-assisted (MW) materials and conventional electrical (CE) heating conditions.[59]

In particular, the MW-synthesized materials due to the fast crystallization process can trap free linker molecules and therefore, reduce the pore sizes from micro-pores to ultramicro-pores. According to the authors these ultramicro-pores were responsible for the enhancement in the gas uptake capacities since the gas molecules could interact more efficiently with the pore walls.[59] This examples give a clear idea that PALS has some inherent advantages towards the common N_2 physisorption measurements. Most importantly, interconnected pore space is not required to determine pore size from PALS. Therefore, this method can be applied for open and closed-pore systems.

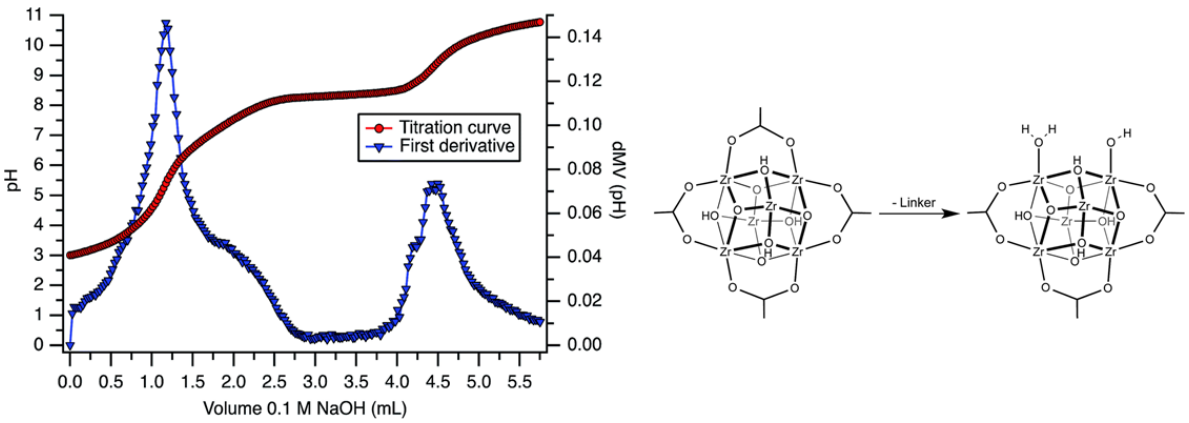

Figure 2.12: left panel titration curve (red) and its first derivative (blue) from a Zr-UiO-66 sample. Right panel: Missing linker defects as reason for M–OH_2 and M–OH groups. Reproduced with permission of ref. [61] Copyright 2016, The Royal Society of Chemistry.

Potentiometric acid–base titration is another useful technique that gives insight to the chemistry of defects in MOFs. In more detail, potentiometric titration can quantify and distinguish between distinct Brønsted sites and their pKa values. Klet et al. investigated several Zr-based MOFs such as UiO-66, MOF-808, and NU-1000.[61, 63] With UiO-66 (Zr and Hf) for instance, they obtained titration curves displaying three inflection points (see Figure 2.12, left panel). Three different pKa values were determined and assigned not only to the μ_3-OH groups already present in "defect-free" UiO-66 but also to the values matching the acidity of metal-bound hydroxo and aqua ligands. The authors assumed that the occurrence of these species originates from missing linker defects (see Figure 2.12, right panel).[63] In comparison to commonly used TGA, potentiometric acid–base titration is not sensitive toward typical TGA-related conflicting issues such as inconclusive on- and offset

temperatures, the formation of non-volatile carbonaceous products, or incomplete activation procedures.[23] However, potentiometric titrations have practical issues, too. For example, inconsistent reproducibility and challenging data interpretation, for similar pK_a values, flat titration curves, and diffusion limitations, may be of concern. Furthermore, a high stability of the MOF toward acids and bases is a prerequisite for the measurement and limits its applicability.

Electron paramagnetic resonance (EPR) is also a useful technique to access the chemistry of defects in MOFs due to its high sensitivity. A. Pöppl and co-workers used this technique to precisely characterize the ligand environment of Ni^{2+} ions in flexible DUT8 (Ni).[64] In their work they used the small nitric oxide (NO) as a magnetic probe to investigate the adsorption properties as well as the local adsorption sites of NO in DUT-8 (Ni). The NO molecule is accessible by EPR since it has one unpaired electron in an antibonding molecular 2Π state. In particular, the lowest rotational level of the $2\Pi_{3/2}$ state of the free NO molecule allows the detection of even small amounts of desorbed NO gas in adsorption experiments.[64] The authors were able to distinguish up to five different signals coming from defective site of the flexible and rigid material which can be attributed to NO molecules forming paramagnetic complexes with the Ni^{2+} ions. These might be defective species since in principle "defect free" DUT-8 (Ni) offers no open coordination sites for NO. Furthermore, the density of these species is one order of magnitude higher in the rigid material than in the flexible material. In particular, only for the rigid defective DUT-8 (Ni) material two Ni^{2+}–NO adsorption species were observed. For these two species, the unpaired electron resides in a dz^2 orbital of the Ni^{2+} ion instead of the $dx^2 – y^2$ orbital, where it resides for the flexible material. A model where one NO molecule bonds in the equatorial plane of a defective paddlewheel unit to the Ni^{2+} ion can explain the two species. This implies that at least one NDC linker (2,6-naphthalenedicarboxylate) does not coordinate to these units. The absence of some linkers in the rigid DUT-8(Ni) might decrease the total attractive force between the ligands originating from π-π stacking. This could also explain why rigid DUT-8 (Ni) stays porous even in the absence of adsorbates.[64]

2.3.3 Properties of defective MOFs

MOFs with their porosity and available Lewis acidic sites implicate the application of these in heterogeneous catalysis and gas adsorption. Consequently, much focus was put on these two applications since their discovery and more recently focus was put on how the

introduction of defects can improve the performance of a parent MOF. In this context and for the scope of this thesis we will discuss mainly of these two applications. It is worth to mention that these are not the only applications that defective MOFs are used for. In fact, in recent years various reports have been published were defective MOFs have been used for decontamination of chemical warfare agents (CWA) and in generals hazardous gasses,[65-67] dye uptake and degradation,[68] increased hydrophobicity[69] and charge transport,[70-71] just to name a few.

2.3.3.1 Catalysis

A good example of how the catalytic activity of a parent MOF can be enhanced is shown in the work of Zhang et al.[72] The authors applied the solid solution approach in ruthenium analogs of $[Cu_3(BTC)_2]_n$ (HKUST-1), Ru-MOF to create defects. By using ditopic instead of tritopic linkers, under-coordinated and formally reduced $Ru^{\delta+}$ sites were obtained, which can act as soft Lewis acid sites. In the dimerization of ethylene the defect engineered Ru-MOF sample containing 32% of 5-OH-ip (5-hydroxy-isophthalate) linker revealed a two-fold increase in the turnover frequency, when compared to the parent Ru-MOF. A similar trend was observed in the Paal-Knorr reaction, which similarly relies on the presence of Lewis acid sites. As expected, the catalytic activity of the OH-ip functionalized defective Ru-MOF samples were found to be superior to the un-functionalized parent Ru-MOF. Another compelling example was performed by Llabrés and co-workers.[73]

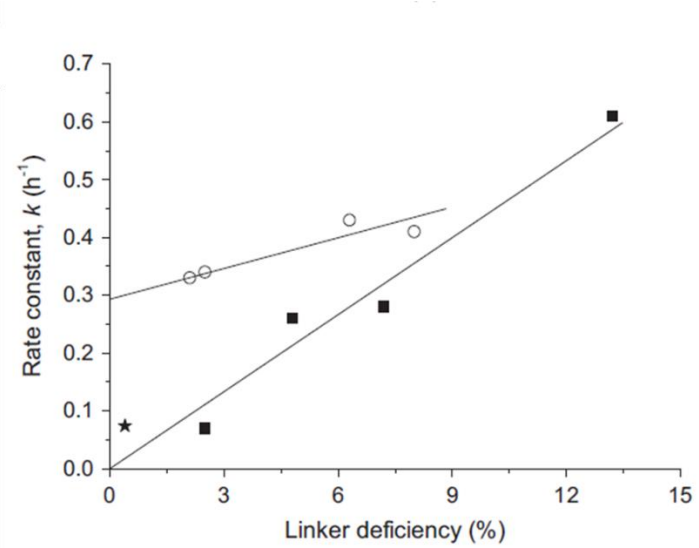

Figure 2.13: Rate constant k as a function of linker deficiency. Close symbols refer to UiO-66 sample while open symbols refers to amino functionalized UiO-66. Reprinted with the permission of ref. [73] Copyright 2015 Elsevier.

In their work, NH_2-UiO-66 and UiO-66 (UiO-66 with 2-amino-1,4-benzenedicarboxylate as linker) were used as solid acids in the esterification reaction of levulinic acid, whereby the number of missing linker defects inside UiO-66-NH_2 were estimated by using TGA. It was found that the rate constant correlates with the linker deficiency of the investigated systems (see Figure 2.13), demonstrating the strong impact of defects on the catalytic performance. The correlation of defects and catalytic activity was also reported by Hupp and co-workers, whereby the acid-catalyzed epoxide ring opening of styrene oxide was examined as a test reaction.[63] They studied a series of Zr/Hf-based MOFs, namely UiO-66, UiO-67, PCN-57 (porous coordination network), NU-1000, and MOF-808, quantifying the number of defects by using potentiometric titration. The authors showed that the catalytic activity can be attributed to defective sites and/or the connectivity of the Zr_6/Hf_6-clusters. Interestingly, defect-free Zr-UiO-67 exhibits almost no catalytic conversion, while defective Zr-UiO-67 (HCl as modulator) with 1.75 missing Linkers per Zr_6 cluster shows a catalytic conversion of ≈40% after 24h. Moreover, NU-1000 and MOF-808 were found to be significantly more active catalysts due to their intrinsic lower connectivity of 8 and 6 Linkers per Zr_6 cluster and more exposed Zr_6-nodes bearing additional -OH/-H2O groups. Notably, there is a conceptual difference in engineered defects using modulators and as proposed by the authors "inherent defects" that are defined as deviations from the fully coordinated Zr_6 clusters (12 linkers per Zr_6 cluster) with lowered connectivity (8 or 6 linkers per Zr_6 cluster).

2.3.3.2 Gas adsorption

It has been more and more recognized that the intrinsic adsorption properties can be tuned due to the introduction of new functional groups that can impact the interaction with different adsorbents such as H_2, CO_2, and CH_4. Similarly, defects with their ability to alter the chemical functionalization of pores have been recognized to play a key role in adsorption processes. A stunning example was reported in 2016 by Szilágyi et al.. The authors reported an enhanced methane adsorption uptake by 33% of the post synthetically treated MIL-101(Cr) compared to the pristine MOF.[74] In their work, they introduced NH_2-BDC^{2-} (BDC^{2-} = 1,4-dicarboxylate) via SALE and were able to exchange up to 20% of the original BDC^{2-} linkers. However, the dramatic increase in CH_4 uptake could not be explained by the introduction of new adsorption sites by the amino-functionalized linkers. The authors conclude that structural lattice point defects (see figure 2.14) such as dangling linkers and missing linkers (linker vacancy) play an important role in the way that these defects open

the pore windows of the MIL-101 superclusters, so the voids become more accessible for CH_4.

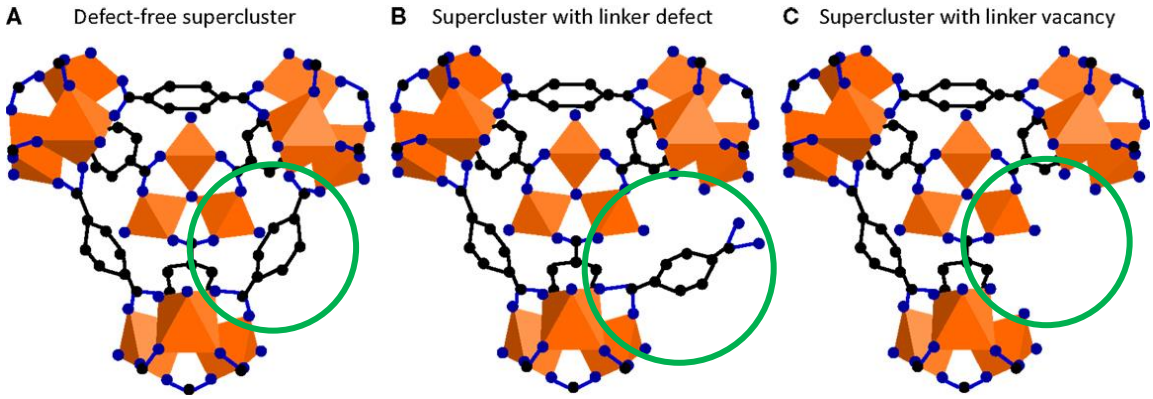

Figure 2.14: Different MIL-101 supercluster are shown (green circles) with: A) no defects, B) dangling linker, and C) linker vacancy. The orange polyhedra represent the cationic units, where C and O atoms are depicted in black and blue, respectively. Reprinted with the permission of ref. [74] Copyright 2016 Szilágyi, Serra-Crespo, Gascon, Geerlings and Dam.

To exclude that only additional NH_2-BDC contributes to the increase in uptake, fully substituted NH_2-MIL-101 was used as a reference system that shows a slightly reduced uptake. This is a remarkable example demonstrating that small changes, such as structural point defects, can in fact have a large impact on the properties of the overall framework. Another example that concerns with framework modification for CO_2 adsorption was reported by Behrens et al.[75] In their study, they compared conventional electrical (CE) heating with microwave-assisted synthesis and studied the role of defects on the adsorption properties of differently functionalized imidazolate framework potsdam (IFPs). As already introduced, the formation of defects strongly depends on the applied synthesis conditions, whereby it is widely accepted that standard CE methods with long reaction times (usually days) allow for the growth of large crystals with a low defect density. The same group also applied microwave-assisted conditions, which led to shorter reactions times (30–60 min) and samples with higher defect densities. To study the influence of these integrated lattice defects, the CE- and MV-synthesized IFPs were tested in CO_2 physisorption experiments. The authors found that the MV-synthesized IFPs outperform the conventionally synthesized IFPs, indicating the impact of defects on the adsorption properties.

2.3.3.3 New applications of defective MOFs

Ín this section we will discuss briefly the new application that MOFs have been used for in the recent years. Decontamination/ detoxification of hazardous gasses is probably one of the most exciting application that MOFs have been used so far. In this context different strategies for increased detoxification have been investigated by Hupp and co-workers in the last few years. For instance, metal substitution (cerium-based UiO-66), MOF/polymer composites, enzyme immobilization, or detoxification via selective photo-oxidation have been developed.

The utilization of photocatalysis or enzyme encapsulation is a nice proof-of-concept for CWA detoxification; however, there seem to be many practical challenges that need to be overcome in the future, e.g., enzyme preparation and isolation or performing photo-catalytic reaction within gas masks is difficult to achieve. In the study by Plonka et al., the capture and decomposition of dimethyl methylphosphonate (DMMP), a Sarin simulant, by defective Zr-based MOFs, were investigated.[66] In particular, they have used UiO-66, UiO-67, MOF-808, and NU-1000 to study the capture and hydrolysis of DMMP vapor through a stream of air or helium. By applying several analytics such as PXRD, DRIFTS (diffuse reflectance infrared Fourier transform spectroscopy), and EXAFS, they unambiguously assigned DMMP adsorption occurring at CUS of the activated samples. Additionally, the authors studied the reaction mechanism of the decomposition of DMMP toward methyl methylphosphonate (MMPA) and methanol intensively. They correlate the activity with adjacent M–OH_2 and M–OH groups (see figure 2.15), which are absent in defect-free UiO-66.[66] Thus, the role of defects for detoxification is crucial. It is envisioned that further synthesis optimization via defect engineering could be done for this purpose in the future. For instance, the modulator approach would lead to both higher adsorption capacities and faster hydrolysis, which might lead to a better performance in decontamination. The resulting MMPA shows a desorption energy from Zr centers of >100 kJ mol^{-1}, leading to irreversible adsorption at ambient conditions.

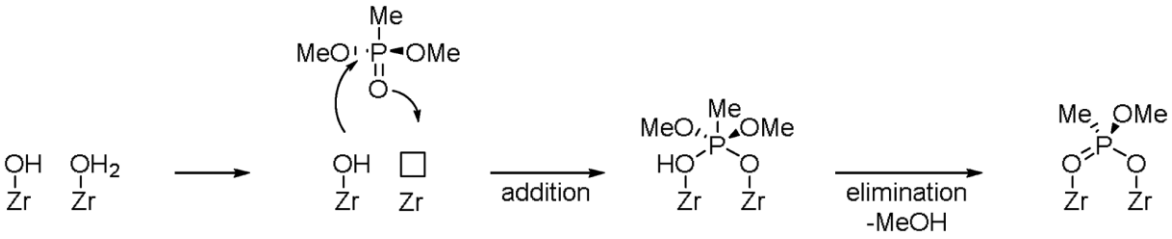

Figure 2.15: Proposed schematic representation of DMMP degradation mechanism assumed in ref. [66] Reprinted with the permission of ref. [40] Copyright 2018, John Wiley & Sons.

Another stunning example of detoxification of dangerous compounds such as organoarsenic molecules e.g., roxarsone (ROX), have been done by B. Li et al. in 2016. These molecules are used as feed additives but can be degraded into more toxic inorganic arsenic compounds that have already been found in meat and drinking water.[67] To date, there is no effective therapeutic treatment for arsenic poisoning and hence there is considerable interest in new decontamination procedures. B. Li et al. have used defect engineering in MOFs to obtain UiO-66 samples that show an increased adsorption behavior for ROX in aqueous solution.[76] They have used benzoic acid as modulator for the synthesis of defective (Zr) UiO-66. As expected, they observed an increase in BET surface from 600 $m^2\ g^{-1}$ ("defect-free" sample) to 1568 $m^2\ g^{-1}$ (20% modulator content related to BDC). Subsequently, the authors investigated important process parameters such as contact time, adsorbate concentration, pH as well as adsorption capacities. A formation of reactive Zr-OH groups as a result of missing linker defects mostly contributes to ROX adsorption and thus peaks in the 20% modulator sample. These additional binding sites lead to capacities up to 730 mg g^{-1}. The reduced adsorption equilibrium times, 30 min compared to 240 min for "defect-free" UiO-66, were related to the presence of mesopores. A pH value of 4 turned out to be superior to more basic conditions regarding the ROX adsorption capacity. The authors explained this trend with an increasing electrostatic repulsion between negatively charged adsorbent and the ROX anions at higher pH-values. A negative influence of electrolytes such as common salts on binding affinities was also investigated and could be excluded. Reusability was proven and includes an almost complete release of ROX in diluted hydrochloric acid after each cycle.

2.3.4 Guests inside MOFs

There is one last aspect, on defective MOFs that might be worth to be discussed briefly in this chapter. The introduction of guest molecules inside MOF frameworks, e.g. metal nanoparticles (NPs) or more simply, compounds that are not part of the MOF itself.

In general, guest molecules are introduced into MOFs via different methods, e.g liquid impregnation, chemical vapour infiltration (CVI) or double solvent approach (DSA).[77]* When these molecules due to their dimensions do not fit in the cavity size provided by the MOF, i.e. pores, they will create most likely, a local mismatch/irregularity in the crystal pattern and thus they can be considered as defects. A perfect example that we will discuss later in the thesis (see chapter 5), is the encapsulation of preformed NPs via the bottle around the ship method, which imply, as the name suggest, the construction of the MOF around the NPs introduced in the MOF synthetic solution. In other words, these metal NPs act as seeds and provide a base where to start the nucleation (construction) of the MOF framework. It is apparent, that this encapsulation will create an interface between NPs and the MOF. This, most likely, will play a crucial role in the reactive properties of these composite material and will require a detailed characterization. However, this level of characterization, requires accuracies that hardly can be achieved by common laboratory instruments and therefore makes intrinsically difficult to study this type of defects/interface.

After this brief introduction on the effect that defects have in MOFs, it is apparent that these new porous materials have in future many different possible applications that hardly can be found in any other material. However, from these chapters is also clear that research of defects in MOFs is more application driven than structure –property driven. In recent years scientists realized that to uncover and understand more deeply the nature of defects and their incorporation, research need to focus more on experiments that try to shed light on the effect that defects have in the MOF structure and consequently in their physical-chemical properties. This is not an easy task due to the amount of characterization techniques required, and luckily computational scientist come to aid experimentalists in helping them to screen which are the more probable effects that defects can have in the material. In the next chapters, i.e. the result part, we will see how physical, mechanical and reactive properties of UiO-66 change with increasing amount of defects.

*For further details on the topic please see the review article in ref.[77]

3 Using water adsorption measurements to access the chemistry of defects in the metal-organic framework UiO-66.*

Abstract

Defects in metal-organic frameworks are gaining much attention due to their strong impact on MOFs reactive properties. In this chapter, a series of defective UiO-66 samples have been analysed for the first time with water adsorption measurements. Precious insights into the reactivity of the Lewis acid sites generated by the modulation approach have been quantified through the calculation of the Henry constant and the saturation water uptake. In particular, the result shows that the defect-induced hydrophilicity, which is quantitatively expressed by the Henry constant, correlates well with the catalytic performance in a Lewis acid based reaction used as a test reaction.

*Parts of the results of this chapter are published and reproduced with permission from: Dissegna, S.; Hardian, R.; Epp, K.; Kieslich, G.; Coulet, M.-V.; Llewellyn, P.; Fischer, R. A., *CrystEngComm* **2017**, 19 (29), 4137-4141.

3.1 Introduction

Metal–organic frameworks (MOFs) are a fascinating class of materials that offer ample opportunities in the research areas of catalysis, gas adsorption, gas separation and related fields.[77-80] As already described in the introduction part, MOFs are porous materials composed of interconnecting inorganic and organic moieties,[6, 81] which can be tuned to meet certain requirements.[82] For instance, by varying the organic linker, many different structures with tuneable inner pore volumes, e.g. micro or mesoporosity, can be obtained.[27] Initially, MOFs have gained a lot of attention in the context of gas-storage applications; however, their thermal and chemical stability have limited possible (industrial) applications so far.[3, 21] A step forward in this context has been made with Zr-based MOFs, e.g. UiO-66 and PCN-222,[22, 29, 83] which are stable in most chemical solvents with decomposition temperatures as high as 400 °C.[84] When dealing with crystalline materials, defects and disorder are steady companions at temperatures above 0 K. Recently, it has been recognised that defects can be used to alter the properties of MOFs, especially their catalytic activity and sorption behaviour.[43, 56, 63, 85-87] For instance, defective Zr-based MOFs have been used as Lewis acid catalysts in various reactions, including MPV reduction,[44] esterification,[73] hydrogenation of aromatic compounds,[88] epoxide ring-opening reaction and others.[63] Despite the large interest of the community in this field, there is a current debate on what is the most effective set of experiments to determine the nature of defects, e.g. concentration, type of defects and their chemistry. Our work follows on from the important findings of Vermoortele[44] and Wu,[89] who used different modulators, e.g. acetic acid (AA) and trifluoroacetic acid (TFA) for the incorporation of defects in UiO-66. Here, we use varying amounts of AA and TFA as modulators to prepare UiO-66 samples with an increasing amount of defects.[42, 44, 89] Subsequently, water sorption measurements were performed to elucidate the chemistry of the incorporated defects, in particular their hydrophilicity which can be directly linked to their Lewis acidity. Additionally, we use the cyanosilylation of benzaldehyde as a catalytic test reaction to probe the Lewis acidity of the defects in UiO-66 directly.

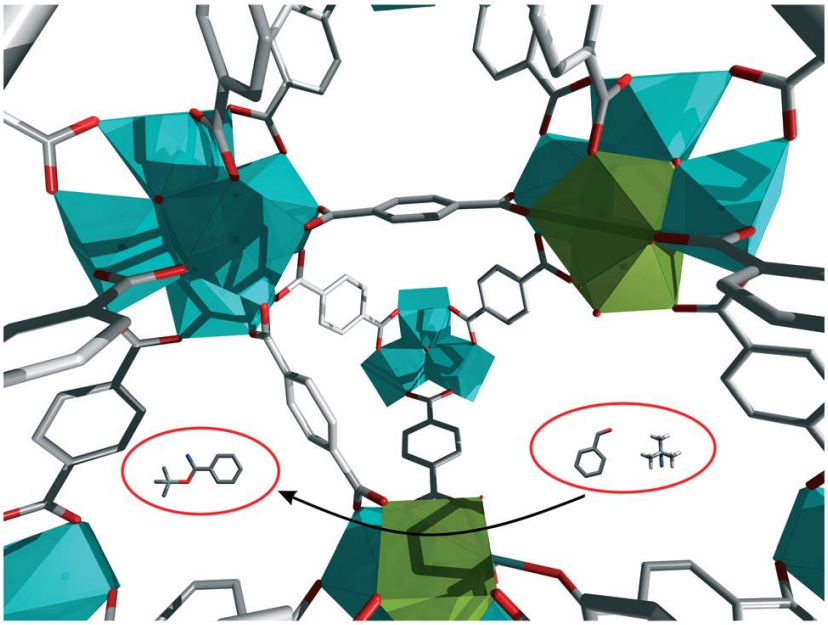

Figure 3.1: Illustration of the catalytic cyanosilylation of benzaldehyde on a Lewis acidic missing-linker defect in UIO-66. Green polyhedra: clusters with missing linker defects; light blue polyhedra: ideal Zr_6 clusters.

3.2 Characterization of defective UiO-66 with water adsorption measurements and other characterizations techniques.

Synthetically, 16, 33, 67 and 100 equivalents of AA with respect of zirconia were used to prepare defective UiO-66 and samples are denoted as 16AA, 33AA, 67AA, 100AA, respectively. For TFA as a modulator, 1 and 10 equivalents were used and the samples are denoted as 1TFA and 10TFA. Unmodulated UiO-66 (UiO-66 ref) was also synthesized as a reference sample, following a modified procedure reported by Shearer et al. [25] and the details of the synthesis conditions can be found in the experimental section.

After synthesis, the phase purity of all the samples was confirmed using powder x-ray diffraction (see figure 3.2 and 3.3).[22, 25] Additionally, we like to note that no intensity in the low theta region (2 – 6 θ°) was observed which would indicate the presence of correlated defects in UiO-66 as observed by Goodwin and co-workers.

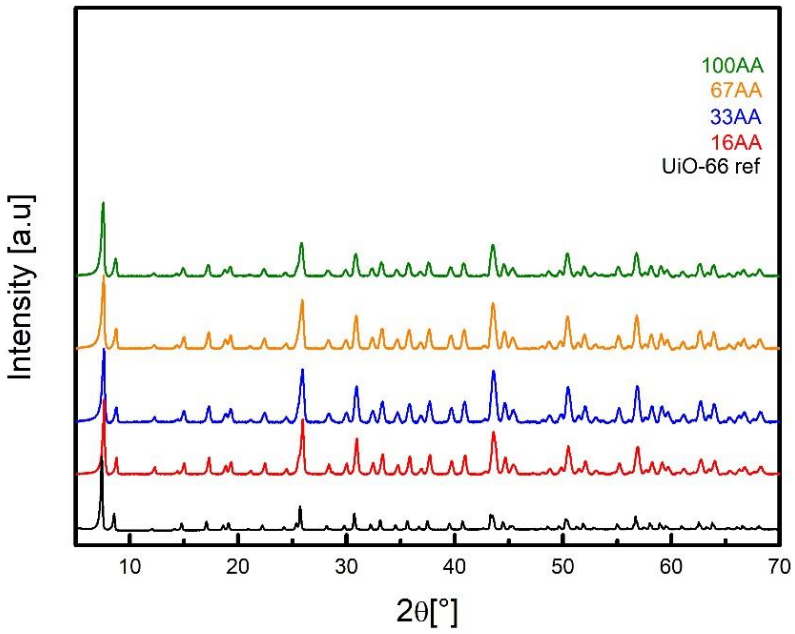

Figure 3.2: PXRD patterns of UiO-66 ref (black), 16AA (red), 33AA (blue), 67AA (orange) and 100AA (olive green) of AA**.**

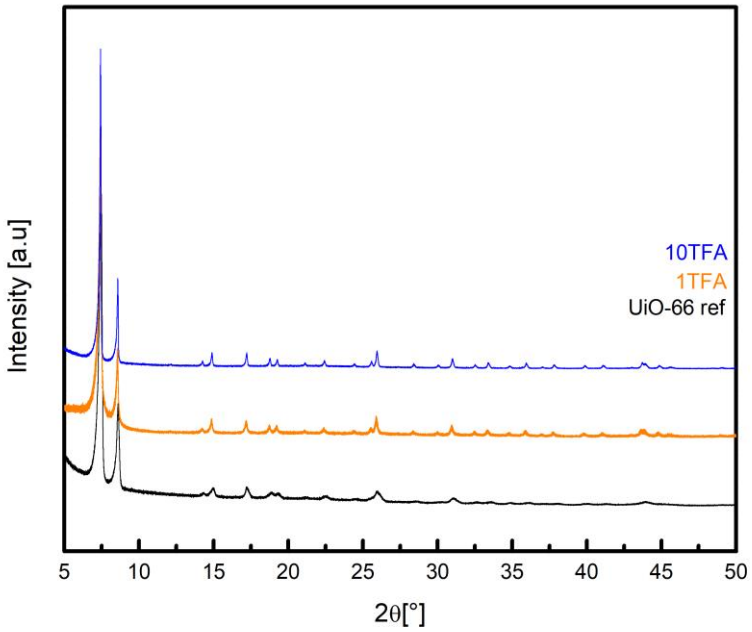

Figure 3.3: PXRD patterns of UiO-66 ref (black), 1TFA (orange), 10TFA (blue) of TFA.

Moreover, thermogravimetric analysis (TGA) was performed for all samples, and the results were compared to UiO-66 ref in order to investigate the effect of the incorporated amount of modulator and the thermal stability (see figure 3.4 and 3.5).

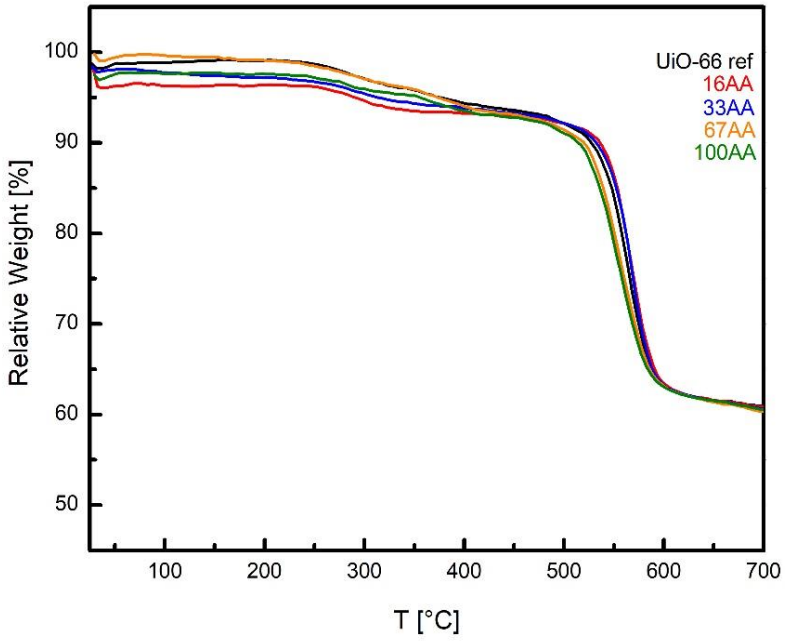

Figure 3.4: Thermogravimetric analysis measured under Ar atmsphere (TGA) of of UiO-66 ref (black), 16AA (red), 33AA(blue), 67AA (orange) and 100AA (olive green) of AA.

For samples with AA as modulator, a typical weight loss at approximately 250 - 300 °C is observed which corresponds to the dehydroxylation of Zr clusters. At approximately 500 °C, a second weight loss is observed, which was previously assigned to linker decomposition in pure UiO-66.[89] In contrast to that, the defective UiO-66 samples prepared with TFA as modulator exhibit a multistep curve in the TGA. The weight loss at temperatures below 320°C can be assigned to different processes like dehydroxylation of the Zr cluster and loss of the remaining solvent and formate molecules.[44] The weight loss step at 320 °C can be ascribed to TFA anions directly adsorbed on the CUS sites of the zirconium cluster. The first step qualitatively correlates with the amount TFA used in the synthesis. The thermal stability of these samples is approximately 50 °C lower, as compared to the reference.

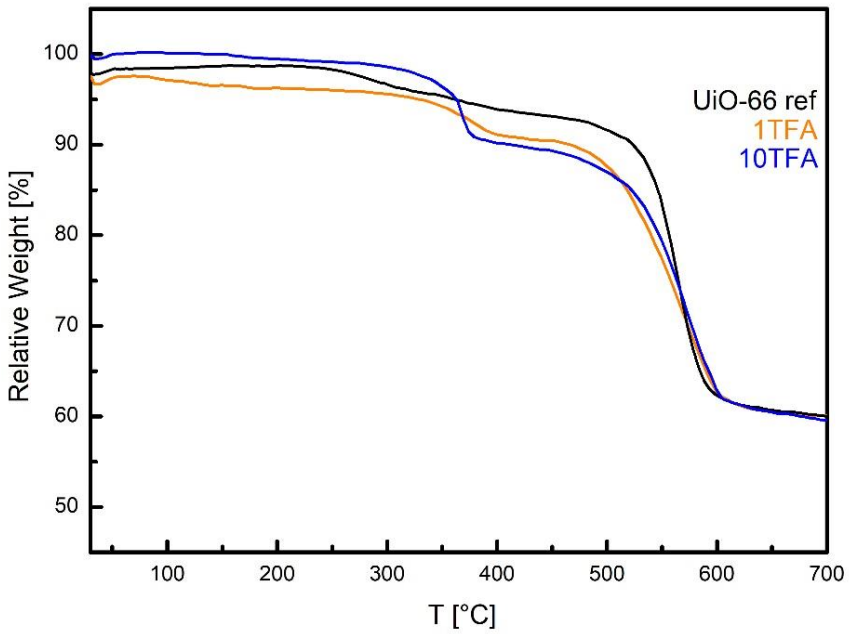

Figure 3.5: Thermogravimetric analysis (TGA) measured under synthetic air of UiO-66 ref (black), 1TFA (orange), 10TFA (blue) of TFA.

Furthermore in order to access the porosity of the samples, N_2 physisorption measurements were also performed, showing type I isotherms, which is typical for microporous MOFs such as UiO-66 (see figure 3.6 and 3.7). Importantly, for materials prepared with increasing quantities of the AA modulator, several trends can be observed as shown in Table 3.1. In particular, when TFA is used, the nitrogen isotherm data shows that the addition of either small or large amounts of modulator (1 and 10 mol equivalent) leads to a drastic increase of the BET surface area and pore volume. This might suggests that TFA creates more defective samples than AA.

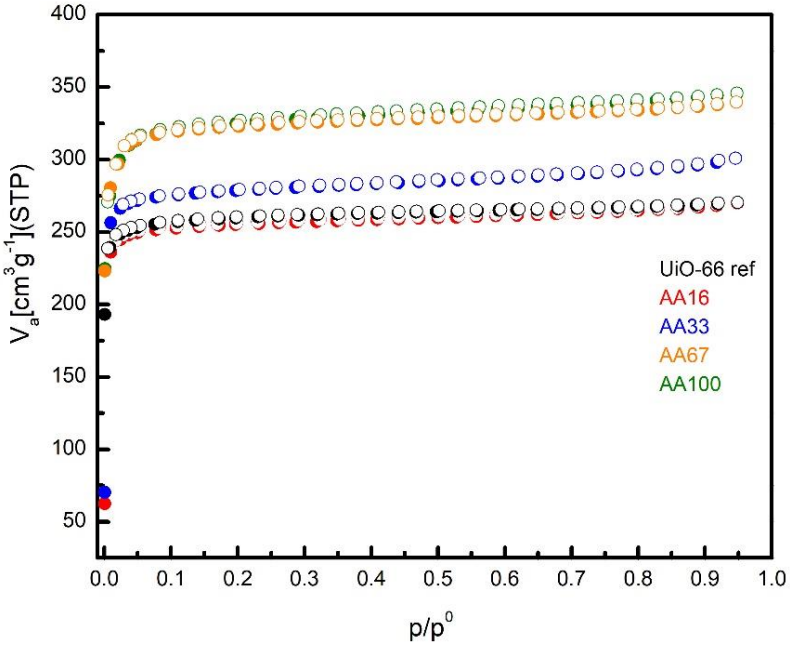

Figure 3.6: N_2 adsorption measurements (77K) of defect free UiO-66 (black), 16AA (red), 33AA(blue), 67AA (orange) and 100AA (olive green) of AA.

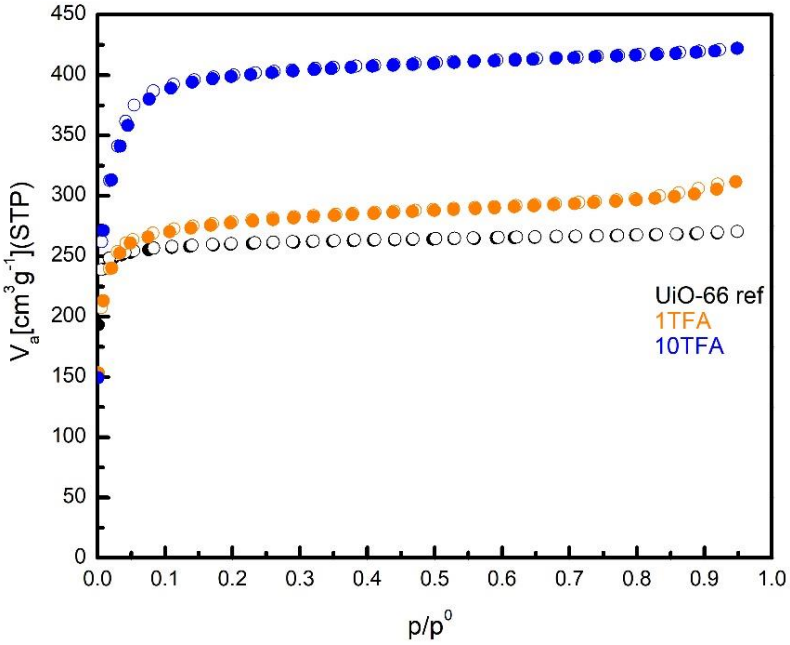

Figure 3.7: N_2 adsorption measurements (77K) of UiO-66 ref (black), 1TFA (orange), 10TFA (blue) of TFA samples. Close and open symbols for each sample are for adsorption and desorption respectively.

We now turn our attention to the core of this chapter, water adsorption measurements, which allowed us to access the chemistry of the defects, in particular their hydrophilicity. The water adsorption capacity can be determined as the water uptake at partial pressure close to the bulk saturation vapor pressure, $p/p^0 = \sim 1$, while the Henry constant, K_H, is a quantitative indicator of hydrophilicity. K_H corresponds to the slope of the water adsorption isotherm at very low coverage. [90] However, this approach is valid assuming an ideal adsorption system. For a more realistic adsorption system (non-ideal gas), an extrapolation of the virial plot* of ln(n/p) versus n can be adopted to obtain K_H, where n is the mol of adsorbed molecules and p is pressure at low coverage (see figure 3.8).[90]

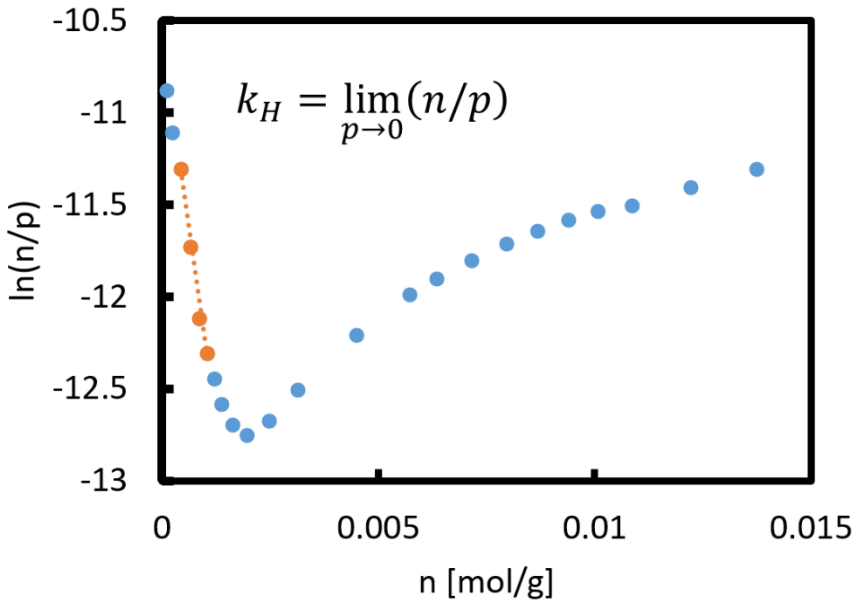

Figure 3.8: virial plot used to calculate the Henry constant at very low coverage. The points highlighted in orange were used in the calculation.

*The virial plot derives from the virial equation $\ln(n/p) = k_1 + k_2 * n + k_3 * n^2$... and continues as an infinite expansion where k_1 k_2 and k_3 are virial coefficients n are the moles of gas adsorbed and p is the pressure. This equation basically describes the non-ideal behaviour of the gas-adsorbent interaction. A way to express mathematically this tendency of p towards zero is the limit function $\lim_{P\to 0} \frac{n}{p}$, where the intercept extrapolated at p = 0 of this function gives the Henry constant.

Table 3.1: Summary of N_2 and water adsorption on UiO-66 ref and modulated UiO-66. In white background are depicted AA samples while TFA sample are highlighted in dark grey background.

	N_2 at 77K				H_2O at 298 K			
Sample	Modulator (eq)	BET (m^2/g)	PSD (nm)	Pore volume[a] (cm^3/g)	Pore volume[b] (cm^3/g)	Shape of isotherm	Henry constant[c] ($mol^{-1}\cdot g\cdot Pa^{-1}$)	Max water ads capacity (cm^3/g)
UiO-66 ref	0	1068	1.16	0.37	0.35	2 steps	$2.04*10^{-5}$	495
16AA	16 AA	1131	1.2	0.38	0.37	1 step	$1.52*10^{-5}$	519
33AA	33 AA	1191	1.2	0.41	0.40	1 step	$2.49*10^{-5}$	556
67AA	67 AA	1314	1.2	0.47	0.44	1 step	$2.27*10^{-4}$	603
100AA	100 AA	1334	1.2	0.50	0.48	1 step	$7.58*10^{-4}$	650
1TFA	1 TFA	1100	1.2 & 1.5	0.40	0.39	2 steps	$3.52*10^{-4}$	528
10TFA	10 TFA	1567	1.2 & 1.5	0.59	0.55	2 steps	$7.12*10^{-4}$	740

[a] Pore volume determined with N_2 adsorption. [b] Pore volume determined with water adsorption, PSD = pore size distribution. [c] A Henry constant value in the order of 10^{-7} corresponds to very hydrophobic materials, while values in the order of 10^{-3} correspond to very hydrophilic materials. For further information please see ref. [91] where other Henry constant values for different types of MOFs are reported.

The water adsorption isotherms of the UiO-66 ref and the AA modulated UiO-66 are presented in figure 3.9. The parameters calculated from these isotherms obtained at 298 K are tabulated in Table 3.1. It is worth nothing that the Gurvitch rule[90] is satisfied since the pore volume obtained with nitrogen at 77 K is comparable with the one obtained with water at 298 K. However, slightly lower values of the pore volume are systematically obtained by water sorption which may be explained by the presence of hydrophobic domains within the pores that may repel H_2O molecules, thus avoiding complete pore filling.[92] The very low pressure region of the isotherms (see figure 3.9) were used to determine the Henry's constant. Interestingly, as can be seen from Table 3.1, this constant increases with increasing amount of AA. This suggests that AA makes a more hydrophilic surface, because of the missing linker defects which allow the metal site to be more accessible. Furthermore, simulated water sorption isotherms of UiO-66 with missing linker defects indicate an increased hydrophilicity, which is in agreement with our experimental work. [93] Interestingly, two steps are observed in the second part of the water adsorption isotherm (range of partial pressure 0.25 to 0.4) for UiO-66 ref. This finding is in agreement with the work of Canivet et al.; however, other studies did not observe a similar feature.[26, 31, 91, 94-95] Nevertheless, the

observation of this step-like behaviour seems to be highly dependent on the number of data points obtained during water adsorption measurement in the appropriate range of p/p^0 = 0.2–0.4. In earlier works, this behaviour was linked to the dual pore size distribution in UiO-66, and thus is characteristic of the pore filling of the tetrahedral (0.7–0.8 nm, first step) and octahedral (1.1–1.2 nm, second step) cavities respectively.[92] In our UiO-66 ref sample, two pore sizes are confirmed by water adsorption but not by N_2 adsorption measurements due to the insufficient data points at the very low p/p^0 region. Nevertheless, the addition of AA leads to the disappearance of the first step, suggesting that AA preferentially attacks the smaller pores and enlarges them. Thus, a narrower pore size distribution with only a PSD comparable to that of the octahedral pores can be found for the modulated samples. Furthermore, in the last part of the water sorption isotherm (above p/p^0 = 0.8), the maximum water uptake can be observed, and thus the total pore volume can be calculated. These values also increase as the modulator concentration is increased (Table 3.1). This can be explained by the additional pore space generated by the defects. [31]

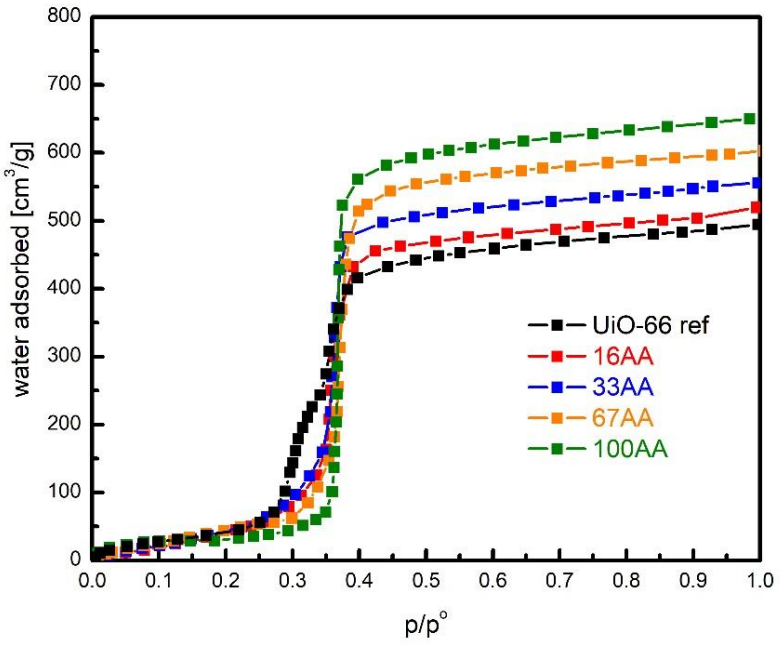

Figure 3.9: water adsorption isotherm of UiO-66 ref in black, 16AA in red, 33AA in blue, 67AA in orange and 100AA in olive green.

Similar to AA, in the TFA case, the Gurvitch rule[90] is verified since the pore volume obtained with water at 298 K is comparable to the one obtained with nitrogen at 77 K. Similarly, the Henry's constants were evaluated for the TFA samples, and we found that the

TFA samples are more hydrophilic than the UiO-66 ref and the AA modulated samples. Interestingly, the shapes of the isotherms are more complex for the TFA-modulated samples (see figure 3.10). Indeed, in the range of p/p^0 0.3–0.5 for both TFA samples, two steps can be clearly observed. This behaviour seems to be more prominent than in the UiO-66 ref sample. This may indicate that TFA does not attack preferentially the smaller pores but rather enlarges both cavities. Another interesting observation from the water adsorption experiment on the TFA modulated UiO-66 is the onset of a third step around $p/p^0 \sim 0.8$. Since we did not observe this step in UiO-66 ref and in the AA modulated UiO-66, we can propose two interpretations of this effect. (i) This step is related to the creation of a third pore size distribution that results from the merging of some of the two other micropores, or (ii) this is linked to the outer surface or interparticle condensation.[92] To propose a possible mechanism, it is worth noting that the weakest point in the UiO-66 structure is the bond between the benzene rings and the terminal carboxyl group in the BDC linker.[22] In the case of the AA modulator, the BDC linker is replaced by AA, whereas in the case of TFA modulated UiO-66, the replacement of BDC by TFA is followed by the removal of TFA upon activation.[44]

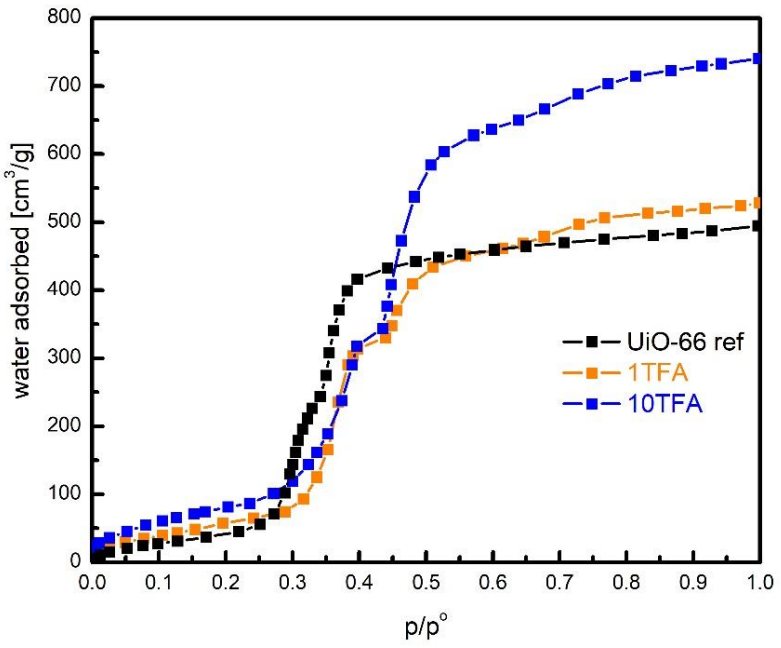

Figure 3.10: water adsorption isotherm of UiO-66 ref and TFA-modulated UiO-66 samples depicted in black for UiO ref, orange for 1TFA and blue for 10TFA samples.

This may create larger cavities and more hydrophilic unsaturated zirconium metal sites. Another possible explanation for the water adsorption isotherm depicted in Fig. 3.10 might be due to the nature of the zirconium metal site that could undergo reversible structural rearrangement upon activation and introduction of water vapor.[22, 26] In the case of UiO-66 ref, it is known that the as synthesized UiO-66 can readily contain some missing linkers,[96-97] and the zirconium metal cluster might exist in the hydroxylated and dehydroxylated forms, probably due to the incomplete activation process. This coexistence could lead to the reversible structural rearrangement upon water adsorption and the readily available missing linkers were terminated by water molecules during water adsorption processes. This termination process, thus, could induce a step in the isotherm. In the case of AA-modulated UiO-66, there is no step observed in the middle range of the partial pressure of water adsorption. This might be linked to the addition of AA that does not only replace some of the BDC linkers but also terminate the readily available missing linkers. Therefore, there is no water-induced missing linker termination during water adsorption and in turn, no step is observed in the isotherm. In the case of TFA-modulated UiO-66, the replacement of some BDC linkers by TFA is followed by the removal of TFA upon activation.[44] This creates a bigger cavity and the zirconium metal sites are more exposed to water. In this case, structural rearrangement is more likely to happen and water-induced missing linker termination is required to maintain the charge balance in the defective structure. Therefore, the step in the water adsorption isotherm is more pronounced, representing a combination of effects between the presence of two pore sizes (as evidenced from the nitrogen adsorption measurement) and the reversible structural changes upon defect termination by water molecules.

3.3 Catalytic testing of defective UiO-66

Lastly, in order to check if the created defects produce a material with more Lewis acid sites, we chose the cyanosilylation of benzaldehyde as a test reaction, which requires the presence of such Lewis acid sites (Scheme 3.1). This reaction of carbonyl compounds with trimethylsilyl cyanide (TMSCN) is one of the very important transformations that allow the formation of the C–C bond and the protection of a hydroxyl function.[98] Cyanohydrin product produced by the cyanosilylation can be further transformed into important synthetic intermediates such as α-hydroxy acids, α-amino acids, and β-amino alcohols, which are widely applied in the chemical industry. [98]

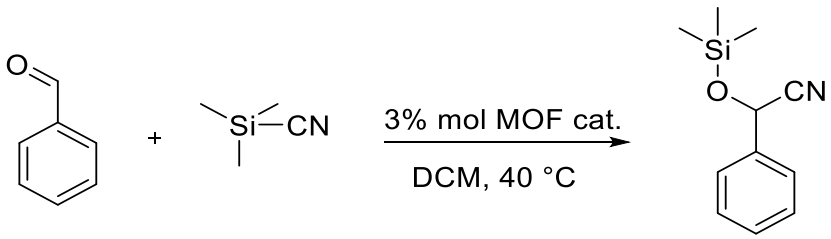

Scheme 3.1: Cyanosilylation of benzaldehyde with trimethylsilyl cyanide (TMSCN) in CH_2Cl_2 (DCM) to give the corresponding cyanohydrin under the Lewis-acidic Zr UiO-66.

In accordance with our expectation, the defect engineered TFA-modulated samples reveal a significantly higher catalytic activity when compared to their "ideal" UiO-66 counterpart, which is considered as defect-free. Notably, a slight induction period is observed at the beginning of the reaction, which can be attributed to the reversible formation of a benzoin condensation product (see figure 3.11).

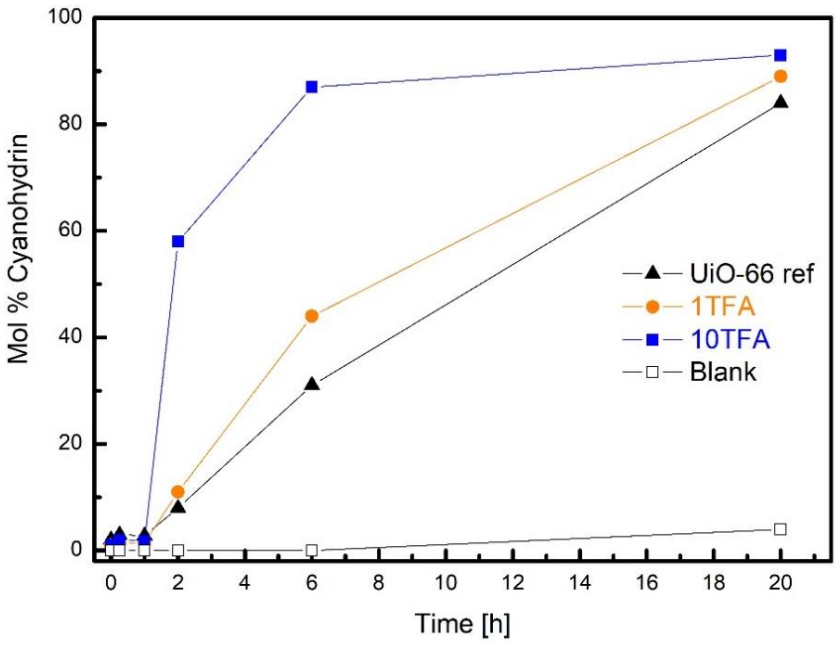

Figure 3.11: Time-Yield plot of the cyanohydrin produced by the cyanosilylation of benzaldehyde with trimethylsilylcyanide (TMSCN) catalyzed over 10TFA (blue squares), 1TFA (orange circles) and UiO-66 ref (black tringles) samples in comparison to the blank sample (black, open squares), in which no catalyst was used.

Moreover, the catalytic activity nicely correlates with the degree of TFA modulation, whereby the created defects and the lowered coordination number of the Zr_6 clusters cause an improvement in the reaction rate. However, it is unclear if the drastic impact on the

catalytic activity is only caused by the defect sites and/or by the increased surface area of the TFA-modulated samples which should also help to overcome diffusion limitations. Most likely, both phenomena contribute to the boost in the catalytic performance. Furthermore, all the tested catalysts show excellent stability to the applied reaction conditions and could be recycled for at least two consecutive catalytic runs, which is confirmed by PXRD (see figure 7.19 and Table 7.7 in the experimental section). In order to investigate the heterogeneity of the underlying reaction, a hot-filtration test was conducted which revealed that the reaction was cancelled after the catalyst was separated from the reaction solution. (see figure 7.20 in the experimental section).

3.4 Conclusions

In this chapter, we investigate water adsorption measurements as a key tool to study the generated defects in AA and TFA modulated UiO-66 samples. We found that increasing the amount of the modulator causes an increase in the surface area (BET), total water uptake and hydrophilicity, especially in the TFA modulated samples with respect to unmodulated UiO-66 sample. By this modulation approach, it is possible to increase the hydrophilicity, which is reflected by the Henry constant, of UiO-66 by one order of magnitude. Furthermore, we want to highlight that it is possible to link the hydrophilicity and the catalytic activity. Therefore, we chose the cyanosilylation of benzaldehyde as a test reaction, which exploited the Lewis acid sites generated by missing linker defects. Hereby, we found that increasing the amount of TFA has a beneficial effect on the catalytic activity. In conclusion, we would like to introduce water adsorption measurement as a complementary characterization method in order to access the chemistry of defects. Compared to other techniques, it offers a direct way to measure the hydrophilicity, which can be used to predict the catalytic properties for Lewis acid-based reactions.

4 Tuning the mechanical response of defective metal-organic frameworks.*

Abstract

Metal-organic frameworks have acquired a lot of attention in the recent years due to the wide spectrum of applications that these materials can be used for, ranging from catalysis to water harvesting systems, just to name a few. In particular, the intentional incorporation of defects into these porous crystalline materials have been shown to enhance macroscopic properties such as porosity and catalytic activity. Despite the vast interest on this topic, experimental studies that tackle the mechanical stability of defective MOFs are presently absent in the literature.

Therefore, in this chapter, high-pressure powder X-ray diffraction experiments are presented by varying pressures from ambient to 0.4 GPa, in order to probe the response of defective UiO-66 to hydrostatic pressure. The results shows an onset of amorphization in defective UiO-66 samples around 0.2 GPa and decreasing bulk modulus as function of defects. In particular, the observed bulk moduli of defective UiO-66(Zr) samples do not correlate with defect concentration, highlighting the complexity of how defects are spatially incorporated into the framework.

*Parts of the results of this chapter are published and reproduced with permission from: Dissegna, S.; Vervoorts, P.; Hobday, C. L.; Düren, T.; Daisenberger, D.; Fischer, Roland A.; Kieslich, G., *J. Am. Chem. Soc*. **2018**, 140 (37), 11581-11584.

4.1 Introduction

The ability to control structure-property relations in crystalline materials is at the heart of modern materials science.[1] In this pursuit, the targeted incorporation of defects is a crucial tool for fine-tuning properties throughout different areas of chemistry, such as condensed matter physics and materials science.[2, 99] It is therefore exciting to see that defect engineering has recently entered the field MOFs. MOFs are a relatively new class of crystalline materials, combining the versatility of organic chemistry with the library of inorganic metal nodes. The organic linker molecules bridge the inorganic building units to form 2D or 3D periodic networks often with guest-accessible porosity. The large chemical tunability in combination with the powerful concept of reticular chemistry in principle allows for designing MOFs to meet specific structural and chemical requirements.[6] In turn, MOFs offer great opportunities across many subjects of materials science ranging from catalysis,[43, 73, 100] sensors,[101] filters[11, 102] to water harvesting systems[8, 103] to name just a few. When considering the defect chemistry of MOFs in more detail, it was shown that macroscopic properties such as porosity and in turn catalytic activity and microscopic properties such as lattice dynamics are closely linked to the defect chemistry.[3, 40, 104] Furthermore, some MOFs such as ZIF-8 can be transformed to a porous amorphous state, with the absence of long-range order.[105-106] In the context of point defects in crystalline MOFs, $M_6O_4(OH)_4(BDC)_6$ (UiO-66, M = Zr and Hf and H_2BDC = 1,4-benzendicarboxylic acid) and similarly its dehydrated form $M_6O_6(BDC)_6$ are currently widely used in the community, owing to their high thermal and mechanical stability combined with a certain chemical robustness.[23] UiO-66 crystallizes in a face-centered cubic framework in fcu topology, with $[M_6O_6]^{12+}$ metal-nodes in 12-fold coordination of $(BDC)^{2-}$.[22] Synthetically, defects are typically incorporated by the so-called modulator approach, where high equivalents of mono-dentate acids such as formic acid, acetic acid and trifluoro acetic acid are added to the reaction mixture.[41-42, 44] For small amounts of modulators, crystallinity of the defect-free framework is enhanced, whilst large amounts facilitate the incorporation of modulators into the structure and the formation of Schottky-type defects. Importantly, it was shown that under certain circumstances defect incorporation can occur in a correlated fashion, producing nanoregions with reduced pcu symmetry.[107]

The permanent porosity and low density implicate that MOFs are soft materials.[108] The large chemical diversity together with the potential to form highly connected lattices, however, lead to bulk moduli that span in a range between K = 4 - 30 GPa.[109] In some cases,

hydrostatic pressure can trigger porous-to-nonporous phase transitions in flexible model systems such as ZIF-4(Zn) and MIL-53(Al) at pressures as low as 0.05 GPa, making MOFs potential working media in mechano-calorics and mechanical dampers.[110-111] In the absence of structural and thermodynamic requirements for a porous-to-nonporous phase transition,[112] MOFs are prone to undergo amorphization at relatively low pressures.[108] For instance, MOF-5 amorphizes irreversibly by direct compression at pressures below 3.5 MPa and ZIF-8 at 0.34 GPa.[113-114] Such insight is not only fascinating from a fundamental viewpoint, but also tackles application-oriented questions, e.g. stability-issues of MOFs during shaping processes for catalytic applications.[115]

Despite the on-going research interest in the field of defective MOFs, experimental studies that address their mechanical stability are presently absent in the literature. However, computational studies have been performed on UiO-66, its isoreticular expansions UiO-67 and UiO-68, HKUST-1, ZIF-8 and IRMOF-1.[39, 56-58, 116-117] Focusing on UiO-66,[39] van Speybroeck and co-workers performed an insightful computational study on defective UiO-66, addressing questions concerning the thermodynamics of defective UiO-66 under hydrostatic pressures.

They find a small but significant impact of the spatial arrangements of defects on the onset pressure of amorphization and similarly the bulk modulus. Likewise, Thornton and co-workers highlighted the large parameter space of defective UiO-66, finding that highly defective UiO-66 with correlated defects (reo topology) exhibit a more stable structure compared to highly defective uncorrelated systems.

4.2 Evaluation of laboratory and high pressure powder X-ray diffraction data

Following on the footsteps marked by the computational results, we herein apply high-pressure powder X-ray diffraction (HPPXRD) to characterize the mechanical response of defective MOFs to hydrostatic pressure experimentally with a non-penetrating transmitting media for the first time.

Defective UiO-66(Zr) samples were prepared by using trifluoro acetic acid (TFA) as modulator. In detail, three defective samples with 1 (UiO-66-1eq), 5 (UiO-66-5eq) and 10 (UiO-66-10eq) equivalents of TFA with respect to the zirconia concentration were prepared.[44] Unmodulated UiO-66 (UiO-66-0eq) was also synthesized as a reference sample, following a modified procedure reported by Shearer et al.[42]

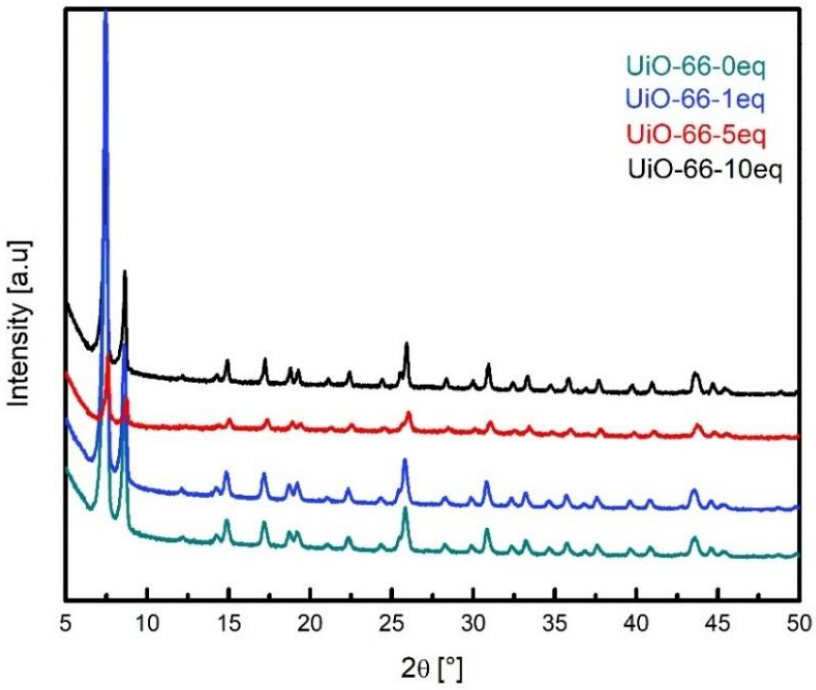

Figure 4.1: Laboratory powder x-ray diffraction pattern of UiO-66-0eq, UiO-66-1eq, UiO-66-5eq and UiO-66-10eq, shown in dark cyan, blue, red and black coloured lines, respectively.

After synthesis, powder x-ray diffraction was used to confirm phase purity for all samples (see figure 4.1). N_2 physisorption measurements were also performed to access the porosity of all samples, showing type I isotherms, which is typical for microporous MOFs such as UiO-66 (see figure 4.2). Interestingly, with an increasing amount of modulator there is also an increase of the surface area of the samples. This is in strong agreement with results present

in the literature, where the increased porosity has been ascribed to an increasing amount of defects incorporated in the UiO-66 frameworks.[42]

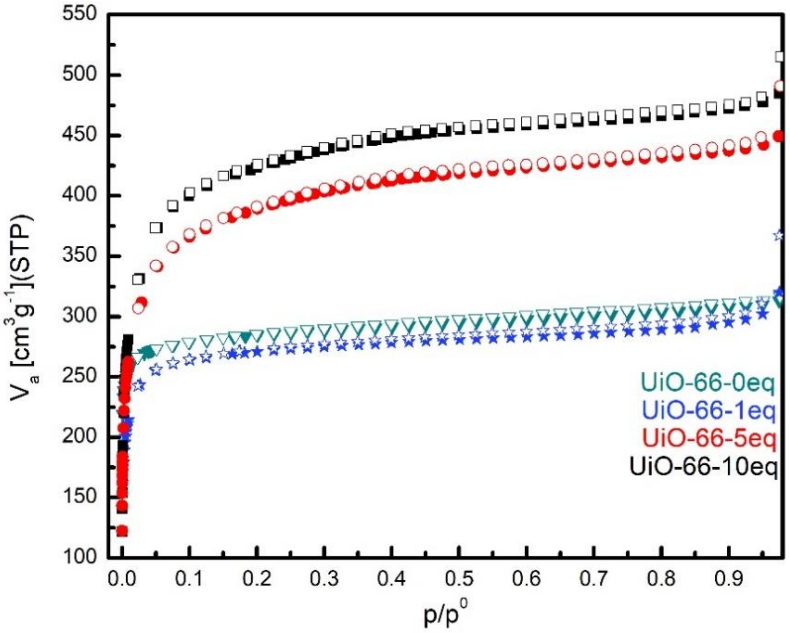

Figure 4.2: N_2 adsorption measurements (77K) of UiO-66-0eq, UiO-66-1eq, UiO-66-5eq and UiO-66-10eq, shown in dark cyan triangular, blue star, red circle and black squares shape symbols, respectively. Open and filled symbols are for adsorption and desorption branches, respectively.

Thermogravimetric analysis (TGA) was also performed to determine the thermal stability of the samples. The decomposition curve of UiO-66 can be divided into 3 different weight loss regions. The first one at 50-150°C, can be ascribed to the removal of a small amount of water and remaining solvent molecules from the MOF pores.

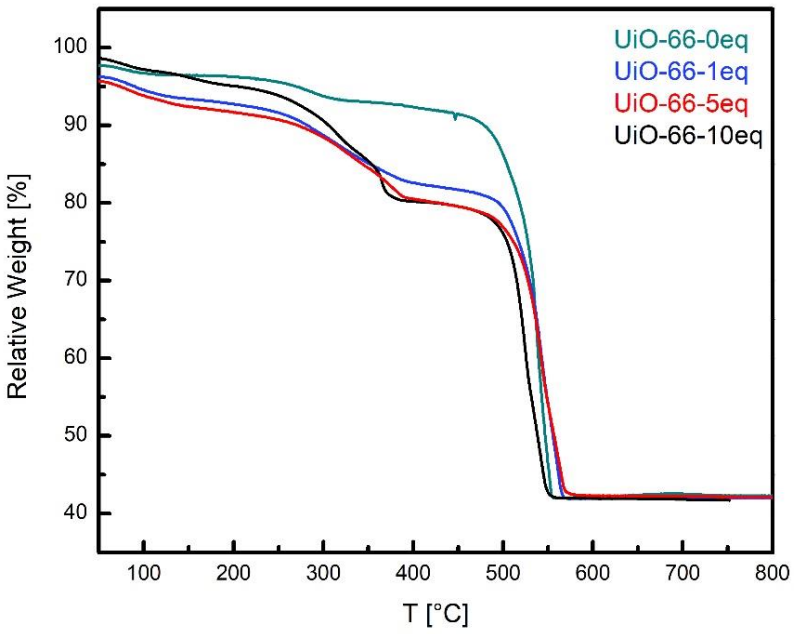

Figure 4.3: TGA of UiO-66-0eq, UiO-66-1eq, UiO-66-5eq and UiO-66-10eq, plotted in dark cyan, blue, red and black coloured lines, respectively.

In the second region, 150-450 °C, many different processes can occur. The weight loss step is a combination of three different processes: loss of structural water, or dehydroxylation of the Zr_6-oxo cluster between ≈ 200°C and 300°C,[23] loss of formate molecules in the same temperature range[42] and loss of TFA molecules above 300°C.[42] Lastly, the largest weight loss step in the range 420 - 600°C can be attributed to the decomposition of the BDC ligand molecules of UiO-66.

Moreover, a quantification of the defect concentration (see figure 4.3 and table 4.1) was performed using TGA data, according to the method proposed by Valenzano et al. (detailed description of the process is provided in the experimental section sub-chapter 7.1.4).[23]

A defective concentration of approximately 3% was found for UiO-66-0eq, whilst TFA modulated samples UiO-66-1eq, UiO-66-5eq and UiO-66-10eq show a defect concentration of approximately 22.5%, 26.6% and 28.3%, respectively. Assuming only linker defects, the metal-nodes in defective materials exhibit a mean coordination number (CN) of 11.6 (UiO-66-0eq), 9.3 (UiO-66-1eq), 8.8 (UiO-66-5eq) and 8.6 (UiO-66-10eq) compared to 12 in the ideal, defect-free UiO-66 structure.

Table 4.1: proposed sum formula, percentage of defects and missing linker per cluster for all full activated UiO-66 samples.

Sample name	Sum formula	% Defects	Missing linker per cluster
UiO-66-0eq	$Zr_6O_{6.2}(BDC)_{5.8}$	3.3	0.2
UiO-66-1eq	$Zr_6O_{7.35}(BDC)_{4.65}$	22.5	1.35
UiO-66-5eq	$Zr_6O_{7.6}(BDC)_{4.4}$	26.6	1.6
UiO-66-10eq	$Zr_6O_{7.7}(BDC)_{4.3}$	28.3	1.7

We move our attention now into the core of this chapter, HPPXRD on soft materials, which is with low pressures of amorphization challenging, since a typical diamond anvil cell setup is designed for working pressures well above 0.1 GPa. Therefore, we applied a radically different approach, using a HPPXRD setup which allows the application of pressure in small-increments (~2 MPa) in the range of p = ambient – 0.4 GPa (see experimental section 7.1.7 for details).[118] In total, we collected 18 HPPXRD datasets for each sample with pressure increments of 0.025 GPa at an X-ray energy of E = 29.2 keV. Contour plots of the obtained HPPXRD pattern are shown in Figure 4.4, and stacking plots are given in the experimental section (see figure 7.7 - 7.10).

Notably, we do not observe any intensities in the HPPXRD pattern that would indicate the formation of nano-regions of correlated defects. However, the absence of such superlattice reflections not excludes correlations on the sub-nano scale which are not detectable with X-ray diffractions techniques.[107] From the contour plots we already observe qualitatively that UiO-66-0eq and UiO-66-1eq remain crystalline up to a pressure of 0.4 GPa with no visual indication of peak broadening.[119]

In contrast a clear loss of crystallinity appears around 0.3 GPa for UiO-66-5eq and at approximately 0.25 GPa for UiO-66-10eq. In order to quantify the onset of amorphization more quantitatively, we performed Pawley profile fits, see experimental section figure 7.3 – 7.6 for further details.

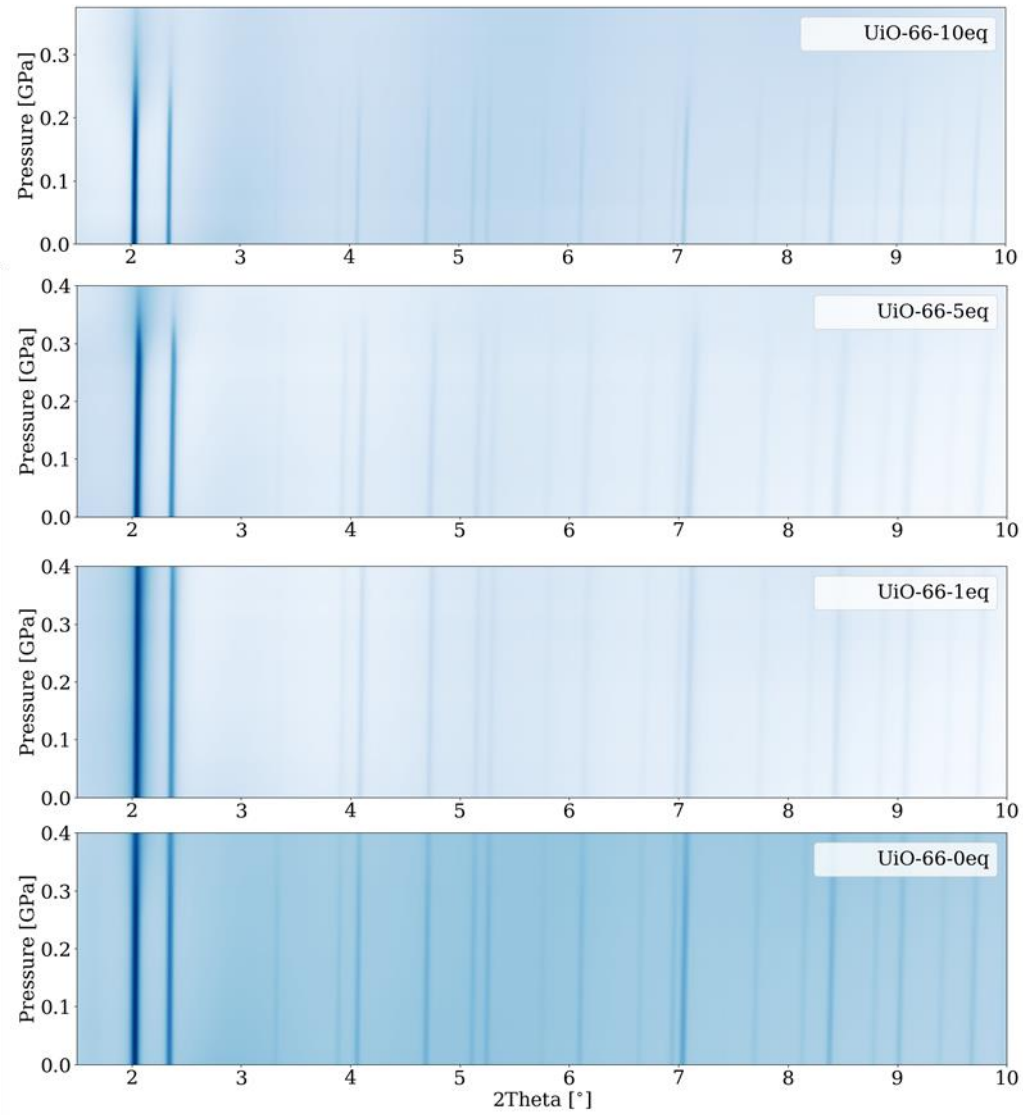

Figure 4.4: Contour plots of HPPXRD data (λ = 0.4246 Å) of UiO-66 from bottom to top without modulator (UiO-66-0eq), with 1 equivalent modulator (UiO-66-1eq), with 5 equivalents modulator (UiO-66-5 eq) and 10 equivalents of modulator (UiO-66-10eq). The High-pressure powder X-ray diffraction data were measured in 0.025 GPa steps starting from 0.1 MPa, leading to 18 datasets between 0.1 MPa and 0.4 GPa. (Dark blue = high intensities, light blue = low intensities).

Analyzing the full width half maximum (FWHM) of the peak shape function as a function of pressure, no significant changes are observed for UiO-66-0eq and UiO-66-1eq until p = 0.4 GPa, see figure 4.5. This confirms that hydrostatic conditions are maintained up to 0.4 GPa without evidence for loss of long-range order of the frameworks. For UiO-66-5eq and UiO-66-10eq, anomalies of the FWHM starting at pressures of p = 0.275 GPa and p = 0.225 GPa are observed. These anomalies are related to an onset of amorphization and agree with the trend found computationally, that an increasing amount of defects leads to reduced mechanical stability. The amorphization process is not reversible, hence is best described

with a collapse of the framework under low hydrostatic pressures (see experimental section figure 7.7 - 7.10 for PXRD pattern after compression).

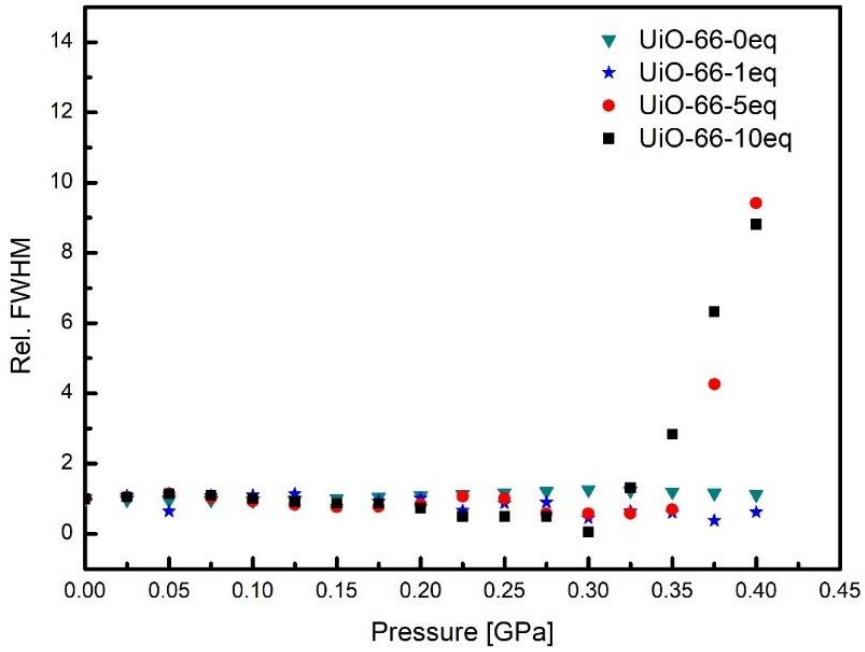

Figure 4.5: Relative FWHM versus Pressure for UiO-66-0eq, UiO-66-1eq, UiO-66-5eq and UiO-66-10eq, shown with green triangular, blue star, red circle and black squares shape symbols, respectively. The anomalous behaviour of the FWHM peak shape function for UiO-66-5eq and UiO-66-10eq allowed us to precisely identify the onset of amorphization which is at 0.275 and 0.225 GPa, respectively.

We now turn our attention to the volume of the materials as function of pressure, V(p), which we obtained from the profile fits. The bulk modulus which is defined as the inverse of the compressibility, i.e. $K = -V \cdot (dp/dV)$, is a measure of volumetric elasticity and returns the mechanic resistance of a material against volumetric changes under hydrostatic pressures. Since we observe unusual volume changes for pressures above approximately 0.2 GPa for the highly defective samples, see Figure 4.6, the bulk moduli were calculated by fitting a 2nd order Birch-Murnaghan equation of state[120] to the first 8 data points in our V(p) data, i.e. up to pressures of p = 0.175 GPa (see figure 4.7).

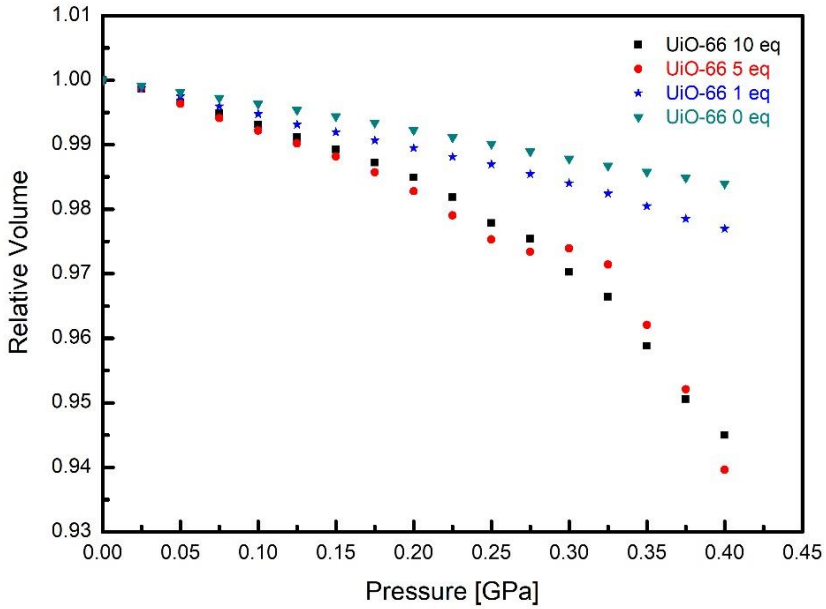

Figure 4.6: V(P) graph of UiO-66-0eq, UiO-66-1eq, UiO-66-5eq and UiO-66-10eq, plotted with green triangular, blue star, red circle and black squares shape symbols, respectively. For UiO-66-5eq and UiO-66-10eq the amorphization onset is at 0.275 and 0.225 GPa, respectively**.**

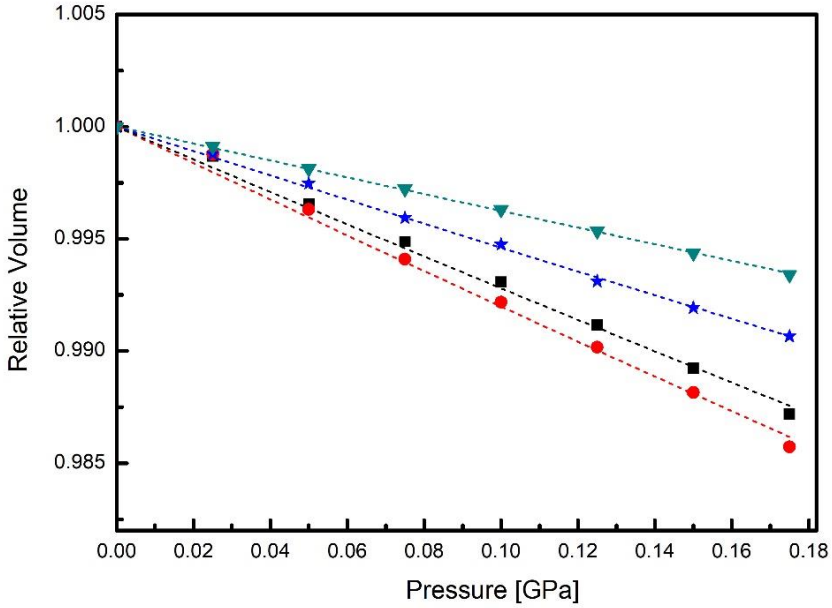

Figure 4.7: The relative volumes as a function of pressure for UiO-66-0eq (dark cyan triangles), UiO-66-1eq (blue stars), UiO-66-5eq (red circles) and UiO-66-10eq (black squares). The straight dashed lines represent the fits of the 2nd order Birch-Murnaghan equation of states for which the first eight data points were used for all data sets.

We obtain values of K(UiO-66-0eq) = 26.4 ± 0.13 GPa, K(UiO-66-1eq) = 18.3 ± 0.16 GPa, K(UiO-66-5eq) = 12.2 ± 0.18 GPa and K(UiO-66-10eq) = 13.9 ± 0.22 GPa , see Table 4.2. The origin of the discontinuous behaviour for pressures above 0.2 GPa for UiO-66-5eq and UiO-66-10eq itself is unclear. The discontinuous change in the V(p) data is only observed for highly defective samples, in principle pointing to the occurrence of a phase transition; however, no other evidence were found in our diffraction data to back-up this finding and is subject of on-going studies.

Table 4.2: Comparison of the bulk moduli of different organic-inorganic coordination polymers. Values marked with ¥ are from computational works. The error calculated for our bulk modulus values was estimated with the program TOPAS V5 (detailed information on the error estimation is given in the experimental section).

Material	Bulk Modulus [GPa]	Reference
UiO-66-0eq	26.4 ± 0.13	This work
UiO-66-1eq	18.3 ± 0.16	This work
UiO-66-5eq	12.2 ± 0.18	This work
UiO-66-10eq	13.9 ± 0.22	This work
UiO-66	17	[121]
UiO-66¥	22¥	[39]
HKUST-1	30.7	[122]
ZIF-8	6.5	[114, 123]
$[CH_3NH_3]PbI_3$	14.9	[124]
$[NH_3NH_2]Pb[HCOO]_3$	19	[125]

Nevertheless, comparing the bulk moduli of our reference sample UiO-66-0eq to literature data (see Table 4.2), we find UiO-66 being one of the least compliant MOFs, only beaten by HKUST-1 with K = 30 GPa. The difference to previous measurements, e.g. by Yot et al.[121] who report UiO-66 to exhibit a bulk modulus of K = 17 GPa highlights the impact of the preparation method on the mechanical response of the framework, e.g. activation and dehydration mechanisms and the potential presence of unintentional defect incorporation. For instance, the use of HCl in the UiO-66 synthetic pathway could led to a decomposition of dimethyformamide (DMF), especially at high temperatures into dimethyammonium and $HCOO^-$. This is indeed a monocarboxylic acid and therefore can introduce, unintentionally, significant amount of defects into the framework as reported in 2016 by Shearer et al..[42] The impact of the coordination of the metal node on the mechanical properties becomes evident

when comparing the bulk modulus of UiO-66-0eq with dense coordination networks such as perovskite-type materials $[CH_3NH_3]PbI_3$ and $[NH_3NH_2]Zn(HCOO)_3$,[125] which exhibit a 6-fold connectivity of the metal-node and a significantly lower bulk moduli despite their higher packing densities. Looking at the bulk moduli of the defective samples, the bulk modulus initially drops significantly. For instance, UiO-66-1eq exhibits a significant lower value (K = 18.3 GPa), confirming computational results and the expectations that a defective framework is less stress resistant. Interestingly, UiO-66-5eq exhibits a slightly lower bulk modulus than the most defective sample UiO-66-10eq. This finding is counterintuitive at first sight, but reflects the complex structure-property relation (see figure 4.8) when going from perfect UiO-66 in fcu topology (CN = 12) to hypothetical UiO-66 in reo topology (CN= 8).

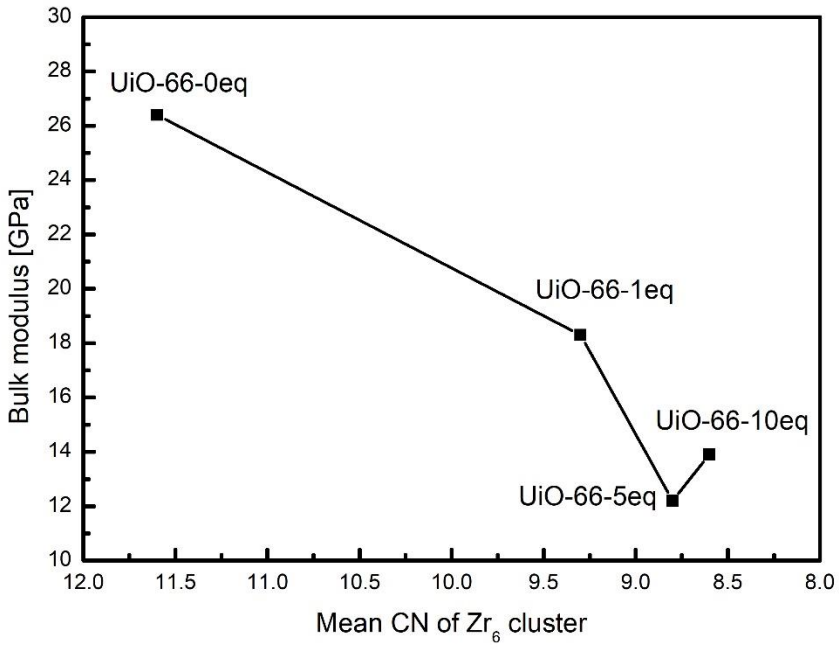

Figure 4.8: Non-linear relationship between Bulk modulus and mean coordination number of the Zr_6 cluster of defective UiO-66 samples. Values close to CN = 12 indicate a perfect sample, while moving to the right, towards CN = 8, indicates an increase of the defectiveness of the samples.

In between, different scenarios with different types and amounts of (correlated) defects are possible, depending on the kinetics and thermodynamics of formation. From our results it seems that with increasing amount of defects correlated regions become more likely, presumably leading to a higher bulk modulus while keeping the amorphization onset low. From zeolites it is known that the correlation between bulk modulus and the loss of

crystallinity is complex, (see experimental section Figure 7.11), with the absence of any obvious correlation. The finding is fascinating, and resembles the currently poor understanding of the thermodynamic and kinetic process of how defects are incorporated into the MOF framework. In turn our results pave the way for experimentally guided computational studies, and emphasize the complex landscape of parameters scientists face when trying to understand and establish structure-property relationships in defective MOFs.

4.3 Conclusions

In this chapter, a series of defective UiO-66 samples have been studied for the first time via high pressure powder X-ray diffraction (HPPXRD). This kind of study on soft materials like MOFs is intrinsically challenging since large volume changes are expected to happen at relatively low pressures and a typical diamond anvil cell setup is designed for working pressures well above 0.1 GPa. To overcome this problem a lab-built set up has been used which allowed us to fine the pressure changes and observe very precisely the onset of amorphization of these materials. In particular, a decrease of the amorphization onset as well as a decrease of the bulk modulus with increasing defect concentration has been found. However, for highly defective UiO-66s samples, the bulk moduli is not correlated with the amount of incorporated defects. An explanation for this unexpected result is that with increasing amount of defects, correlated defective regions become more likely to form on the material. This could lead to high bulk modulus values and low onset of amorphizations. Nevertheless, this fascinating finding highlight the currently lack of understanding of how defects are incorporated into the MOF framework and in turn their impact on the physical properties of MOFs. These results are not only of fundamental interest, but also impacts the potential use of defective-engineered MOFs in adsorption and catalysis.

5 Moving away from UiO-66 system: Evaluation of MOF-808 materials as potential catalyst in a tandem reaction

Abstract

A relative new Zr-based MOF, namely MOF-808, with low node connectivity and enhanced porosity have been used in this work to overcome possible diffusion limitation that might occur when dealing with porous systems with small pore apertures and pores such as UiO-66. Focus was put on synthesis and characterization of pristine MOF-808 and Pt@MOF-808 composite materials with particular emphasis on their thermal stability. Interestingly, variable temperature x-ray diffraction measurement and thermogravimetric analysis allowed us to determine precisely the loss of long range order of the materials above 200°C. Furthermore, Lewis acid test reactions have been performed with these materials which showed an enhanced catalytic activity compared to the defective UiO-66. Preliminary catalytic result also suggest the possible use of Pt@MOF-808 for a tandem reaction that can exploits both Lewis acid sites of the MOF and Pt nanoparticles present in the material.

5.1 Introduction

Defects in terms of missing linkers and missing clusters are often found in Zr-based MOFs, such as UiO-66.[22, 126] The material, even after the removal of many linkers in the framework has been proven to retain its structural integrity whilst improving its catalytic activity.[42, 44] The reason relies on the presence of more accessible coordinatively unsaturated metal sites (CUS) which bear a distinct Lewis acid character. However, UiO-66 even if it has been proven to be a potential catalyst in some industrial relevant catalytic reactions, has an intrinsic limitation, its micro-porosity. In fact, UiO-66 pore openings and pores are as small as 6Å and 12Å respectively.[23] This, indeed can limit the reaction that can be performed with this material since molecules bigger than 6-8Å have difficulties to enter the pores and diffuse into the catalytically active CUS sites. Other Zr-based MOFs with bigger pore apertures and pores that can enhance diffusion are present in the literature. These include diverse systems with different linkers like the 8-connected NU-1000 (with csq topology)[127], the 6-connected MOF-808 (with spn topology) which are much less studied compared to UiO-66 (fcu topology).[31]

MOF-808 is constructed with the same Zr_6 cluster $Zr_6O_4(OH)_4$ which is present in UiO-66 and linked together with six benzene tricarboxylic acid (BTC) molecules (see figure 5.1). The remaining 6 positions on the Zr_6 cluster are occupied by formic acid (FA) which in this case acts as modulator and as a non-constructive ligand.[31] The resulting hydroxylated material has an average sum formula of $Zr_6O_4(OH)_4(BTC)_2(FA)_6$. In principle, the 6-connected MOF-808 can provide more accessible open metal sites because of its lower node-connectivity and its pore system, 1.8 nm in size and 1.4 nm apertures. This and the remarkable surface area results in an enhanced catalytic activity. In fact, these CUS sites can be used for some diverse catalytic applications, ranging from hydrolysis of nerve agent simulants,[128] to Meerwein-Ponndorf-Verley (MPV) reactions,[35] just to name a few.

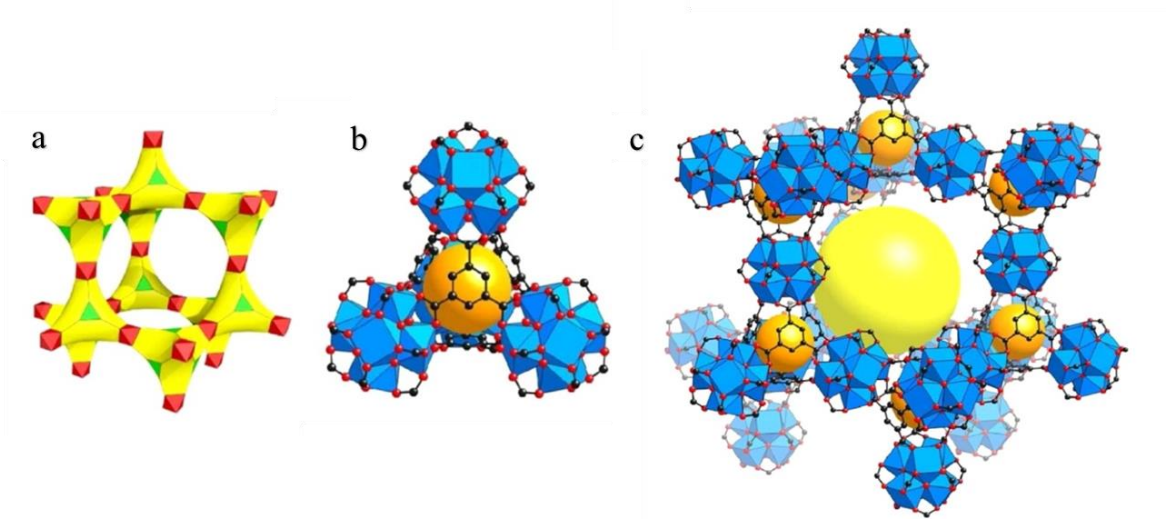

Figure 5.1: a) schematic representation of the spn topology. b) zoom-in of the tetrahedral cage of MOF-808 and c) MOF-808 structure with large adamantine type pores. Reprinted with the permission of ref. [31] Copyright 2014, American Chemical Society.

Having seen the remarkable properties and catalytic activity of this MOF in Lewis acid catalysed reactions it seems only natural trying to introduce metal nanoparticles (NPs) inside MOF-808. There are many ways to introduce guests (metals) inside MOFs, from the most straightforward and industrially applied ways liquid impregnation and chemical vapour infiltration (CVI) to more complicated ones like double solvent approach (DSA).[77, 129] These are post-synthetic techniques which requires the introduction of a metal precursor via liquid or gas phase and the subsequent reduction of the compound to a metallic state. Usually reducing agents such as sodium borohydride, H_2 are used, or the precursor@MOF compound is thermally or photochemically treated. In general, gas phase techniques allow high loadings up to 30-40%which are not achievable with other techniques. This and the simplicity of these methods make them industrially attractive.

However, the lack of control in the size distribution of the metal nanoparticles, the choice of the right volatile precursor that can diffuse inside the pores of the framework (especially for the chemical vapour infiltrations) and the use of reducing agents that might partially destroy the framework should be of concerns.

To overcome this limitations the introduction of pre-formed metal NPs in MOFs through the so-called template synthesis or “bottle around the ship” method was used. This technique consist in introducing pre-formed Pt NPs to the synthetic solution of the MOF (linker and metal salt) prior the formation of the MOF itself. It is apparent that a prerequisite to achieve this goal is that the metal NPs are able to withstand the harsh condition of the MOF synthesis.

For this reason many metal NPs are often synthetized with a capping agent, i.e polyvinylpyrrolidone (PVP) that prevents possible agglomeration even at high temperatures. However, a drawback is also given by embedding the capping agent itself, which might influence the catalytic activity compared to naked NPs. One of the main goal for these systems (metal NPs@MOFs and metal NPs/MOFs), regardless the method of preparation, is to achieve tandem reactions where both MOF with its Lewis acid sites and the introduced metal NPs are active in sequential reactions. Stunning examples are present in the literature, where mainly the MIL family (MIL-101, MIL-53, MIL-125) and UiO-66 MOFs due to their high thermal and chemical stability where the systems of choice.[129] Industrially important tandem reactions (scheme 5.1), such as the citronellal cyclisation to isopulegol with the subsequent hydrogenation to (-) menthol have been catalysed by Pd/MIL-101 (Cr) materials. Nearly complete citronellal conversion was achieved by the Cr^{3+} Lewis acid sites with a diastereoselectivity to rac-isopulegol of 74% after 12 h. After completion of the cyclization step, isopulegol hydrogenation was catalysed by the Pd active sites in 6 h, yielding 70% of the desired (-)-menthol product.[130]

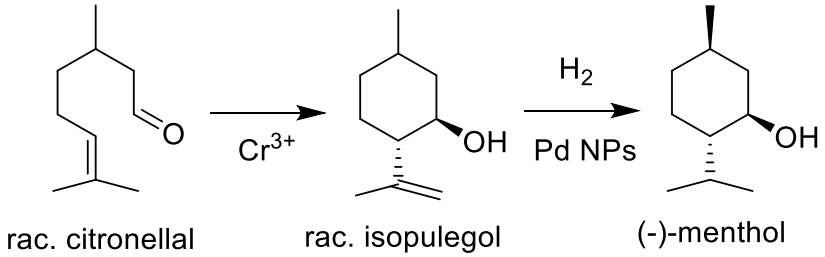

Scheme 5.1: Tandem reaction for citronellal conversion to (-)-menthol catalysed by Pd/MIL-101.

This concept was expanded also to the UiO-66 system, where Pd@UiO-66-NH_2 was utilized in a one-pot tandem oxidation-acetalization reaction with excellent activity and selectivity.[131] In this tandem reaction (scheme 5.2), benzyl alcohol was firstly oxidized to benzaldehyde by the Pd nanocluster, and benzaldehyde acetalization with ethylene glycol occurred at the UiO-66-NH_2 Lewis acid sites to give the 2-pheny-1,3-dioxolane product with 99.9% selectivity.[131]

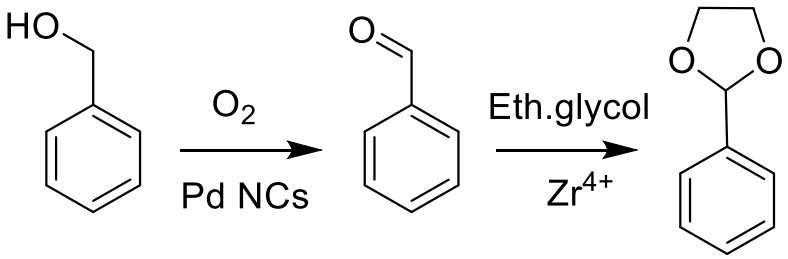

Scheme 5.2: Oxidation of benzyl alcohol over Pd nanoclusters (NCs) and the subsequent acetalization with ethylene glycol over Zr^{4+} Lewis acid sites with the multifunctional catalyst Pd@UiO-66-NH_2.

These are only few example that can give an idea of metal@MOFs potential as multifunctional catalyst.

In this chapter, the same concept was applied to synthetize Pt@MOF-808 material via the bottle around the ship method with the final aim to use this material in a tandem reaction. First, structural characterization of MOF-808 and Pt@MOF-808 composite materials has been performed in order to evaluate this MOF as potential catalyst over important Lewis acid reactions. Furthermore, the Pt@MOF-808 sample was also used for the reduction of cinnamaldehyde to cinnamyl alcohol and a subsequent hydrogenation of cinnamyl alcohol to hydrocinnamyl alcohol reaction which was selected as a proof of concept tandem reaction (see reaction scheme 5.3).

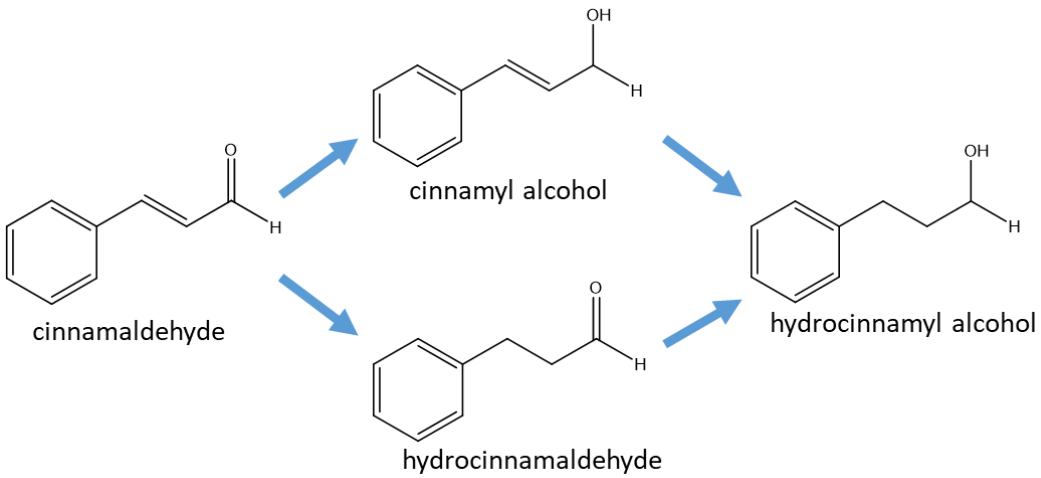

Scheme 5.3: Reaction scheme of the tandem reaction selected for the potential catalyst Pt@MOF-808.

This tandem reaction was chosen because of the industrial importance in the cosmetic industry of hydrocinnamyl alcohol. This alcohol it is a natural fragrance with antimicrobial properties against bacteria and molds. It is used primarily in combination with other antimicrobial drugs as a preservative for cosmetic products. Furthermore, it is also used as fragrance component in fresh flower compositions because of the balsamic odour character.

5.2 Structural characterization of MOF-808 and Pt@MOF-808 composite materials

The general procedures to synthesize pristine MOF-808 and defective MOF-808 are adapted from the literature.[31, 35, 132-133] Pristine MOF-808 was synthesized using $ZrOCl_2.8H_2O$ and BTC with molar ratio 1:1 with different synthesis times; 7 days at 100°C (noted M7) and 3 days at 100°C (noted M3). The defective MOF-808 (noted MD) was synthesized with a metal/linker molar ratio of 3:1 for 2 days at 130°C. Also platinum nanoparticles (Pt NPs) were synthesized according to the literature[134-135] which were afterwards incorporated into the synthesis of MOF-808 to produce Pt@MOF-808 composite materials namely Pt@M7 and Pt@MD. All samples were activated at 100°C under vacuum and were stored in a glovebox with Ar atmosphere prior to the characterization. Initially, PXRD was performed to access the phase purity for all the samples which are reported in figure 5.2 and 5.3.

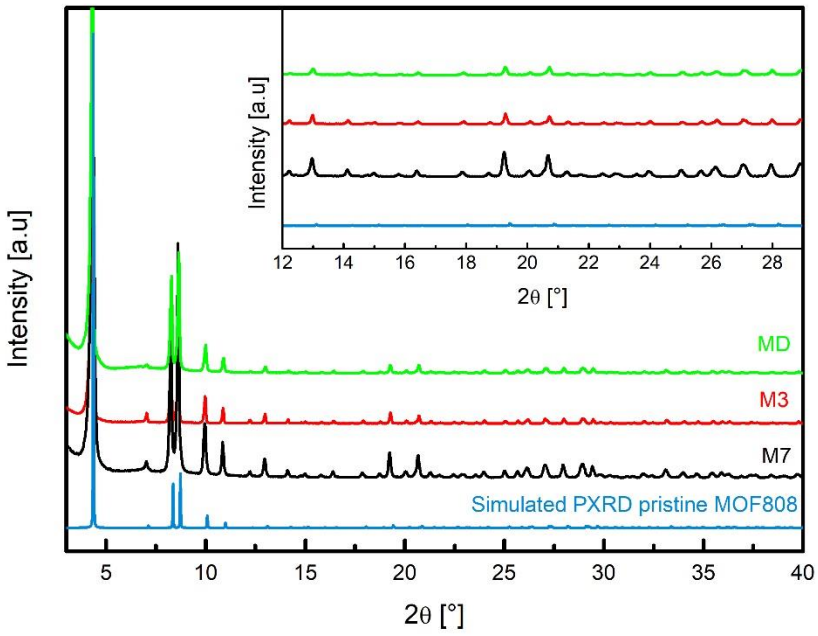

Figure 5.2: PXRD pattern of M7, M3 and MD samples which are shown with black, red and green lines, respectively. The inset show the diffraction patterns in the range 12-30 2θ degree. Simulated PXRD of pristine MOF-808 is also added to confirm the phase purity of all the samples.

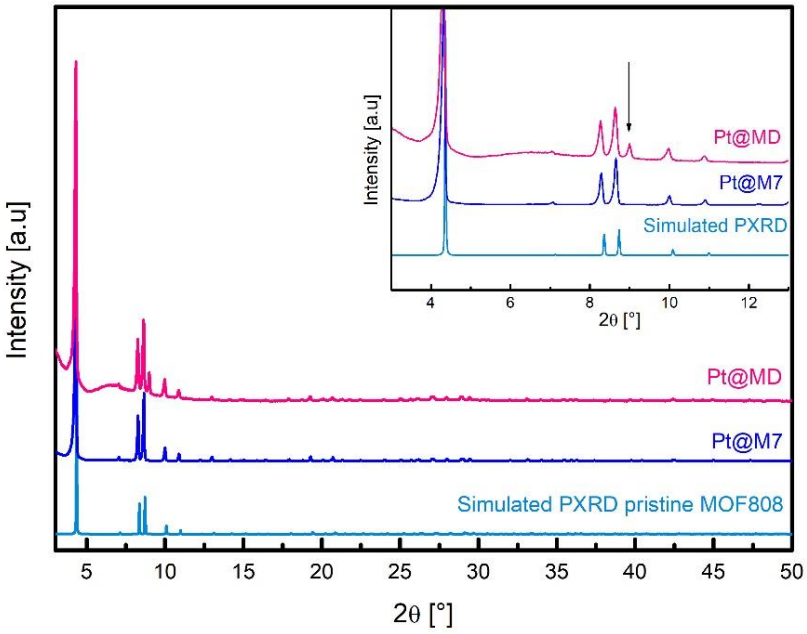

Figure 5.3: PXRD of Pt@MOF-808 composite materials namely Pt@M7 and Pt@MD shown in blue and magenta coloured lines, respectively. The diffractrograms are also compared with simulated PXRD pristine MOF-808 to qualitatively evaluate the phase purity of the samples. The black arrow highlight an additional peak in the sample Pt@MD.

For all the materials, sharp Bragg peaks are observed and nicely fit with the simulated MOF-808 diffraction pattern. It is worth to mention that the Pt@MD pattern shows an additional reflection at low 2θ degree (see inset in figure 5.3 peak highlighted by the black arrow). We can speculate that this could be attributed to remaining solvent molecules which might be still present after the activation of the material. Interestingly, this peak disappear at 130°C and is not present in the diffraction pattern after a second activation with same conditions. Additional peaks due to the presence of Pt NPs are not observed in the diffractograms at high 2θ degree, e.g 39.9 for the Pt (111). This could be explained with the low amount of Pt in the framework (≈ 0.1 wt. %) which was calculated by induced coupled plasma (ICP) and the size of NPs which is around 3.5 nm, too small to give a considerable diffraction signal. Subsequently, N_2 physisorption measurement have been performed (see figure 5.4 and 5.5), in which all the sample display a type I isotherm with no signs of hysteresis loops. BET surface area for the sample M7 are in accordance with data present in the literature.[31] However, for the samples MD and M3 the values are relatively low which could be attributed to the presence of some solvent molecules still present in the framework.[31, 35] Furthermore, for Pt@M7 (see figure 5.5) there only is a minimal decrease in the surface area if compared

to the pristine MOF-808 namely M7 and can be explained with the low Pt content in the framework. On the contrary, the Pt@MD surface area is quite different compared to the pristine MOF-808 and cannot be attributed only to the encapsulation of Pt NPs inside the framework. In fact, the Pt content is very low and equal to 0.04 wt.%. Therefore scanning transmission electron microscopy (STEM) depicted in figure 5.6 and scanning electron microscopy (SEM) shown in figure 5.7 and have been performed to this sample.

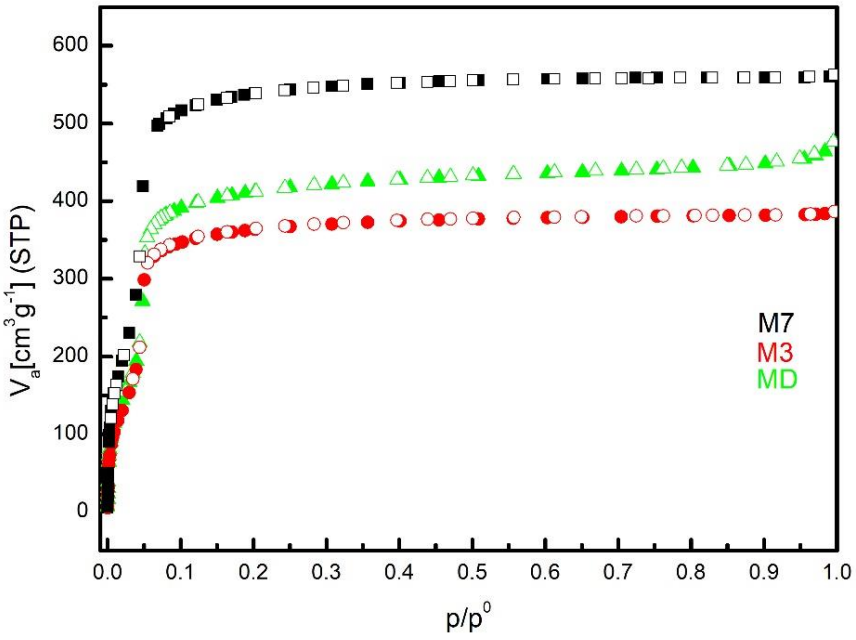

Figure 5.4: N_2 adsorption measurements (77K) of M7, M3 and MD, shown in black squares, red circle and green triangular shape symbols, respectively. Open and filled symbols represent adsorption and desorption branches, respectively.

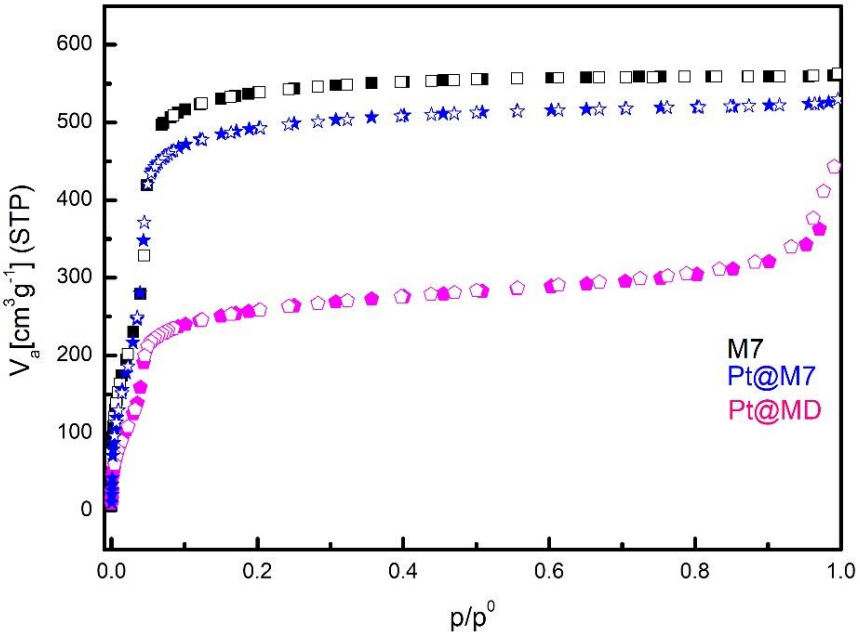

Figure 5.5: N_2 physisorption measurements (77K) of Pt@M7 and Pt@MD in blue star and in magenta pentagons, respectively. Closed and open symbol represent the adsorption and desorption branches, respectively.

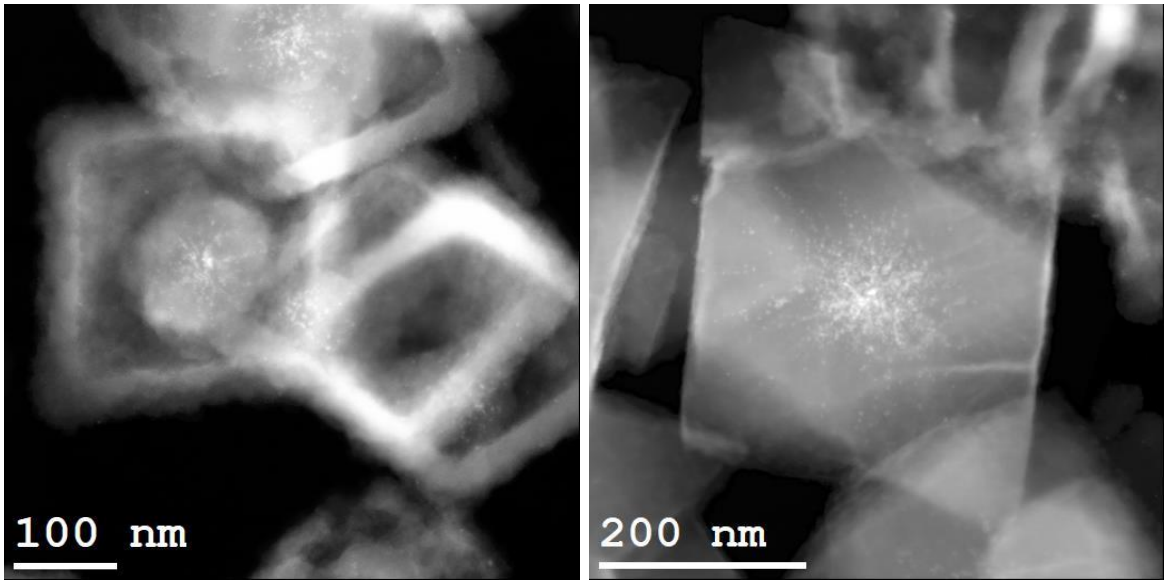

Figure 5.6: STEM images of Pt@MD sample. Left panel are shown "hollow" type crystals" while on the right panel are shown regular "filled" Pt@MD crystals. Pt NPs represented as white spots in the crystals are mainly located in the center of the framework.

As can be seen in figure 5.6 left panel, the majority of crystals show this hollow structure (low magnification picture is shown in the experimental section figure 7.23). It seems from these images that the crystals are somehow excavated resulting in a structure with only the

peripheral layers of the crystals that are still intact. Nevertheless, also regular "filled" crystals with Pt NPs in the center of the framework can be seen as depicted in the right panel of figure 5.6. To better explain the nature of this hollow structure SEM pictures have been performed (see figure 5.7).

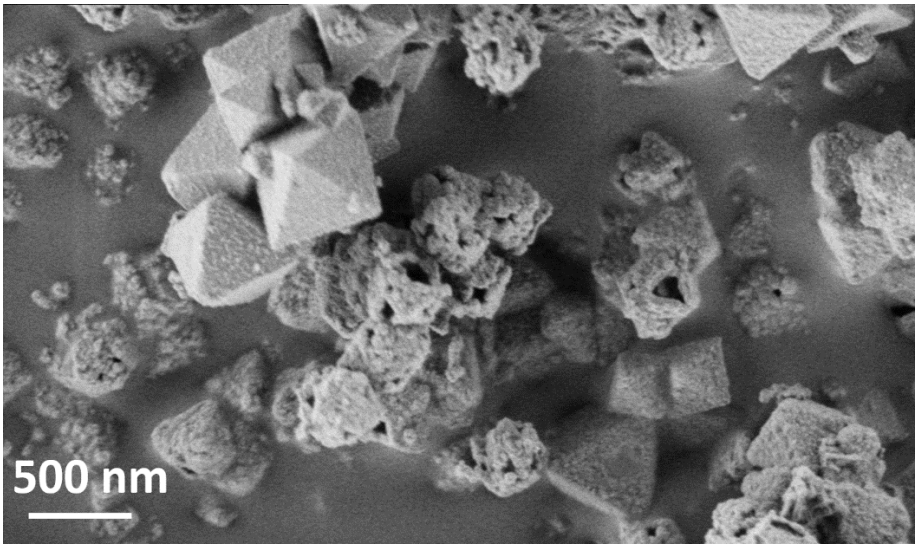

Figure 5.7: SEM picture of Pt@MD where can be seen hollow filled type structures.

The estimated ratio between "hollow" and "filled" crystals are 60/40 in favour of the hollow structure. Furthermore, at the surface of the "filled" crystals can be detected a homogeneous distribution of particles. The nature of this particles is still puzzling and is focus of ongoing studies. Nevertheless, hollow structures and the presence of particles on the outer surface of the filled crystal, which can cause pore blocking, can explain the low surface area of the sample Pt@MD.

It is worth to mention that the origin of this hollow structure is still unknown, even if MOFs crystals with a hollow type structure have been reported in the literature.[136] The preparation method for this kind of structure usually requires the presence of a sacrificial agent that is dissolved during the solvo-thermal synthesis of the second species which is growing on top of the first one. This method was not used during the synthesis of these materials, however we might speculate that the presence of high amounts of PVP (coming from the Pt NPs) in the synthetic solution of the MOF might play a role in the formation of this hollow structure. Inclusion of high amounts of PVP molecules inside the pores can cause errors in during the MOF synthesis and therefore might destabilize the structure resulting in the creation of holes in the crystals.

Furthermore, thermal stability was also determined via the combination of VTXRD and TGA measurements (see figure 5.8 and 5.9). Combination of those methods allows a better understanding of the correlation between molecules removal and structural integrity of the materials. As it can be seen in figure 5.8, below 150°C, no significant mass loss is observed for M7 M3 and MD samples (between 2-5% mass loss). This can be attributed to the removal of water molecules that are adsorbed on the external surface of the MOFs. In the temperature region between 180° - 380°C, further mass loss is observed. Ideally, for the activated MOF-808, this temperature region can be attributed to the removal of coordinated OH and H_2O which may have replaced the formic acid (FA) on the CUS sites after solvent exchange and activation procedure.[35, 128] The last temperature region in the TGA, which is between 400°-600°C, is interesting because it corresponds to the BTC linker decomposition. Analysing this region can give indications concerning the missing linker concentration in each sample. The methodology to estimate the missing linker concentration was adopted from the literature.[42] We found an average coordination number (CN) for M7 and M3 of CN = 5 while for MD the CN = 4.5. All mass losses in every samples are less than the theoretical ones, this suggests that even the pristine materials (M7 and M3) already contain inherent missing linker defects.

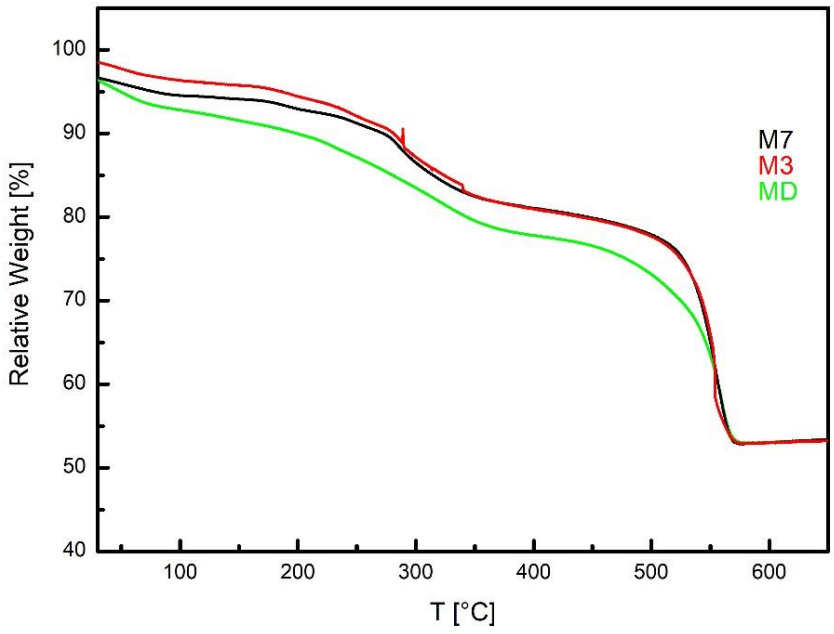

Figure 5.8: TGA of M7, M3 and MD plotted in black, red and green coloured lines, respectively.

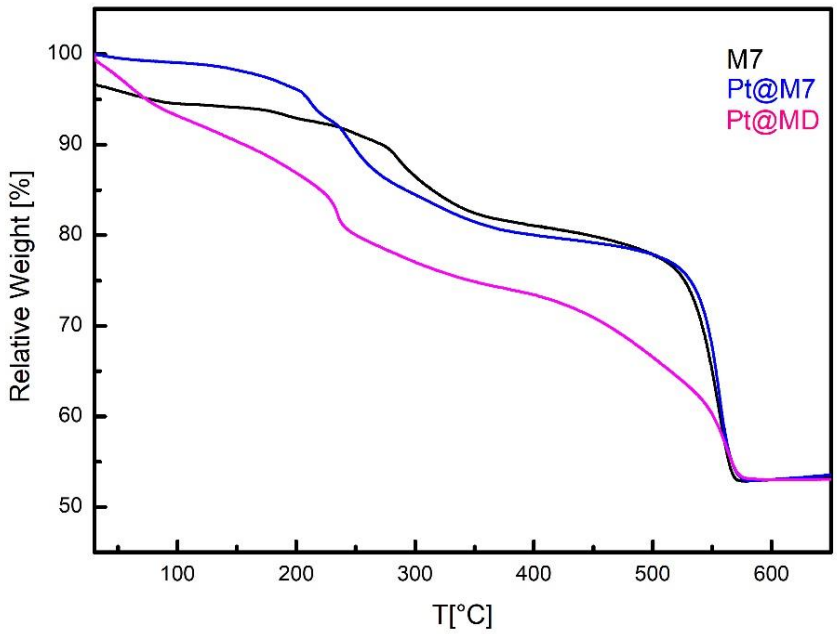

Figure 5.9: TGA of M7 Pt@M7 and Pt@MD samples, shown with a black, blue and magenta coloured lines.

Moving to the TGA of Pt@MOF-808 composite materials, the Pt@MD thermal stability compared to the other samples is different in many aspects. First, in the region below 150°C a 10% mass loss is observed while for the Pt@M7 the mass loss is only marginal around 2% which is similar for the unloaded ones. The difference can be attributed to the presence of holes which are clearly visible on figure 5.7. The presence of this holes can indeed host a large amount of water physisorbed on the external surface of Pt@MD and therefore explain the abnormal mass loss.

In the region 150 – 400°C the mass loss for Pt@M7 and Pt@MD are 19% and 19.7%, respectively. In this case, the mass losses cannot be attributed only to the removal of the coordinated H_2O and OH to the CUS sites but also to the decomposition of the remaining PVP incorporated in the materials with the encapsulation of Pt NPs which can occur between 280 – 350°C which its presence is confirmed by FT-IR spectra (see Figure 5.10).

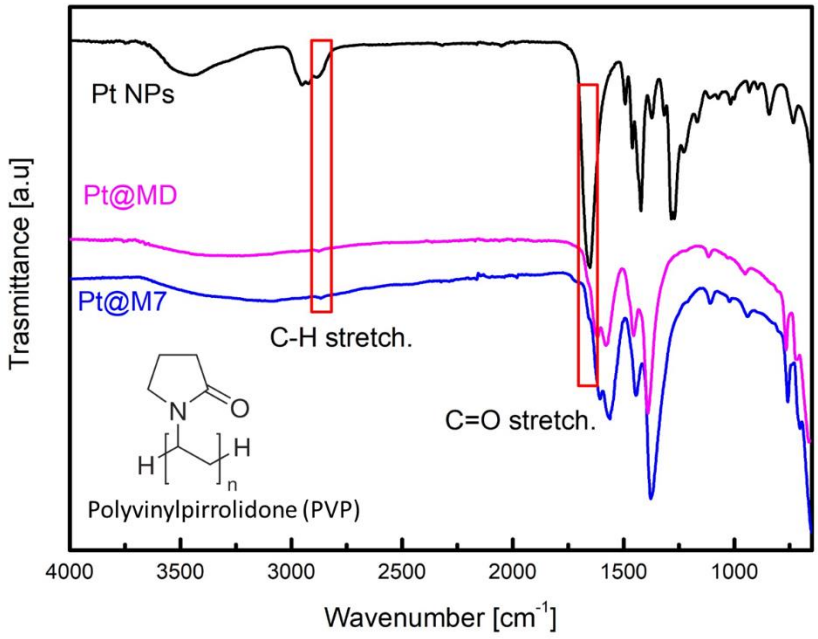

Figure 5.10: FT-IR of the samples Pt@M7, Pt@MD and Pt NPs coated with the capping agent PVP. In the red boxes are highlighted the characteristic peaks of PVP which are also visible in the Pt@M7 and Pt@MD spectra as a small shoulder for the CO stretching at ≈1650cm^{-1} and a small band at ≈2900 cm^{-1} for the CH stretching. The samples were taken out of the glove box and FT-IR was measured under atmospheric conditions, thus the bump at 3500 – 3000 cm^{-1}.

In order to shed some light in this complicated TGA curves, VTXRD of the unloaded MOF-808 and the Pt composite materials have been also performed (see figure 5.11 and 5.12). In both cases crystallinity and long range order are lost above 200°C. This corresponds either to the loss of the non-constructive ligand FA and/or to the loss of H_2O/OH groups adsorbed to the CUS sites. It is clear by the combination of VTXRD and TGA that the removal of this molecules greatly destabilize the structure resulting in a complete loss of the crystallinity at relatively low temperatures.

5.2.1 Negative thermal expansion of MOF-808.

Interestingly, both materials (MOF-808 and Pt@MOF-808), shows a clear shift of the peaks towards higher 2θ (degree) in the VTXRD patterns. This is an indication of a relatively rare phenomenon called negative thermal expansion (NTE), which consist basically in the contraction of the framework upon heating. This behaviour is known to occur in a handful of compounds such as in ScF_3 and ReO_3 perovskites type materials, [137-138] in anhydrous Prussian blue analogues and in ZrW_2O_8.[139-141] The details of NTE mechanisms remain still controversial, however, there is a general consensus that there are essentially two mechanisms active during NTE. The thermal expansion between atom pairs which has a positive contribution, whilst the geometric rotations of rigid units (i.e transverse vibrational modes) has a negative contribution. For NTE to occur then, the geometric effects rigid unit modes (RUMs) must dominate those of the chemical bond expansion (longitudinal modes).[142] MOFs made by metal cluster connected with long and flexible organic linker certainly shares one of the main feature that is believed to favour NTE. It is no surprise that reports of NTE behaviour on MOFs are increasing, [104, 143 144] even so, to the best of our knowledge this peculiar behaviour is not reported for the material MOF-808 so far. Preliminary VTXRD analysis of Pt@MOF-808 and MOF-808 materials (see figure 5.11 and 5.12) confirmed the contraction of the unit cell upon heating. The magnitude of this contraction is quite remarkable, however the present data do not allow us to completely exclude the presence of other processes, i.e solvent removal and partial degradation of the framework, which can deeply influence the NTE behaviour. Nevertheless, an in depth study with the use of Raman spectroscopy or neutron diffraction can shed light on the mechanisms of this peculiar phenomenon. This NTE is important not only for a fundamental viewpoint but can be very useful to minimize and counterbalance the positive thermal expansion of common engineered materials leading for example to a composite material which can be used to build more secure infrastructure, e.g prediction of the material deformation at relative high temperatures.[144].

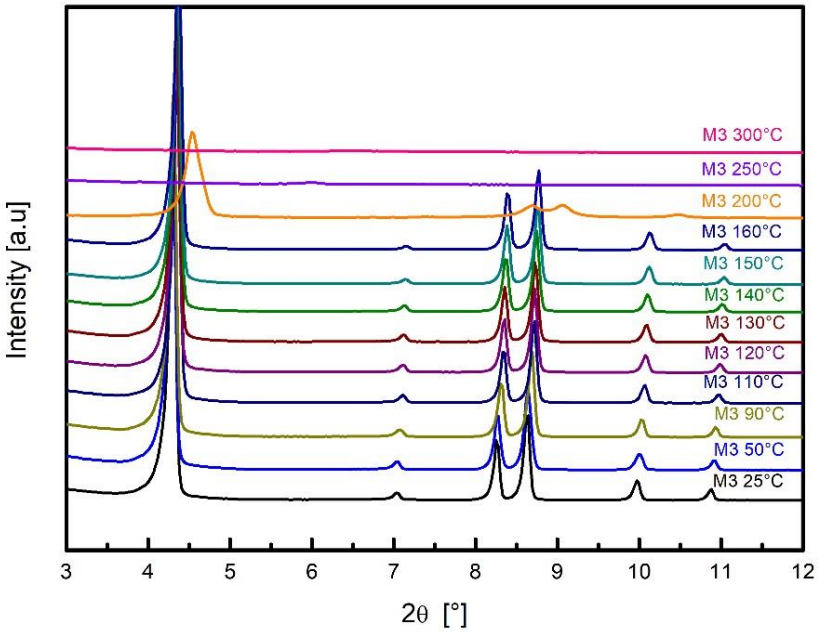

Figure 5.11: Example of VTXRD of the unloaded MOF-808 sample M3. Similar graphs were obtained for the other two unloaded MOF-808 samples which are reported in the experimental section. (see figures 7.12 – 7.16).

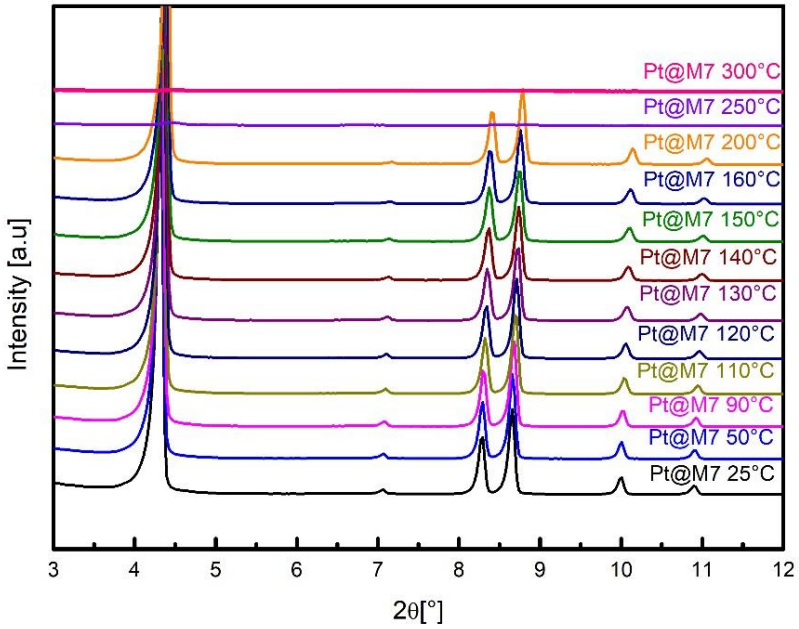

Figure 5.12: Example of VTXRD of Pt@M7 sample. Similar graphs were obtained for Pt@MD which are reported in the experimental section (see figures 7.12 – 7.16).

5.3 Catalytic testing of MOF-808 and Pt@MOF-808 composite materials

As mentioned in the introduction part, one of the main goals of this chapter is to have an idea if MOF-808 and in particular Pt@MOF-808 can be used as heterogeneous catalysts. Different batches of the sample MD and Pt@MD were produced for the catalytic testing using the same synthetic procedure reported in the previous chapter.

The final aim is to use Pt@MOF-808 for a tandem reaction which exploits the Lewis acid sites of the MOF and the encapsulated Pt NPs for a subsequent hydrogenation reaction.

The idea is to first perform the reduction of the aldehyde to the alcohol and then perform the hydrogenation of the double bond via Pt NPs located primarily at the centre of the MOF-808 framework.

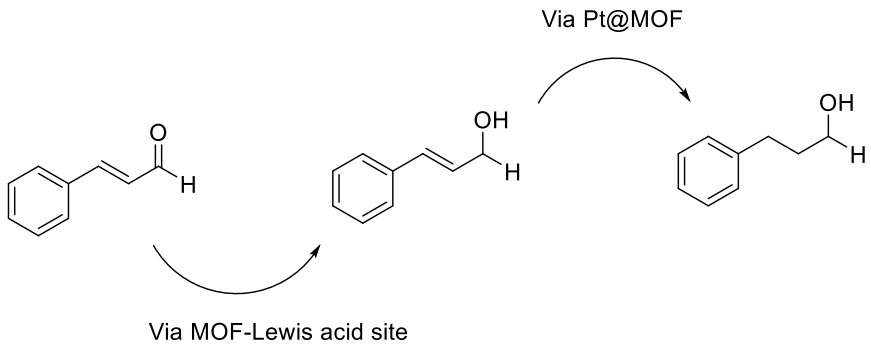

Scheme 5.4: Proposed reaction scheme of a tandem reaction catalysed by Pt@MOF-808 composite materials.

5.3.1 Testing MOF-808 for MPV reaction

Before performing this targeted reaction is important to evaluate if unloaded MOF-808 is capable to perform Lewis acid based reaction. The selected first test reaction is the MPV reduction of cyclohexanone to cyclohexanol. The resulting molecule is of paramount importance since it is used in the order of billions of kilograms as precursor for Nylon® production. The actual industrial process oxidise cyclohexane with a Co catalyst to produce a mixture of cyclohexanone and cyclohexanol. It is therefore important to have a catalyst that selectively transforms cyclohexanone to the more valuable cyclohexanol.[14] As can be seen from figure 5.13 full conversion after 24 h with no by-product was achieved. Interestingly, the system converted almost quantitatively cyclohexanone within 6 h. Furthermore, a brief induction period with low conversion in the first 30 min of reaction can be seen. This can be ascribed to the reagents that need some time to diffuse inside the pores

of the catalyst and reach the active CUS sites. The heterogeneity of the system was confirmed by the hot filtration test while the necessity of catalyst was confirmed by the blind test.

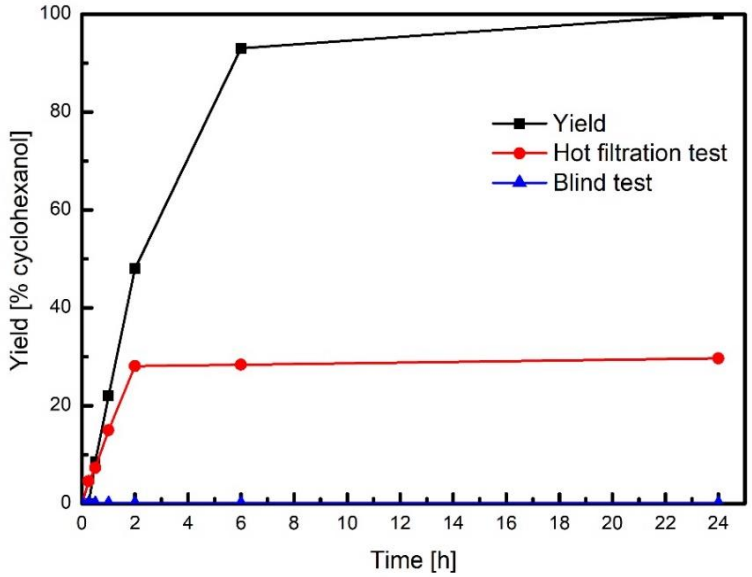

Figure 5.13: Yield versus time plot for the reduction of cyclohexanone to cyclohexanol with MOF-808 as catalyst. Yield curve, hot filtration test and blind test depicted in black red and blue coloured line, respectively. The catalytic reactions were followed by gas chromatography. Conditions used are 80°C in air with isopropanol in excess that act as solvent and reagent.

5.3.2 First steps towards the tandem reaction

After this first promising results, the targeted MPV reduction of cynnamaldehyde to cinnamyl alcohol was performed. This reaction has already been studied by Plessers et. al.,[35] however, to the best of our knowledge this tandem reaction with Pt@MOF808 as catalysts has not been reported so far. Nevertheless, as it can be seen in figure 5.14, almost full conversion of the substrate with negligible amount of by-product was achieved in 6 hours which is comparable to the data present in the literature.[35] The enhanced catalytic activity of the system is shown in figure 5.15 where after 6 h almost full conversion for MOF-808 and Pt@MOF-808 was reached. Only a small difference of 4% in the activity can be detected. This represent a promising result since the encapsulation of Pt NPs do not limit the availability of Lewis acid sites in the catalyst. Interestingly, Figure 5.15 also displays the beneficial effect of the bigger pore openings and pore size of MOF-808 that allow bigger molecules to react and enhance diffusion of the reagents. This effect is highlighted in the

low conversion rates achieved by defective UiO-66 and perfect UiO-66 where only 55% and 2% of the cyannamaldehyde were converted, respectively. UiO-66 low conversion can be also explained if we consider the MPV mechanism that is generally accepted in the scientific community.[14] This mechanism assumes the simultaneous adsorption of the alcohol and the ketone on the active site and the direct hydrogen transfer from the alcohol to the ketone, involving a six-membered cyclic transition state, see scheme 5.5. Therefore, it seems reasonable to hypothesize that the more sterically hindered Zr Lewis acid sites of UiO-66 will form such a transition state with more difficulties, which ultimately end in a low conversion rate.

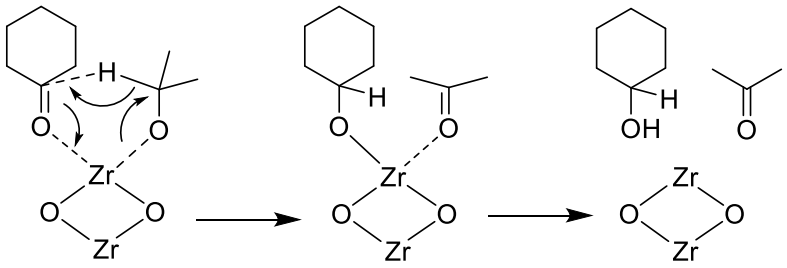

Scheme 5.5: Proposed reaction scheme for the MPV reaction of cyclohexanone to cyclohexanol. The same reaction mechanism is assumed for the reduction of cynnamaldehyde to cinnamyl alcohol.

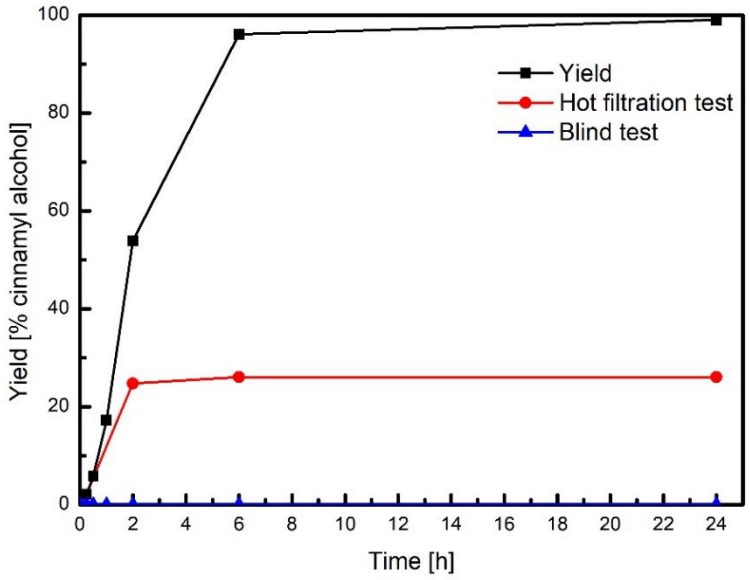

Figure 5.14: Yield versus time plot for the reduction of cynnamaldehyde to cinnamyl alcohol using MOF-808 as catalyst. Yield curve, hot filtration test and blind test depicted in black red and blue coloured line, respectively. The catalytic reactions were followed by gas chromatography. Conditions used are 80°C in air with isopropanol in excess that act as solvent and reagent.

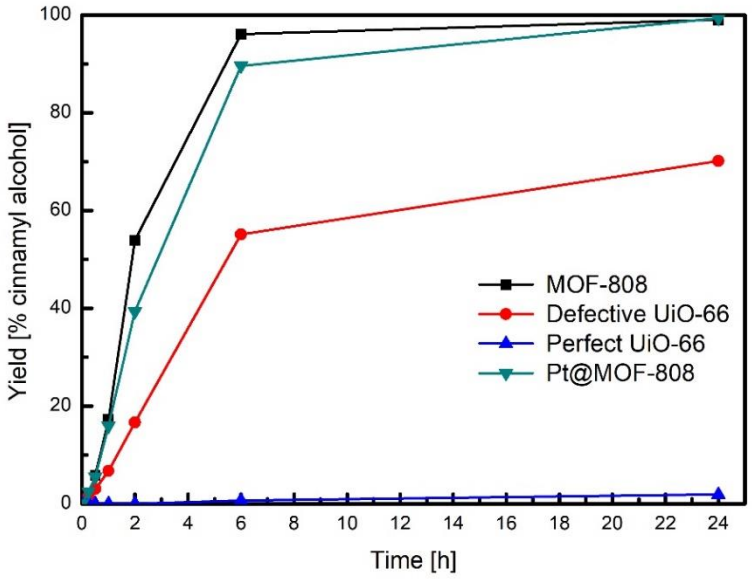

Figure 5.15: Comparison of different catalyst over the reduction of cynnamaldehyde to cinnamyl alcohol. MOF-808, defective UiO-66, perfect UiO-66 and Pt@MOF-808 yield curves are depicted in black, red, blue and dark cyan coloured lines, respectively. The catalytic reactions were followed by gas chromatography. Conditions used are 80°C in air with isopropanol in excess that act as solvent and reagent.

5.3.2.1 First attempt of performing a tandem reaction with Pt@MOF-808

A first attempt to perform the tandem reaction under mild conditions (80°C, 2 bar of H_2 isopropanol in excess and under stirring) was performed, in which, only two aliquots were taken, the first one after 4 h and the other one after 20 h. Interestingly, after 20 h with a selectivity of 95% and full conversion towards hydrocinnamyl alcohol was achieved. To the best of our knowledge this tandem reaction with Pt@MOFs as catalysts has not been reported, yet.

Unfortunately, in the timeframe of this PhD thesis it was not possible to reproduce and complete these catalytic studies. Problems in the reproduction of the catalyst slowed down considerably any possibility to complete the catalytic testing of this material before the end of the project. Nevertheless, these preliminary data are promising results which are worth to investigate in the future.

5.4 Conclusions

In this chapter, the thermal stability of unloaded MOF-808 and Pt@MOF-808 composite materials have been investigated via the use of TGA and VTXRD. Interestingly, when heated, the materials show a clear shift of the main peaks towards higher 2θ angles suggesting a contraction of the unit cell. This negative thermal expansion is relatively rare phenomenon and preliminary results suggest a remarkable NTE character of MOF-808 materials.

Furthermore, several reaction to test the Lewis acidity of the unloaded MOF-808 were performed. The good catalytic performance in the MPV reductions of cyclohexanone to cyclohexanol and cynnamaldehyde to cinnamyl alcohol even when Pt NPs were encapsulated inside the framework suggest MOF-808 as a good candidate for the selected tandem reaction. Interestingly, the preliminary data suggest that 95% selectivity with almost full conversion after 20 h can be achieved. However, in the timeframe of this project more focus was put on the synthesis of the material rather than an in depth catalytic study of the aforementioned reactions. Many other important experiments still need to be performed, e.g recyclability and hot filtration tests, however, these preliminary results are first indications of a possible use of Pt@MOF composite materials for tandem reactions.

6 Summary and outlook

The targeted incorporation of defects in engineered materials is at the hearth of material science. In particular in MOFs, defects seem to play a key role in synthetic methods and can become an important additional tool for designing MOFs with enhanced reactive properties. However, establishing a clear structure-property relationship remains a problem still today. In this work, the incorporation of defects via the modulation approach into different Zr-based MOFs was studied. The system investigated were then characterized by water adsorption, high pressure PXRD (HPPXRD) and variable temperature XRD (VTXRD) in order to uncover the effect of defects in material properties.

An important goal that was achieved during the time frame of this thesis, was the use of the modulation approach to increase systematically the missing linker defects of UiO-66 samples. The obtained samples were then studied with the use of water adsorption measurements which allowed to quantify the hydrophilicity of UiO-66. Furthermore, it was possible to link the hydrophilicity, which is reflected by the Henry constant, to the catalytic activity of the material. A test reaction, which exploited the Lewis acid sites generated by missing linker defects, was used for this purpose. Interestingly, an increasing amount of modulator had a beneficial effect on the catalytic activity, possibly due to the creation of more CUS sites and a more open structure that decreased considerably any diffusion limitations.

The behaviour of MOFs under mechanical stress is another property that is crucial for future industrial application of these materials, e.g in catalyst shaping processes. For this reason, defective UiO-66 was investigated for the first time via HPPXRD. It is worth to mention that this kind of study on soft materials like MOFs is intrinsically challenging since large volume changes are expected to happen at relatively low pressures (< 0.1GPa). To overcome this problem a lab-built set up has been used which allowed to fine tune the pressure changes and observe very precisely the onset of amorphization of these materials. In particular, a decrease of the amorphization onset as well as a decrease of the bulk modulus with increasing defect concentrations has been found. The values found, range between 26.4 and 12.2 GPa, which are one of the highest values reported for MOFs. However, for highly defective UiO-66s samples, the bulk moduli does not correlate with the amount of incorporated defects in a simple linear relationship. An explanation for this unexpected

result is that with increasing amount of defects, correlated defective nano-regions become more likely to form on the material which could lead to higher bulk modulus values and therefore a more stable structure.

Even if catalytic and mechanical properties are very promising for future industrial application, UiO-66 pore openings and pores are as small as 6Å and 12Å, respectively. This is a drawback that indeed can limit the reaction that can be catalysed by this material. For this reason an attempt to transfer the knowledge acquired with the UiO-66 system was also made during the time of this thesis where the modulation approach was used to introduce defects into another MOF called MOF-808. This material shares the same Zr_6 cluster of UiO-66 but instead of being connected by 12 linker molecules is connected only by 6 resulting in a more open framework. In principle, the 6-connected MOF-808 can provide more accessible open metal sites, especially if defects are engineered into the framework. Furthermore, MOF-808 pore system, 1.8 nm in size and 1.4 nm apertures, gives the material a remarkable surface area that helps to limit diffusion limitations of molecules towards the active open metal sites, which is reflected in an enhanced catalytic activity. This, however, come with a cost. The material is less chemically and thermally stable compared to UiO-66. For this reason, in order to evaluate more precisely its thermomechanical behaviour, VTXRD have been performed for the first time in pristine MOF-808. The stability of the framework is lost at relative low temperatures (200°C) if compared to the stability of UiO-66 that can reach 400°C.

Lastly, Pt NPs were successfully encapsulated inside MOF-808 via a “bottle around the ship” approach. Thermal stability of the composite material was confirmed via VTXRD, which is in the same range of the unloaded MOF-808, meaning that the presence Pt NPs do not affect negatively the framework. The location of metal NPs were confirmed via TEM and STEM which are located primarily in the centre of the framework; but a minority of them are also present on the surface, resulting in a wide spread distribution of Pt NPs in MOF-808 crystals. The amount of Pt (wt. %) that can be incorporated in this material can range between 0.1 to 0.04%, which was determined with ICP and elemental analysis in different samples. Pt@MOF-808 materials were synthetized with the final aim of using this composite material in a tandem reaction (cynnamaldehyde to hydrocinnamyl alcohol). Several Lewis acid test reactions were performed with unloaded MOF-808 in order to probe the catalytic activity of the framework itself with almost complete conversions within 6h. It is worth to mention that the enhanced porosity of MOF-808 had a beneficial effect which is

reflected in the difference of activity in the reduction of cinnamon aldehyde to cinnamyl alcohol after 6h, when MOF-808 almost reached full conversion, defective UiO-66 reached only 55%. Subsequently, a first attempt of one-pot reaction was preformed, resulting in almost full conversion of cynnamaldehyde to hydrocinnamyl alcohol with 95% of selectivity; however, during the timeframe of this PhD, it was not possible to complete and optimize these catalytic studies due to unexpected problems in the reproducibility of the catalyst.

At this point, it is possible to answer some of the question raised at the beginning of the thesis. A certain degree of control over defect incorporation in the UiO-66 system was achieved by the modulation approach; however, the selective introduction of defects, i.e missing linker and missing cluster, is still a challenge. Furthermore, defect engineering in MOFs is still largely limited to a handful of MOFs which includes H-KUST-1, MOF-808, PCN-222 and NU-1000. In order to have a complete understanding of how defects incorporate in MOFs and their impact, these studies needs to be expanded to other system; only then we will see if fundamental structure–property relations across different systems will be discovered or if it will be necessary to look at every system independently. It is also important to keep in mind that the introduction of defects on these porous materials is not limitless and a balance between reactivity and stability needs to be found. It is now apparent that defective MOFs bear many opportunities that contain fascinating promises for the area of materials science. In particular UiO-66, due to its catalytic activity and mechanical stability, even after defect engineering is one of the most studied MOFs and might be the framework which is closest to an industrial application.

7 Experimental section

7.1 General techniques and methods

All chemicals were purchased from commercial suppliers (Sigma-Aldrich, Alfa Aesar, Acros Organics and others) and used without further purification. Air sensitive chemicals and synthetized materials were manipulated under inert gas conditions using Schlenk-line and glovebox techniques (O_2 < 0.5 ppm and H_2O < 0.5 ppm). Argon in the Schlenk line was not further purified. Drying of metal-organic frameworks was performed in dynamic vacuum (p = 10^{-3} mbar) while activation was performed at proper temperatures ranging from RT to 320°C. Once the materials were activated they were stored into a glovebox with inert atmosphere.

7.1.1 Fourier transform infrared spectroscopy (FTIR)

FTIR spectra were measured with a Bruker Alpha FTIR spectrometer equipped with a single-reflection platinum ATR (spectral region 4000 cm^{-1} – 400 cm^{-1}) module under inert gas conditions inside a glovebox. All spectra were processed with the software provided by Bruker.

7.1.2 Powder x-ray diffraction (PXRD)

Powder X-ray diffraction (PXRD) measurements were recorded in flat mode with an X'Pert Empyrean series 2 PANalytical equipment in Bragg–Brentano geometry, with a PIXcel position sensitive detector and a CuKα radiation source (λ = 1.54178 Å voltage and intensity were 45 kV and 40 mA, respectively) at room temperature. K_β radiation were removed with a Ni-filter.. The measurement range was from 5.0° to 50.0° (2θ) with a step size of 0.040° (2θ) and an acquisition time of 35 seconds per step.

Air sensitive samples were recorded in capillary mode with the same instrument. The capillary were prepared under inert gas condition inside a glovebox and sealed with grease after preparation.

7.1.3 N_2 physisorption measurements

N_2 adsorption-desorption isotherms were measured using a Quantachrome autosorb iQ2 ASiQwin apparatus equipped with a micropore port ($1 \cdot 10^{-5}$ bar). Void volume was measured with helium. Measurements were conducted at 77 K with N_2 as adsorbant gas. Before starting the measurement, the samples (~50 mg) were pre-heated for 12 h under 150 °C.

7.1.4 Thermogravimetric analysis (TGA)

Thermogravimetric analysis was performed with a Mettler Toledo TGA/STA 409 PC apparatus with a continuous heating ramp of 5 or 10 °C/min applied under synthetic air flow. Around 5 mg of sample were used in a temperature range from 30 to 800°C.

Qualitative analysis of TGA data obtained on UiO-66 samples allowed us to determine the defectiveness of the samples using the method proposed by Lillerud and co-workers in 2011 and explained step by step by Shearer et al. in 2016.[42] The procedure is reported here and this was made with an important assumption: that the residue in each TGA experiment is pure ZrO_2. In order to do so, the TGA measurements were run up to 800 °C under a flow of synthetic air, and with a relatively slow temperature ramp (5 °C/min). Such conditions should ensure the complete combustion of organics and the conversion of zirconium to ZrO_2.

To have a better idea of what happens is good to have in mind the reaction for the complete combustion of the ideal, de-hydroxylated UiO-66, Zr_6O_6 $(BDC)_6$:

$$Zr_6O_6\ (BDC)_6 + 45\ O_2 \rightarrow 6ZrO_2 + 48CO_2 + 12H_2O$$

The molar mass of Zr_6O_6 $(BDC)_6$ is 1628.03 g mol^{-1} , a factor of 2.20 higher than the solid residue - 6 moles of ZrO_2 (6 * 123.22 = 739.34 g mol^{-1}). Thus, if the end weight at 800 °C of a TGA run on UiO-66 is normalized to 100 %, then the TGA plateau (representing the empty, solvent free, and de-hydroxylated MOF) should ideally be found at 220 % on the TGA trace. However, this never happen since it typically falls significantly short of this theoretical weight, meaning that the UiO-66 framework is lighter than that formulated in the idealized equation. This observation was the starting point of the hypothesis that the UiO-66 framework can be linker deficient.[42] It is worth to mention that both missing linker and

missing cluster defects introduce linker deficiencies to the UiO-66 framework, meaning that TGA cannot distinguish between the 2 types of defect. [42]

In general, the theoretical TGA plateau weight (**Wtheo.Plat**) of any Zr_6 MOF composition can be calculated with the following equation:

$$Wtheo.Plat = \left(\frac{Mcomp}{M6ZrO_2}\right) * Wend$$

Where:

Mcomp = is the molar mass of the composition of interest.

$M6ZrO_2$ = is the molar mass of 6 moles of zirconium oxide (739.34 g mol^{-1}).

Wend = is the end weight of the TGA run normalized to 100%

Now we are essentially considering the material in a state where only the zirconium oxide connectors and BDC linkers remain. We thus assume that each missing linker is charge compensated by an extra oxide anion on the cluster, giving the material the following average composition:

$$Zr_6O_{6+x}(BDC)_{6-x}$$

Where x is the number of linker deficiencies per Zr6 formula unit.

The weight contribution per BDC linker (**Wt.PLTheo**) can be arrived at by simply taking the difference between the TGA plateau of the ideal dehydroxylated material (**WIdeal.Plat**) and the end weight of the TGA run (**Wend**), and dividing by **NLideal**., the number of linkers in the ideal Zr_6 formula unit:

$$Wt.PLtheo = \frac{(Wideal.Plat - Wend)}{NLideal}$$

The actual (experimental) number of linkers per defective Zr_6 formula unit, NLExp (i.e. 6-x) in $Zr_6O_{6+x}(BDC)_{6-x}$, can now be determined by rearranging the previous equation and replacing the idealized **NLIdeal** and **WIdeal.Plat** values with the real experimental values, **NLExp** and **WExp.Plat**:

$$NLExp = (6 - x) = \frac{(WExp.Plat - Wend)}{Wt.PLtheo}$$

Which rearranged is:

$$x = (6 - NLexp) = 6 - \left(\frac{WExp.Plat - Wend}{Wt.PLtheo}\right)$$

Wt.PLtheo is known when the end weight (**Wend**) of the TGA run is normalized. Thus, the experimental TGA plateau (**WExp.Plat**) is the only unknown value in the equation. The correct choice of plateau is therefore the most crucial part of the analysis. The chosen plateau must represent the material in a state where its composition is $Zr_6O_{6+x}(BDC)_{6-x}$.[42] Meaning without any residual molecules coming from residual solvent, -OH groups in the Zr_6 cluster and modulator molecules.

The best way to explain this is through an example:

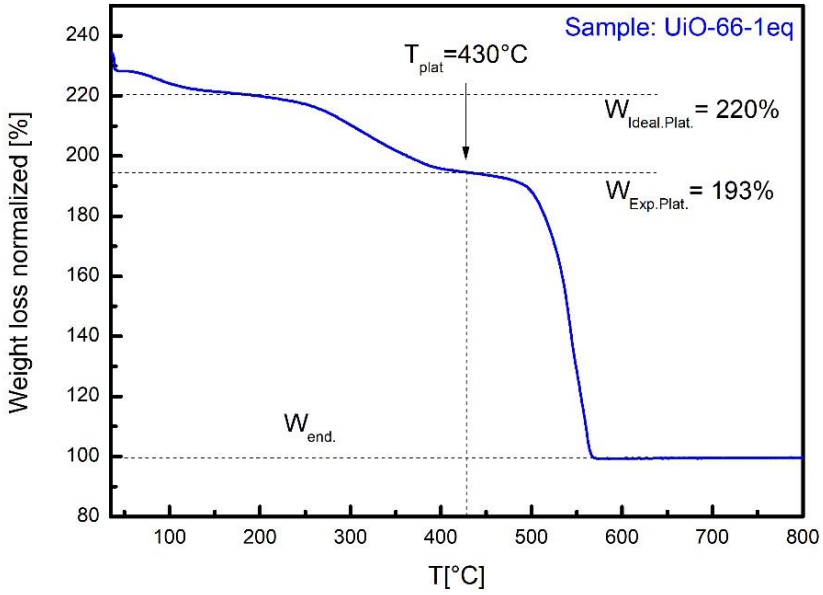

Figure 7.1: TGA curve of the UiO-66-1eq sample. The data were normalized to the weight at the end of the TGA curve. The dashed lines represent the points where the data where taken for the calculation.

Simply by observing the figure, it is qualitatively obvious that this sample is linker deficient – it is significantly lighter than the ideal de-hydroxylated material. In the example, **Wend** has been normalized to 100 %, and thus **Wt.PLtheo** is automatically known to be 20 %. Thus, only the (experimental) weight of the TGA plateau (**$W_{Exp.Plat}$**) is needed to calculate

the number of linker deficiencies per Zr_6 formula unit x. In order to obtain an accurate $\mathbf{W_{Exp.Plat}}$ value, it is of utmost importance to pinpoint the temperature at which the experimental plateau is reached.

This is when the removal of solvent molecules (25-100 °C), de-hydroxylation (ca. 200-325 °C), and removal of the modulator (> 320°C) has already occurred prior to this temperature. Thus, at $\mathbf{T_{plat}}$ = 430 °C (emphasized by the vertical dashed line in the figure), the material is in the desired state (with no other additional molecule besides the linker). At this point, the experimental plateau weight ($\mathbf{W_{Exp.Plat}}$) can be easily determined – it is simply the (normalized) weight of the material at $\mathbf{T_{Plat}}$ (= 430 °C), which is 193 % (as emphasized by a horizontal dashed line in the figure). This is considerably lower than the plateau theoretically expected for an ideal UiO-66 sample ($\mathbf{W_{Ideal.Plat}}$= 220 %), also emphasized by a horizontal dashed line in the figure), indicating that the material is significantly linker deficient:

With $\mathbf{W_{Exp.Plat}}$ known, we can now calculate **NLExp**, the average number of BDC linkers per $Zr_6O_{6+x}(BDC)_{6-x}$:

$$NLExp = (6 - x) = \frac{(WExp.plat - Wend)}{Wt.PLtheo}$$

$$NLExp = (6 - x) = \frac{(193\% - 100\%)}{20\%} = 4.65$$

Thus x:

$$x = (6 - NLExp) = 6 - \left(\frac{WExp.plat - Wend}{Wt.PLtheo}\right) = 1.35$$

Putting this x value into the defective molecular formula $Zr_6O_{6+x}(BDC)_{6-x}$ provides us with the composition of the material at T_{Plat} = 430 °C in the TGA curve: $Zr_6O_{7.35}(BDC)_{4.65}$. These calculation were made also for the other samples in the thesis, i.e UiO-66-0eq, UiO-66-5eq UiO-66-10eq and for MOF-808 samples M7 M3 and MD.

7.1.5 Transmission electron microscopy (TEM)

Transmission electron microscopic measurement were carried out with a JEOL JEM 2010 with LaB_6-Cathod with an acceleration voltage of 120 kV at the department of Chemistry in the chair of Prof. Dr. Sevil Weinkauf, TUM. Furthermore, scanning transmission electron microscopy STEM were performed in different institutes. Primarily by Dr. Aladin Ulrich, in the chair of Experimental Physics II at Augsburg University used a JEOL 2100F type instrument with an acceleration voltage of 200 kV. TEM and STEM were helpful in determine the size distribution of Pt NPs encapsulated inside MOF-808 materials. The size distribution was calculated over 100 particles and the particles were measured with the software ImageJ.

7.1.6 Water adsorption measurement

Water isotherms were measured by Rifan Hardian on a BEL Japan BELSORP instrument at Aix-Marseille University in Marseille, France. In the context of the European project DEFNET.

Prior to the measurements, samples were activated to 170°C under secondary vacuum for 16 hours. Prior to performing water adsorption, water (analyte) was flash frozen with liquid nitrogen and then evacuated under dynamic vacuum 3 times in order to remove dissolved gases from the water reservoir. The measurement temperature was controlled with a water bath at 25 °C and with the dosing manifold controlled at 40°C to avoid unwanted condensation effects. Helium was used to estimate the dead volume prior to the water adsorption-desorption measurements. Adsorption equilibrium was assumed when the variation of the cell pressure was 0.5% for a minimum period of 300 seconds.

7.1.7 High pressure powder x-ray diffraction additional data

High pressure powder X-ray (HPPXRD) experiments were performed at the Diamond Lightsource (beamline I15) with an X-ray energy of 29.2 keV ((λ = 0.4246 Å) and a 2D PerkinElmer area detector for data collection within beam time EE19187-1. The applied high-pressure cell is described in detail at https://www.imperial.ac.uk/pressurecell/. Briefly, for HPPXRD measurements UiO-66 samples were filled into plastic capillaries (inside diameter 1.8 mm) together with Silicone AP oil 100 as pressure transmitting medium. The capillaries were sealed with Araldyte-2014-1. The plastic capillaries were then loaded into the sample chamber, a metal block filled with water. The pressure to the material is applied by increasing the inside water pressure with hydraulic gauge pumps and HPPXRD is performed through two diamond windows in the metal block. Due to sample mounting and sealing, the initial calibration of the sample-to-detector distance is likely to be affected which was considered during the evaluation of the bulk modulus, see below.

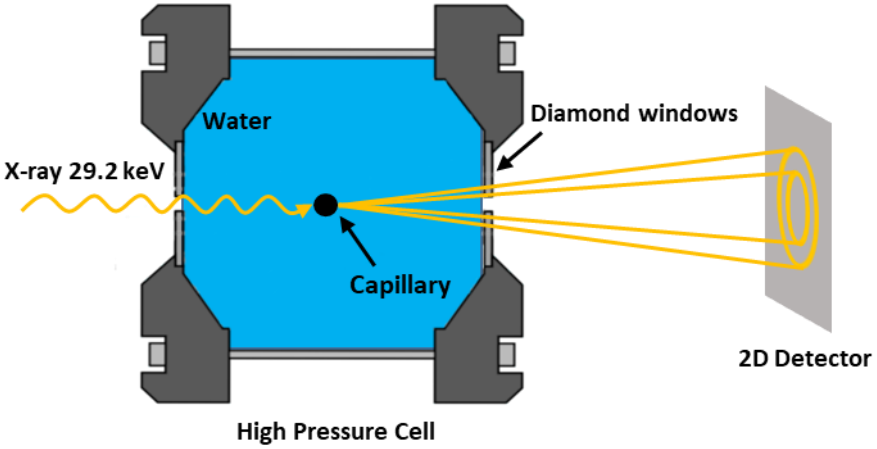

Figure 7.2: Schematic representation of the high pressure cell used at diamond light source at beamline I15.

Pawley profile fits of the data were performed using TOPAS v5 to extract lattice parameters and volumes as a function of pressure. As mentioned above, lattice parameters and volume that come out of the profile fits might be offset due to inaccuracies of the sample-to-detector distance. We would like to highlight here, however, that this does not affect the relative changes which are important for obtaining the bulk modulus. The bulk moduli reported in table S1 were obtained by fitting a 2nd and 3rd order Birch-Murnaghan equation of state (BM EoS) to the obtained data. As described in the main text, we decided to use only the first 8

pressure points up to 0.175 GPa for the BM fit, due to an unusual discontinuity in the V(p) behaviour of defective samples (see raw data in tables 7.2 - 7.5).

During the refinement with the program TOPAS V5, errors were also estimated as standard deviation (σ). In particular, σ(V) was then included in the fitting process of the program EoSFit7c by R. J. Angel. These values were then used by the program to calculate the bulk modulus by fitting a 2nd order BM EoS. The maximum error that we found for our values was 0.22 GPa as reported in Table 7.1 and in table 4.2 in the main manuscript. Another aspect that might be worth to be discussed are the bulk modulus first derivative values (K'_{3rd}), see Table 7.1. A negative K'_{3rd} indicates that the framework becomes more compressible with increasing pressure. This could be counterintuitive at first sight, however, Chapman et al. in 2009 proposed that negative K'_{3rd} values may be relatively common in open framework solids (as we found here for UiO-66) since the volume reduction at moderate pressure is not sufficient to bring atoms into unfavourably close contact.

Table 7.1: The P-V data values for all UiO-66 sample were fitted to the 2nd and 3rd order BM EoS using the EoSFit7-Gui program by R. J. Angel. These values are obtained using a fixed value of V_0 equal to 1 in the pressure range p= ambient to 0.175 GPa.

Sample name	K_{2nd} [GPa]	K'_{2nd}	K_{3rd}[GPa]	K'_{3rd}
UiO-66-0eq	26.4 ± 0.13	4	27.5	-12.9
UiO-66-1eq	18.3 ± 0.16	4	18.9	-5.4
UiO-66-5eq	12.2 ± 0.18	4	13.7	-15.1
UiO-66-10eq	13.9 ± 0.22	4	15.4	-17.9

Table 7.2: Cell parameters (lpa), Volume (V), R_wp value and full width half maximum (FWHM) for the sample UiO-66-0eq in each pressure step.

Pressure [GPa]	lpa	rel. lpa	V [Å^3]	σ(V)	rel. V	R_wp	FWHM	Rel FWHM
0.0001	20.73733	1	8917.81981	0.307	1	1.76279	0.02168	1
0.025	20.73124	0.9997063	8909.9556	0.25	0.999118147	1.72493	0.02111	0.973708487
0.050	20.7244	0.9993765	8901.15009	0.264	0.99813074	1.64751	0.02083	0.960793358
0.075	20.71813	0.9990741	8893.0658	0.239	0.997224208	1.67797	0.02081	0.959870849
0.100	20.7118	0.9987689	8884.91686	0.231	0.996310427	1.62178	0.02051	0.94603321
0.125	20.70519	0.9984501	8876.41647	0.229	0.995357235	1.66745	0.02102	0.969557196
0.150	20.69831	0.9981184	8867.56901	0.394	0.994365125	1.77622	0.02195	1.012453875
0.175	20.69159	0.9977943	8858.94004	0.306	0.993397515	1.83202	0.02272	1.04797048
0.200	20.68368	0.9974129	8848.77708	0.311	0.992257891	1.86088	0.02357	1.087177122
0.225	20.67593	0.9970392	8838.83791	0.329	0.991143362	1.82389	0.0245	1.130073801
0.250	20.6687	0.9966905	8829.56386	0.312	0.990103416	1.87691	0.02545	1.173892989
0.275	20.66072	0.9963057	8819.34421	0.355	0.988957436	1.91286	0.02623	1.209870849
0.300	20.65288	0.9959276	8809.31226	0.465	0.987832503	2.07277	0.02717	1.253228782
0.325	20.64534	0.995564	8799.66111	0.38	0.986750271	2.27571	0.02664	1.228782288
0.350	20.63864	0.9952409	8791.1057	0.638	0.985790909	2.5196	0.02604	1.201107011
0.375	20.63233	0.9949367	8783.03803	0.73	0.984886241	2.73997	0.02516	1.160516605
0.400	20.62602	0.9946324	8774.98218	0.363	0.983982898	2.96185	0.0242	1.116236162

Table 7.3: Cell parameters (lpa), Volume (V), R_wp value and full width half maximum (FWHM) for the sample UiO-66-1eq in each pressure step.

Pressure [GPa]	lpa	rel. lpa	V [Å^3]	σ(V)	rel. V	R_wp	FWHM	Rel. FWHM
0.0001	20.63428	1	8785.5245	1.135	1	2.89116	0.02641	1
0.025	20.6257	0.999584	8774.5737	1.19	0.99875354	3.0265	0.02859	1.082544491
0.050	20.61825	0.999223	8765.0753	1.438	0.99767241	3.46437	0.01696	0.642180992
0.075	20.60641	0.998649	8749.9838	1.275	0.99595464	3.15719	0.02875	1.088602802
0.100	20.59815	0.998249	8739.4582	1.274	0.99475657	3.15552	0.02914	1.103369936
0.125	20.58667	0.997693	8724.8532	1.247	0.99309418	3.14801	0.03011	1.140098448
0.150	20.57795	0.99727	8713.7766	1.406	0.9918334	3.40743	0.02082	0.788337751
0.175	20.56991	0.99688	8703.5663	0.752	0.99067123	3.25175	0.02425	0.918212798
0.200	20.56272	0.996532	8694.4402	0.367	0.98963246	3.18376	0.02677	1.0136312
0.225	20.55353	0.996087	8682.7844	1.05	0.98830576	3.66709	0.01746	0.661113215
0.250	20.54473	0.99566	8671.6443	1.433	0.98703776	3.60732	0.02298	0.870124953
0.275	20.53538	0.995207	8659.8086	1.355	0.98569056	3.58054	0.02365	0.895494131
0.300	20.52406	0.994658	8645.4908	1.963	0.98406087	3.70755	0.01173	0.444149943
0.325	20.51344	0.994144	8632.0775	1.713	0.98253412	3.84581	0.01704	0.645210148
0.350	20.49912	0.99345	8614.0108	1.869	0.98047769	4.03828	0.01596	0.604316547
0.375	20.48508	0.992769	8596.3307	2.188	0.97846528	4.10636	0.01006	0.38091632
0.400	20.47926	0.992487	8588.9978	2.551	0.97763063	4.44331	0.01632	0.617947747

Table 7.4: Cell parameters (lpa), Volume (V), R_wp value and full width half maximum (FWHM) for the sample UiO-66-5eq in each pressure step. In light orange are highlighted the anomalous values of the FWHM peak shape function.

Pressure [GPa]	lpa	rel. lpa	V [Å^3]	σ(V)	rel. V	R_wp	FWHM	Rel. FWHM
0.0001	20.64244	1	8795.95688	0.812	1	3.3899	0.0172	1
0.025	20.63387	0.9995848	8785.00505	0.828	0.9987549	3.10059	0.01816	1.055813953
0.050	20.61703	0.998769	8763.51003	0.815	0.99631116	3.03744	0.01979	1.150581395
0.075	20.60175	0.9980288	8744.04048	0.723	0.9940977	2.68962	0.01776	1.03255814
0.100	20.58847	0.9973855	8727.14117	0.696	0.99217644	2.52938	0.01603	0.931976744
0.125	20.57463	0.996715	8709.55346	0.632	0.99017692	2.50001	0.01426	0.829069767
0.150	20.56055	0.9960329	8691.68611	0.639	0.9881456	2.54742	0.01321	0.768023256
0.175	20.54374	0.9952186	8670.3905	0.698	0.98572453	2.69238	0.01339	0.778488372
0.200	20.5232	0.9942236	8644.40907	0.717	0.98277074	2.7276	0.01447	0.84127907
0.225	20.49727	0.9929674	8611.68414	0.935	0.97905029	2.69674	0.01825	1.061046512
0.250	20.47119	0.991704	8578.85448	0.817	0.97531793	2.49606	0.01738	1.010465116
0.275	20.45763	0.9910471	8561.81285	0.957	0.97338049	2.93106	0.01	0.581395349
0.300	20.46146	0.9912326	8566.62334	1.413	0.97392739	3.376	0.01	0.581395349
0.325	20.4438	0.9903771	8544.46273	3.541	0.97140798	4.01845	0.01	0.581395349
0.350	20.37806	0.9871924	8462.30399	5.77	0.96206747	2.68833	0.012	0.697674419
0.375	20.30746	0.9837723	8374.65164	6.691	0.9521024	1.89082	0.07331	4.262209302
0.400	20.21836	0.9794559	8264.90822	6.75	0.93962582	1.10034	0.16198	9.41744186

Table 7.5: Cell parameters (lpa), Volume (V), R_wp value and full width half maximum (FWHM) for the sample UiO-66-10eq in each pressure step. In light orange are highlighted the anomalous values of the FWHM peak shape function.

Pressure [GPa]	lpa	rel. lpa	V [Å^3]	σ(V)	rel. V	R_wp	FWHM	Rel. FWHM
0.0001	20.68695	1	8852.9799	0.312	1	1.32783	0.02039	1
0.025	20.67794	0.99956446	8841.4191	0.276	0.998694133	1.23312	0.02137	1.048062776
0.050	20.66312	0.998848066	8822.4201	0.275	0.99654808	1.41861	0.02327	1.141245709
0.075	20.65158	0.998290226	8807.6514	0.123	0.994879863	1.45656	0.02233	1.095144679
0.100	20.63909	0.997686464	8791.6732	0.358	0.993075025	1.45854	0.02054	1.007356547
0.125	20.62577	0.99704258	8774.6592	0.37	0.991153179	1.51695	0.01891	0.9274154
0.150	20.6124	0.996396279	8757.6122	0.283	0.989227615	1.53217	0.0177	0.868072585
0.175	20.5982	0.995709856	8739.5223	0.43	0.987184249	1.62465	0.0178	0.872976949
0.200	20.58247	0.994949473	8719.5234	0.723	0.984925244	1.81266	0.01506	0.738597352
0.225	20.56117	0.993919838	8692.4813	1.395	0.981870673	1.97744	0.01	0.490926925
0.250	20.53316	0.992565845	8656.9932	2.527	0.977862064	1.85846	0.01	0.490436488
0.275	20.51589	0.991731019	8635.1703	3.862	0.975397034	1.58377	0.01	0.490436488
0.300	20.47995	0.989993692	8589.871	4.814	0.970280184	1.33958	0.00111	0.05443845
0.325	20.45262	0.988672569	8555.5328	5.945	0.966401473	1.2259	0.0268	1.314369789
0.350	20.39879	0.986070445	8488.1544	7.546	0.958790651	1.02135	0.05788	2.838646395
0.375	20.34015	0.983235808	8415.1613	10.287	0.950545628	0.84772	0.12903	6.328102011
0.400	20.30035	0.98131189	8365.8622	11.463	0.944976979	0.66252	0.17963	8.809710642

7.1.7.1 Pawley profile fits of laboratory data

Pawley fitting is a process in which observed peaks in a powder pattern are fitted without a structural model but at 2θ values constrained by the size and symmetry of the unit cell. It is a useful precursor to Rietveld fitting and gives an indication of the "best fit possible" from an eventual structural refinement. Basically the refinement is based only on geometrical inputs, i.e space group a,b,c and angles of the unit cell. UiO-66 has a cubic space group which is Fm-3m, so a = b = c = 20.74 and α = β = γ = 90.

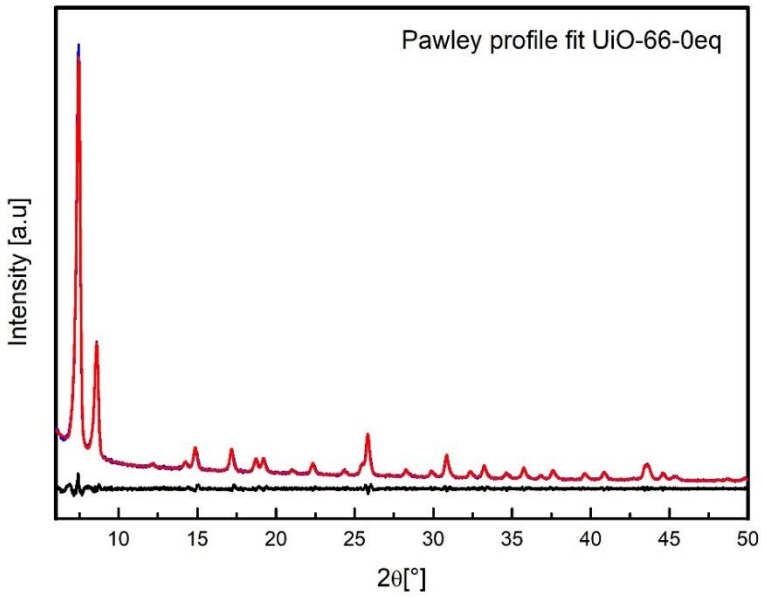

Figure 7.3: Pawley profile fit of UiO-66-0eq. Space group: Fm-3m with Rwp: 3.92 and χ^2:1.68. In blue the experimental diffraction pattern in red the profile fit and in black the difference curve.

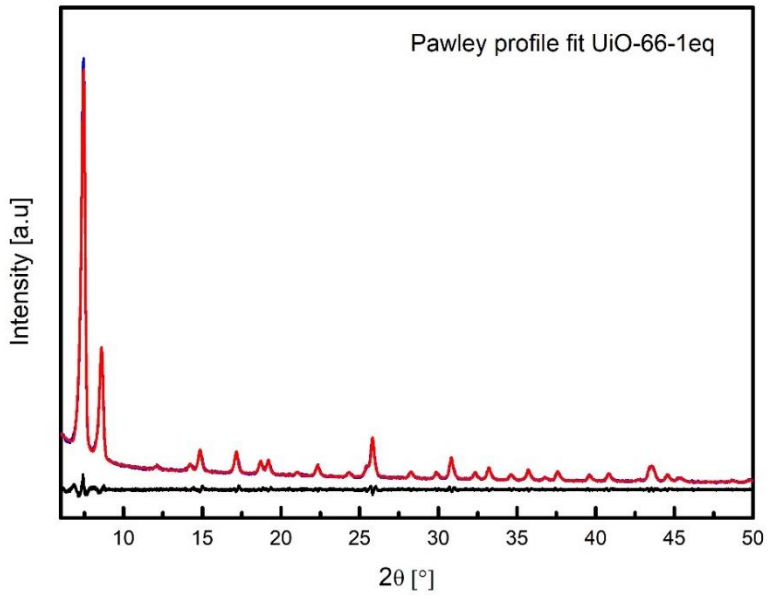

Figure 7.4: Pawley profile fit of UiO-66-1eq. Space group: Fm-3m with Rwp: 3.32 and χ^2: 0.77. In blue the experimental diffraction pattern in red the profile fit and in black the difference curve.

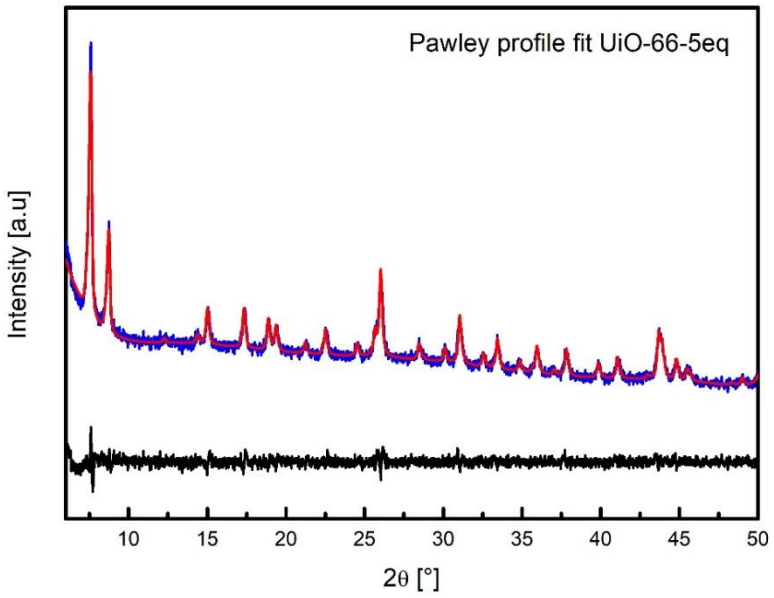

Figure 7.5: Pawley profile fit of UiO-66-5eq. Space group: Fm-3m with Rwp: 3.16 and χ^2:1.41. In blue the experimental diffraction pattern in red the profile fit and in black the difference curve.

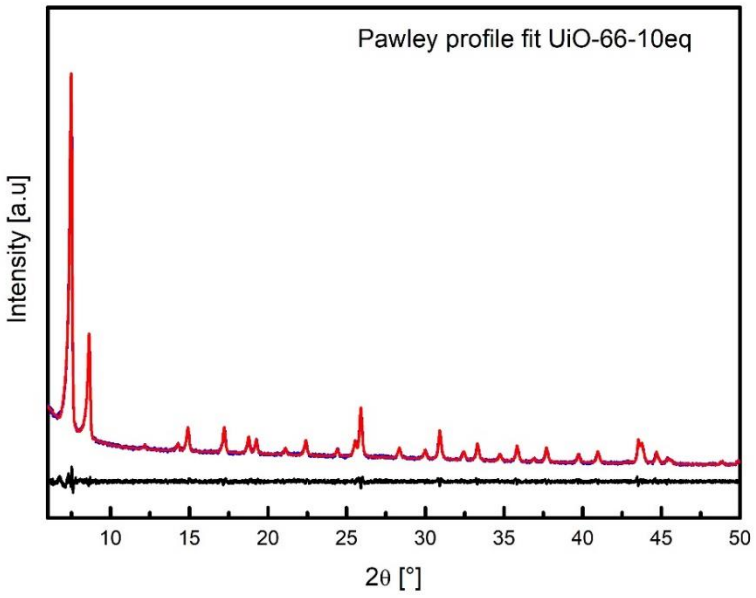

Figure 7.6: Pawley profile fit of UiO-66-10eq. Space group: Fm-3m with Rwp: 3.17 and χ^2:1.47. In blue the experimental diffraction pattern in red the profile fit and in black the difference curve.

7.1.7.2 Stacking plot of high pressure powder x-ray diffraction patterns

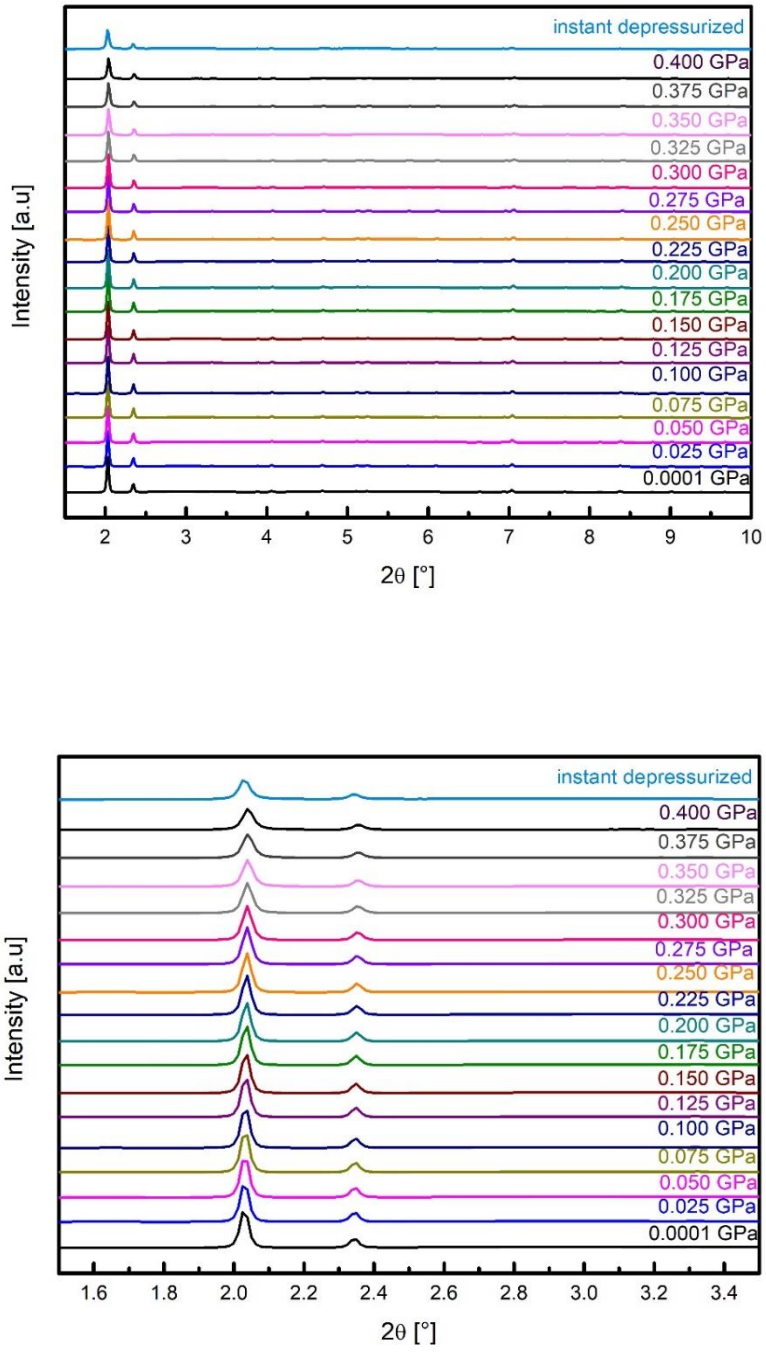

Figure 7.7: Top panel: HPXRD of UiO-66-0eq in the range 0.1 MPa - 0.4 GPa. Bottom panel: zoom of the 1.5 - 3.5 2θ region, showing that there is no loss of crystallinity in pressure range applied.

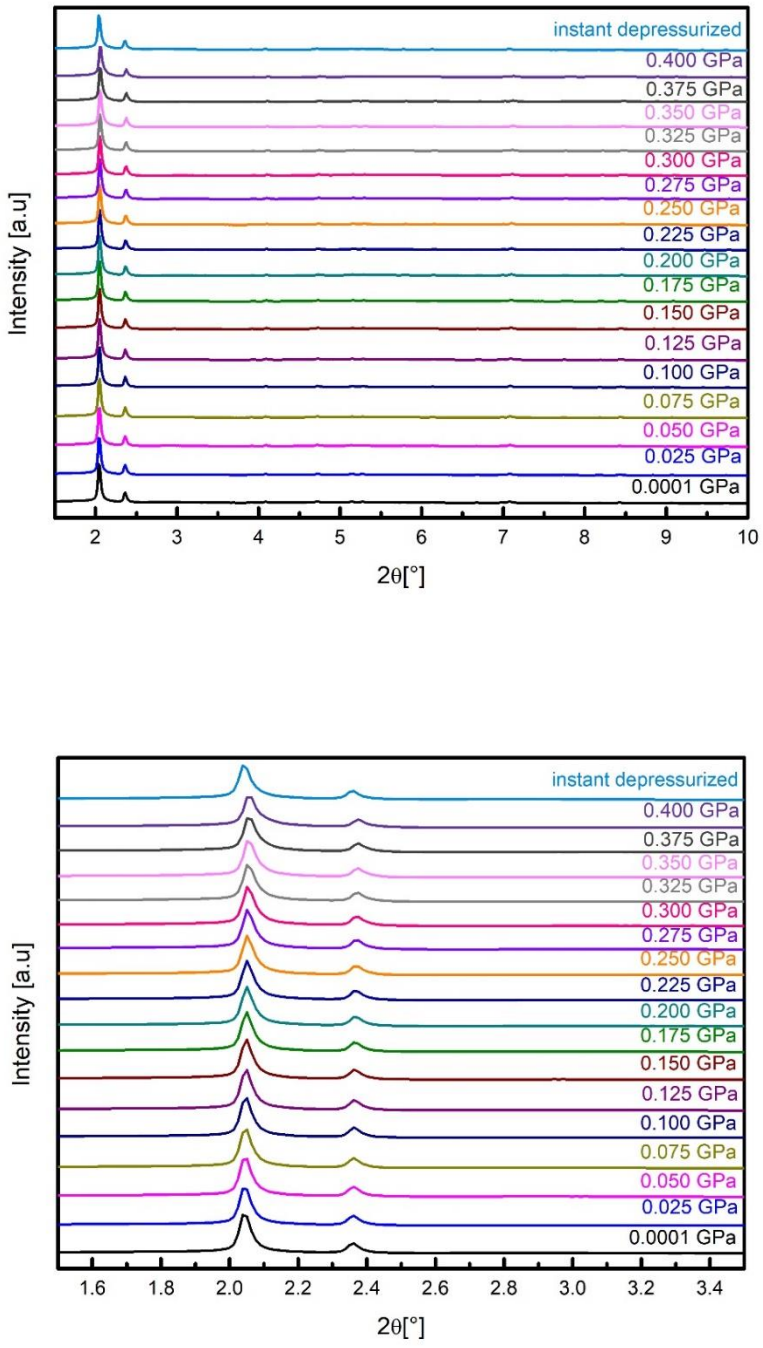

Figure 7.8: Top panel: HPXRD of UiO-66-1eq in the range 0.1 MPa - 0.4 GPa. Bottom panel: zoom of the 1.5 - 3.5 2θ region, showing that there is no loss of crystallinity in pressure range applied.

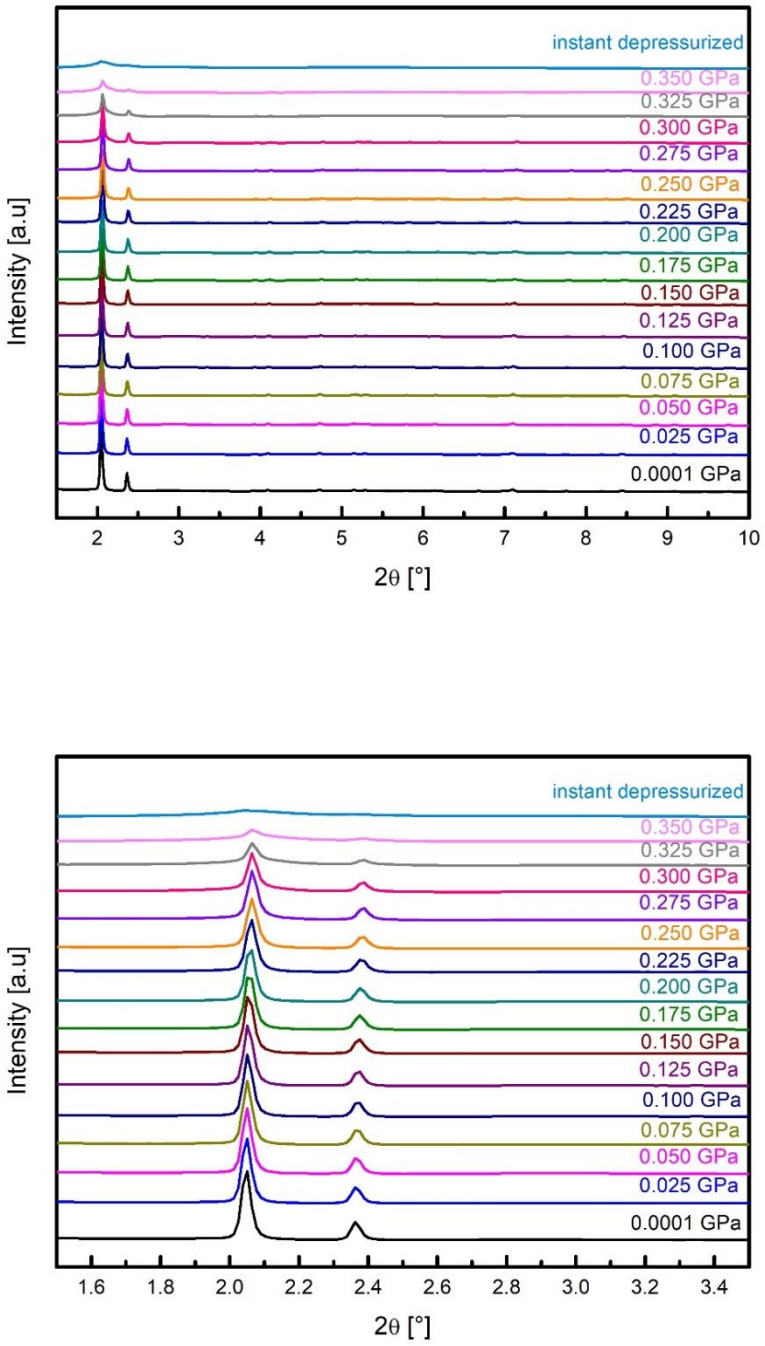

Figure 7.9: Top panel: HPXRD of UiO-66-5eq in the range 0.1 MPa - 0.4 GPa. Bottom panel: zoom of the 1.5 - 3.5 2θ region in the range 0.1 MPa - 0.35 GPa, where an onset of amorphization is observed at approximately 0.275 GPa.

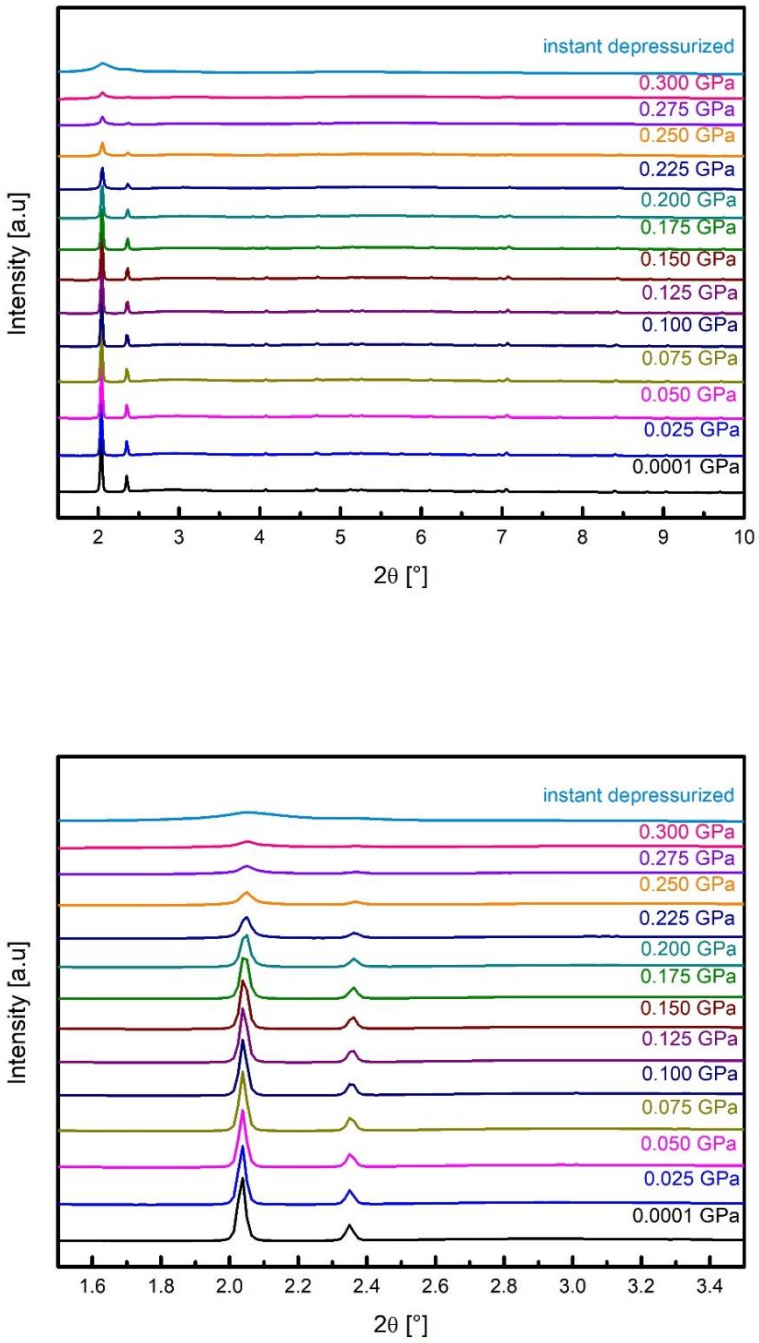

Figure 7.10: Top panel: HPXRD of UiO-66-10eq in the range 0.1 MPa - 0.3 GPa. Bottom panel: zoom of the 1.5 - 3.5 2θ region between 0.1 MPa - 0.3 GPa, where an onset of amorphization is observed at approximately 0.225 GPa.

7.1.7.3 Amorphization onset and bulk moduli of different type of zeolites

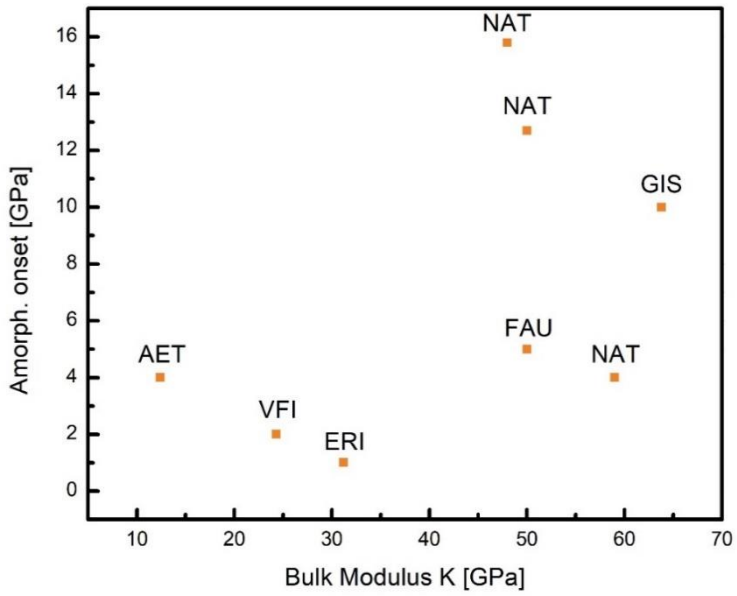

Figure 7.11: Bulk moduli and amorphization onset for different type of zeolites. Detailed values are listed in table 7.6.

Table 7.6: Bulk Moduli and and amorphization onset of different type of Zeolites.

Zeolites	Framework Type Code	Bulk Modulus K [GPa]	P. Onset amorph. [GPa]	REF
$AlPO_4$-17	ERI	31.2	1	[145]
Zeolite X	FAU	50	5	[146]
Na-NAT	NAT	48	15.8	[147]
$ALPO_4$-8	AET	12.4	4	[148]
$ALPO_4$-54	VFI	24.3	2	[149]
Li-NAT	NAT	50	12.7	[147]
Natrolite (natural)	NAT	59	4	[147]
Gismondine	GIS	63.8	10	[150]

¥ For additional information please visit the website http://europe.iza-structure.org/IZA-SC/ftc_table.php

A brief literature research of a possible link between bulk modulus and onset of amorphization of Zeolites was performed. From figure 7.11, it is apparent that there is no obvious correlation between these two parameters. It seems reasonable to think that also in MOFs there is not such a simple correlation due to the known similarities that zeolites and MOFs shares.

7.1.8 Induced coupled plasma (ICP)

For the quantification of Zr and Pt in the synthesized Pt@MOF-808 materials, around 15 mg of each sample (15,3 mg) was digested in 3 mL sulfuric acid, heated until complete dissolution. Once at room temperature 3 drops of H_2O_2 were added and then water milli-Q was used to fill 50ml volumetric flask. The measurement were performed by Andreas Wimmer at TUM in the chair of Prof. Michael Schuster.

The digests were then diluted with ultra-pure water and acidified to 3 % (v/v) hydrochloric acid (suprapure, Merck) for Zr and Pt and 3 % (v/v) nitric acid (suprapure, Merck) for Cu. Quantification was carried out with a 7900 ICP-MS (Agilent) equipped with a SPS4 autosampler (Agilent). Target masses were chosen as follows: 63Cu, 90Zr, 195Pt with an integration time of each 200 ms. No isobaric interferences occured for these selected masses. 115In and 153Eu were used as internal standard to perform plasma corrections. Measurements were carried out in He collision mode to avoid any polyatomic interferences. Solutions for calibration containing the target elements in the concentration range from 50 ng L-1 to 10 µg L-1 were prepared from element standards Merck IV for Cu (Merck, β = 1000 mg L-1) and Periodic Table Mix 2 for Zr and Pr (Merck, β = 10 mg L-1). All digested samples were diluted independently in duplicate prior to measurement and measured each diluted sample in triplicate. Given concentrations are the mean values for each samples, uncertainties are based on calculations using Gaussian error propagation (U, k = 2).

7.1.9 Gas Chromatography (GC)

Gas chromatography were performed with the instrument Agilent Technologies model 7890B with an auto-sampler model 7693. The GC is equipped with a non-polar 30 m long capillary column and a flame ionization detector (FID) that responds to the most organic compounds.

7.1.10 Variable temperature x-ray diffraction (VTXRD)

Variable temperature x-ray diffraction were performed at University of Augsburg in the chair of professor Dirk Volkmer. The measurement were performed with a Bruker Panalitical Empyrean instrument with an X-ray energy of 8.04 keV (Cu Kα λ = 1.5406 Å) equipped with a variable temperature controlled chamber. The measurement were performed

both in a flat mode under a continuous flow of N_2 and also in capillary mode with a hot air blower.

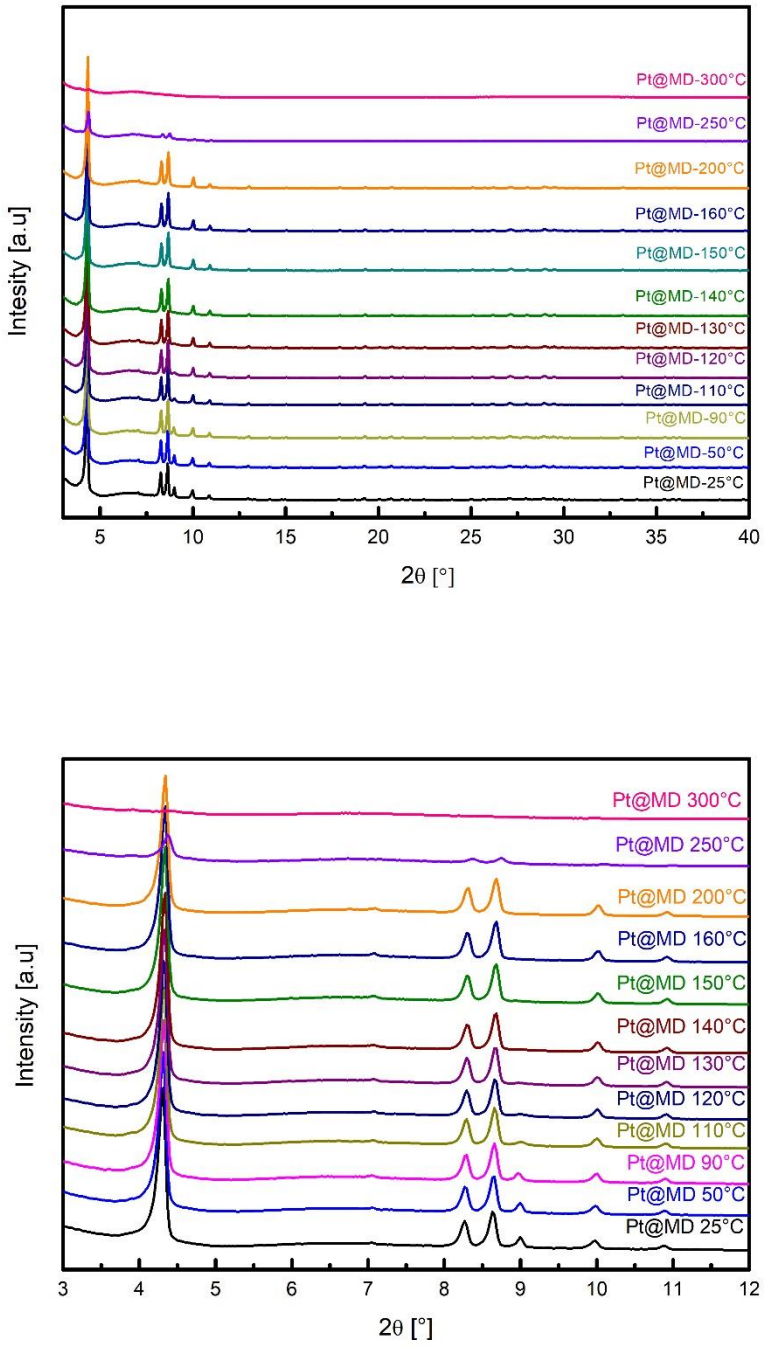

Figure 7.12: top panel full range VTXRD of Pt@MD in the range 25 – 300°C. Bottom panel: zoom of the 3 - 12 2θ region, where a clear loss of crystallinity is observed above 200°C.

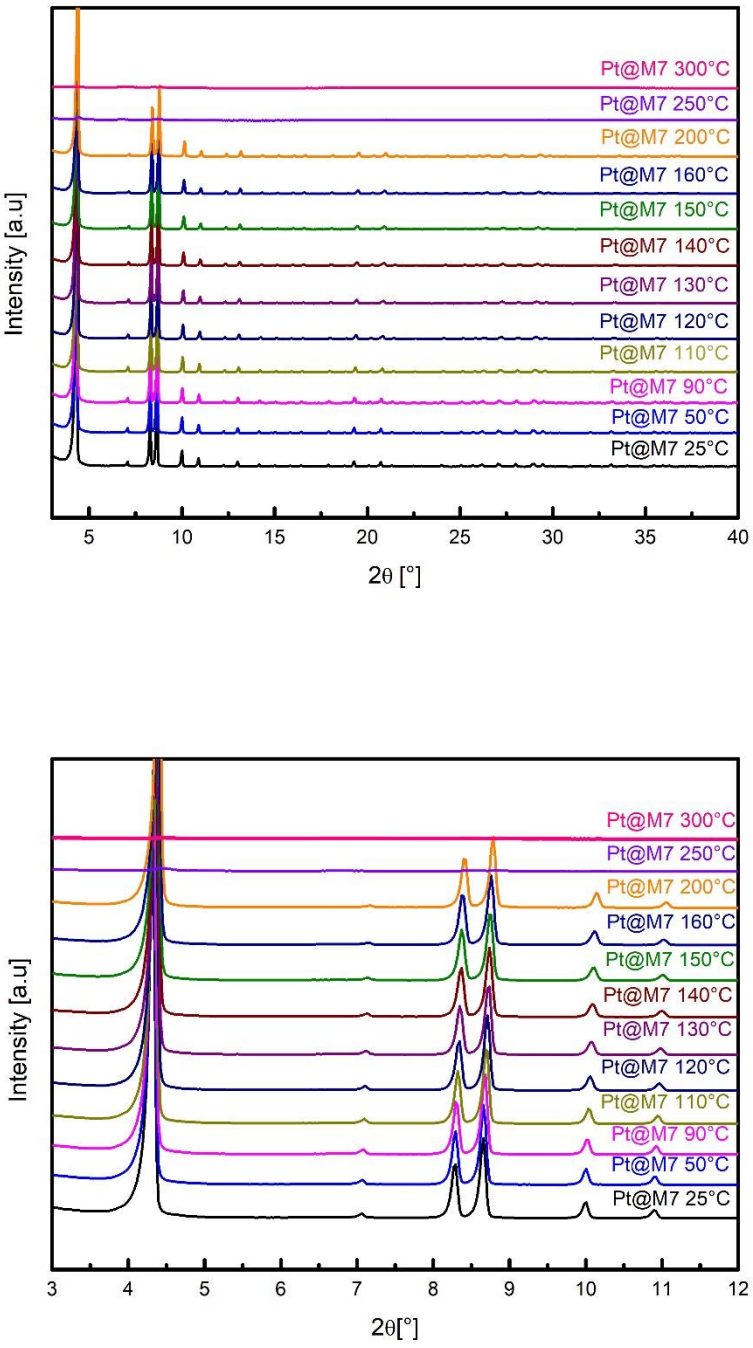

Figure 7.13: top panel full range VTXRD of Pt@M7 in the range 25 – 300°C. Bottom panel: zoom of the 3 - 12 2θ region, where a clear loss of crystallinity is observed above 200°C.

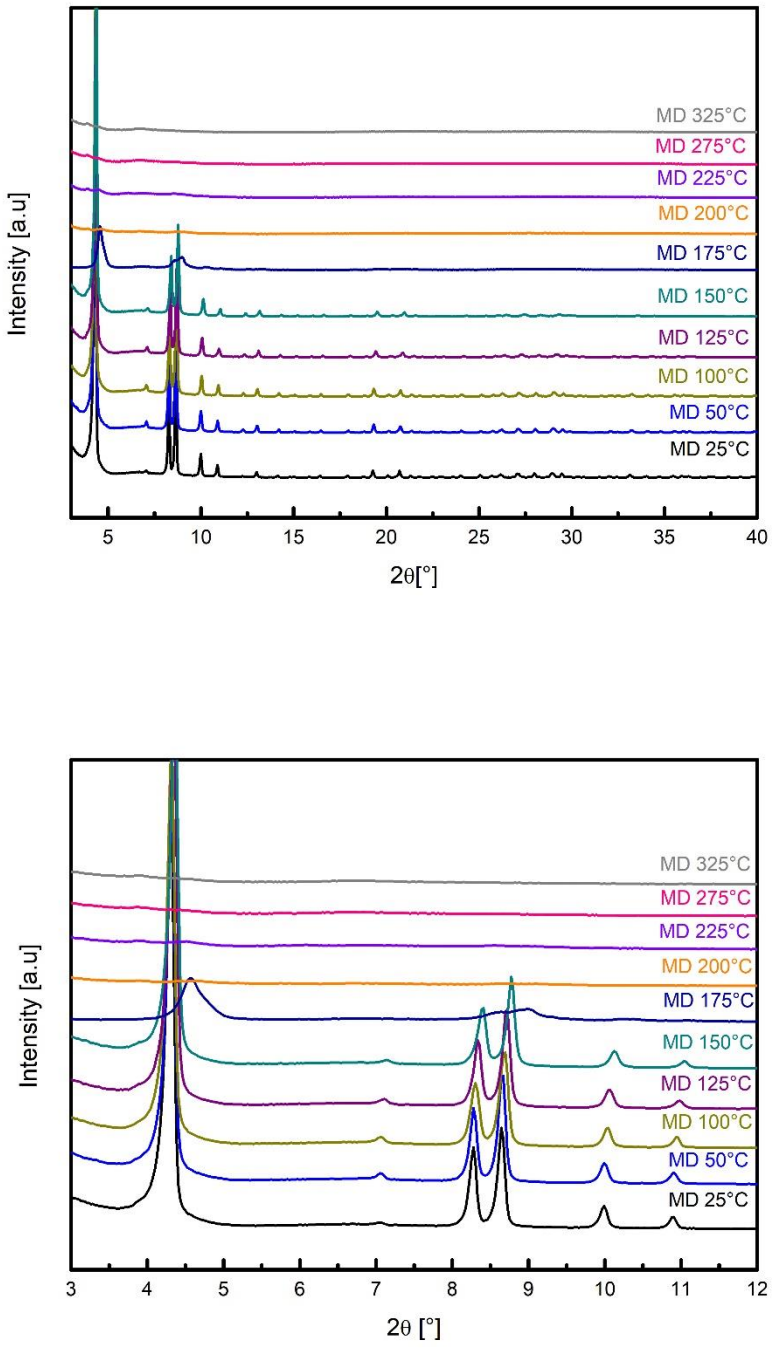

Figure 7.14: top panel full range VTXRD of MD sample in the range 25 – 325°C. Bottom panel: zoom of the 3 - 12 2θ region, where a clear loss of crystallinity is observed at 175°C.

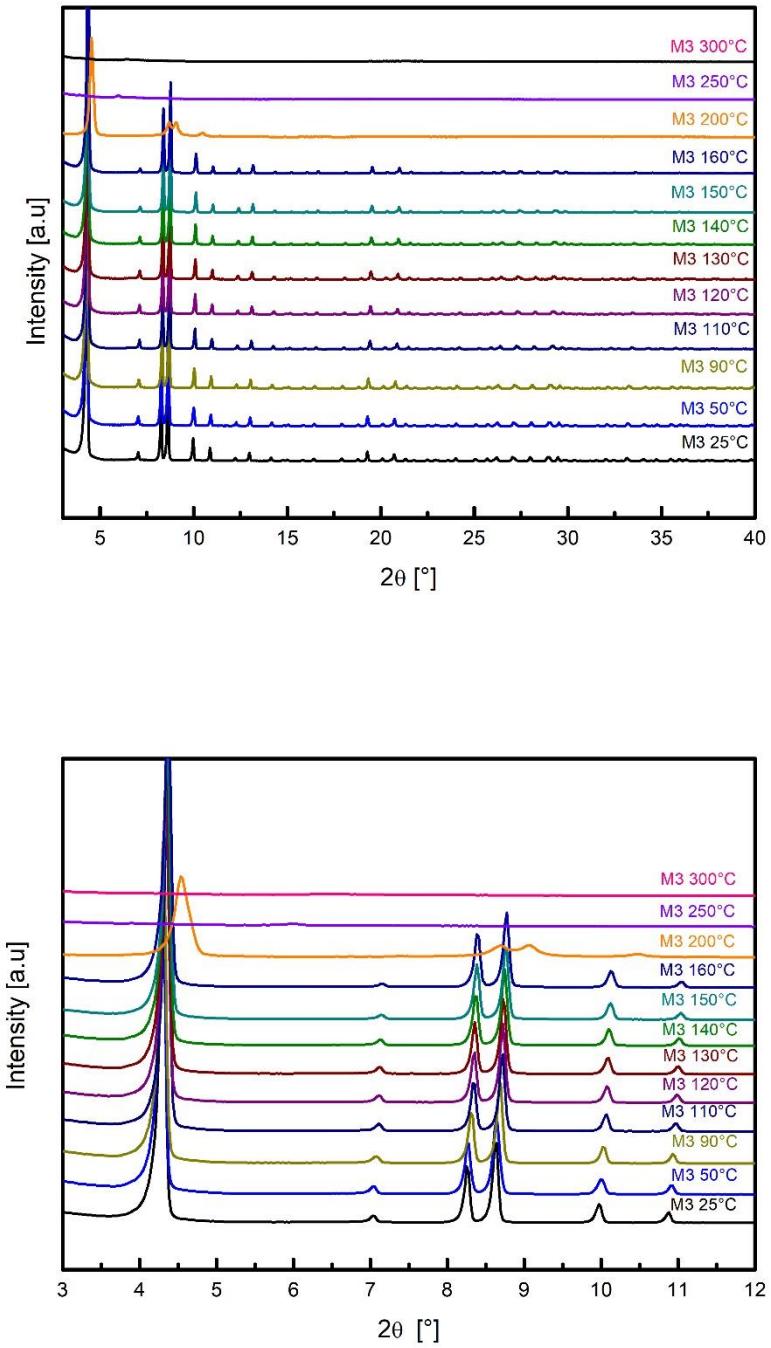

Figure 7.15: top panel full range VTXRD of M3 sample in the range 25 – 300°C. Bottom panel: zoom of the 3 - 12 2θ region, where a clear loss of crystallinity is observed at 200°C.

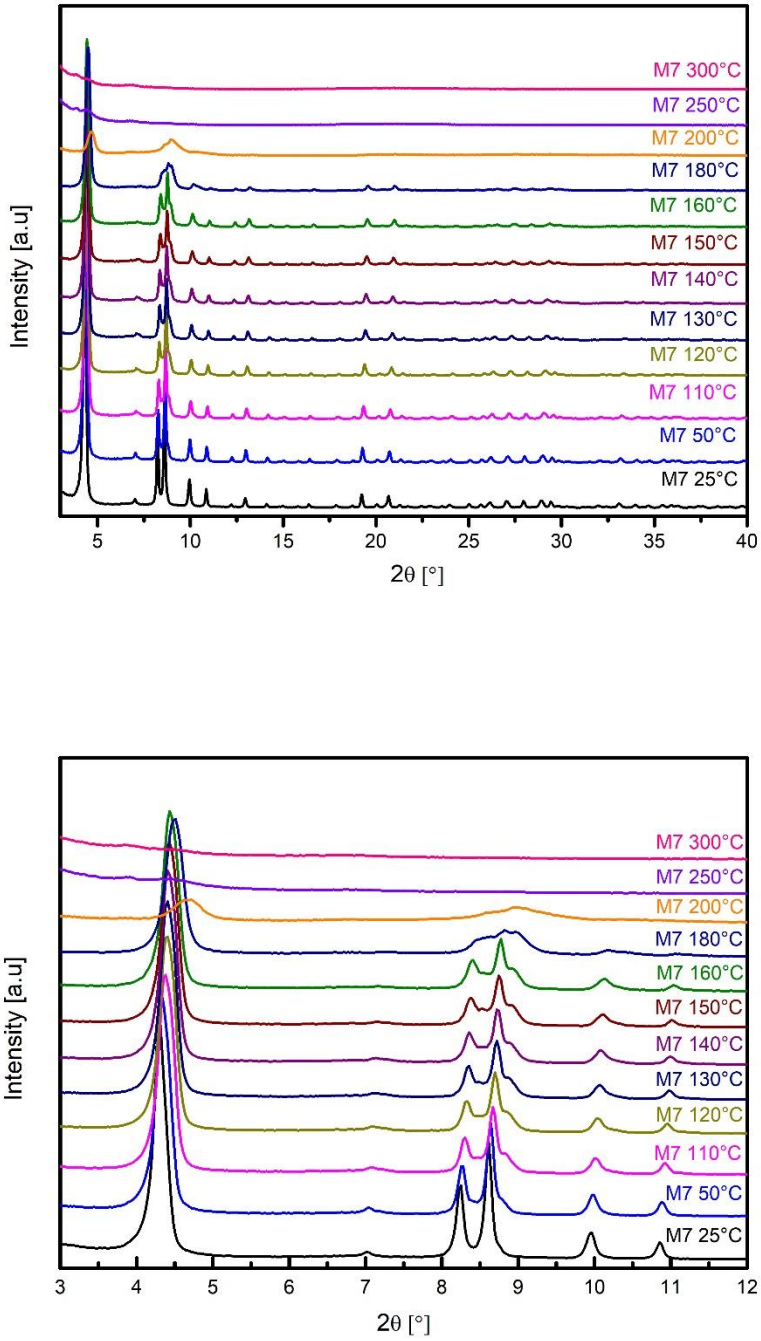

Figure 7.16: top panel full range VTXRD of M7 sample in the range 25 – 300°C. Bottom panel: zoom of the 3 - 12 2θ region, where a clear loss of crystallinity is observed starting at 160°C.

7.1.11 Scanning electron microscopy (SEM)

Scanning Electron Microscopy (SEM) was performed in Aix-Marseille University in Marseille with a Zeiss Gemini 500 instrument. The voltage was varied from 0.5 to 5 kV to find optimum conditions to have a compromise between suppression of charge effect and lateral resolution. The working distance between camera and sample was maintained at 1.8 mm or 0.9 mm to enhance the resolution. Energy dispersive X-ray spectroscopy (EDX) was carried out simultaneously to estimate the elemental compositions.

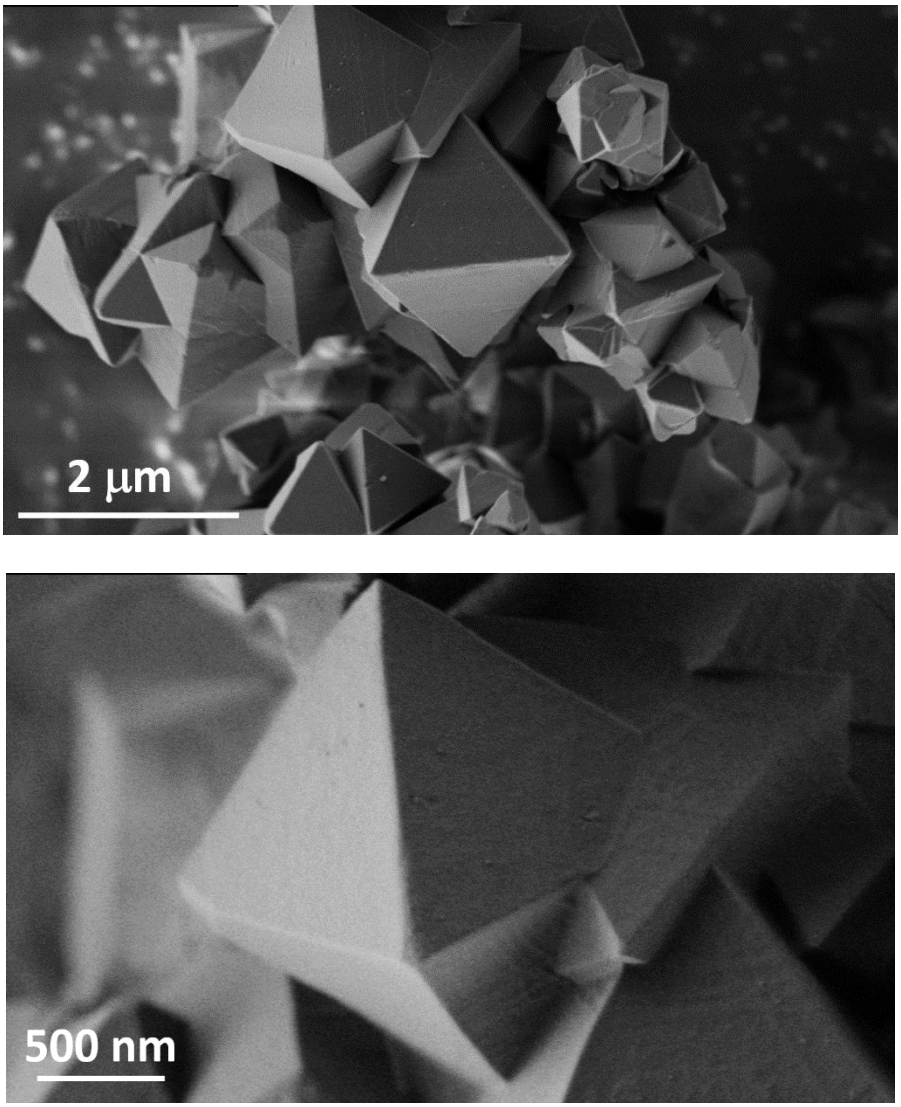

Figure 7.17: SEM pictures of Pt@M7 sample (one of the Pt@MOF-808 samples described in chapter 5). Top panel: overview picture of the sample where big crystals with smooth surface can be seen. Bottom panel: zoom in where is possible to see the perfect octahedral shape of Pt@M7 crystals.

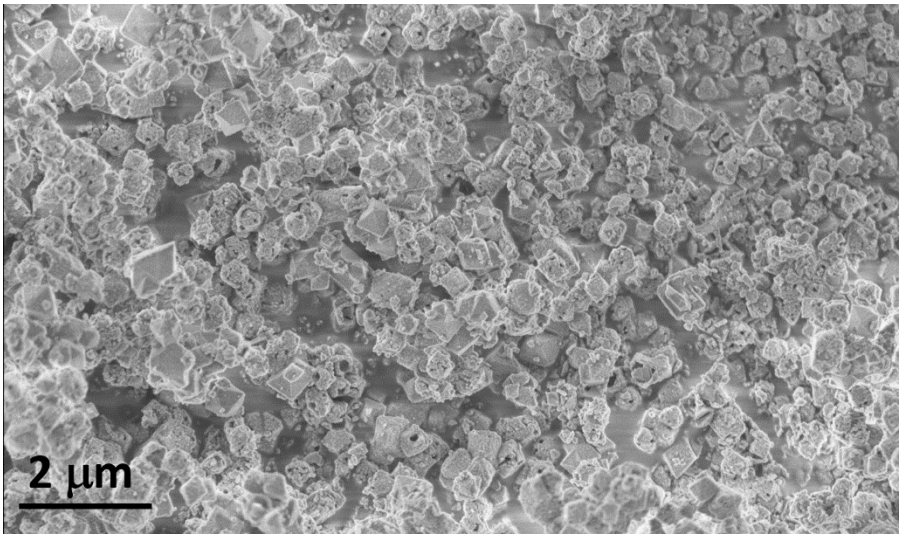

Figure 7.18: SEM pictures of Pt@MD sample (one of the Pt@MOF-808 samples described in chapter 5). Overview picture where is possible to see the relative abundance of the "hollow" structure described in chapter 6. The ratio between hollow and filled crystal is 60/40 in favour of the hollow structure.

7.2 Catalytic testing

7.2.1 Cyanocylilation of benzaldehyde

In a typical catalytic experiment 62µL (0.5 mmol) trimethylsilylcyanide (TMSCN), 25 µL (0.25 mmol) benzaldehyde and ~3mg solid catalyst were stirred (~500 rpm) in a sealed finger schlenk under Ar atmosphere at 40 °C in 1 mL DCM. The reaction was followed by taken aliquots at given time intervals that were analyzed by GC and GC-MS. For the analysis by GC the catalyst were filtered of by the use of syringe filters (0.2 µm).

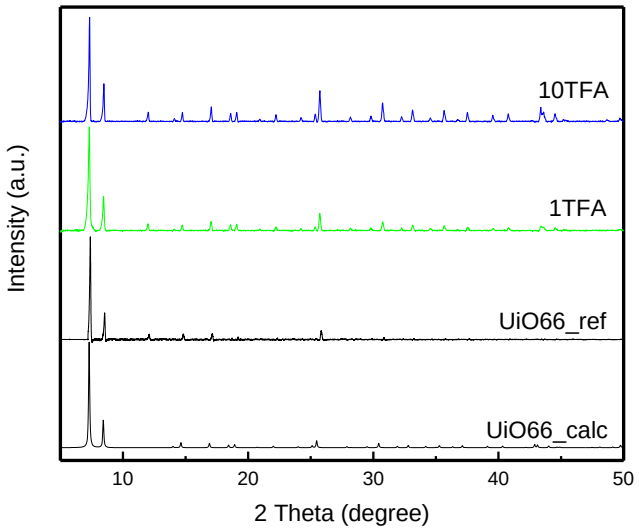

Figure 7.19: Powder X-ray diffractograms of the solid catalyst samples after two catalytic runs.

Table 7.7: Reusability studies for UiO-66 ref, 1TFA and 10TFA which were used as catalysts in the cyanosilylation of benzaldehyde at T = 40 °C in CH_2Cl_2 as solvent. Yield was obtained after 20 h reaction time.

Sample	Yield [%] After reaction	Yield [%] Recycled once	Yield [%] Recycled twice
UiO-66 ref	90	91	88
1TFA	95	95	93
10TFA	96	95	93

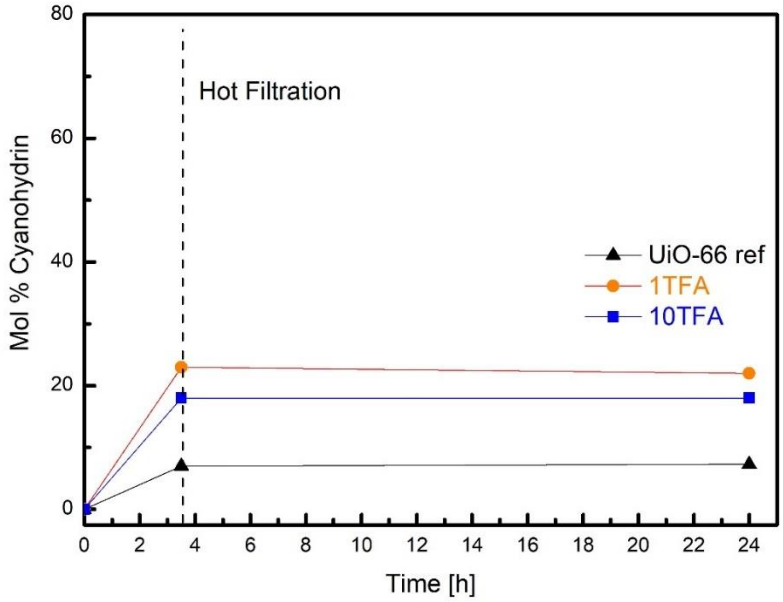

Figure 7.20: Hot filtration test conducted for UiO-66 ref, 1TFA and 10TFA catalysts. The inserted line indicates the time of the hot filtration.

7.2.2 Meerwein–Ponndorf–Verley (MPV) reduction of cyclohexanone

In a typical catalytic experiment 10mg of cyclohexanone and 10 mg of catalyst (MOF-808) were dispersed in 0.5ml of isopropanol (excess) heated at 80°C under air and stirred during the reaction. The reaction was followed by taken aliquots at given time intervals that were analyzed by GC and GC-MS. For the analysis by GC the catalyst were centrifuged by the use of centrifuge at 7000 rpm for 10min. The solution was then transferred in another GC vial and filled with isopropanol if necessary.

7.2.3 Meerwein–Ponndorf–Verley (MPV) reduction of cynnamaldehyde.

In a typical catalytic experiment 39mg of cynnamaldehyde and 7.5 mg of catalyst (MOF-808) were dispersed in 1.8 ml of isopropanol (HPLC grade) heated at 80°C under air and stirred during the reaction. The reaction was followed by taken aliquots at given time intervals that were analyzed by GC and GC-MS. For the analysis by GC the catalyst were filtrated by the use of syringe filters (0.2μm).

7.2.4 Tandem reaction of cynnamaldehyde to hydrocinnamyl alcohol

In a typical catalytic experiment 39mg of cynnamaldehyde and 7.5 mg of catalyst (Pt@MOF-808) were dispersed in 1.8 ml of isopropanol (HPLC grade) heated at 80°C under air and stirred during the reaction. The reaction was performed in a Fischer-porter bottle (80 ml) loaded with 2 Bar of H_2. The reaction was followed by taken aliquots at given time intervals and then analyzed by GC and GC-MS. Prior the GC analysis the aliquots were filtrated by the use of syringe filters (0.2μm).

.

7.3 Material synthesis

7.3.1 Synthesis of Pt NPs

In a typical synthesis, 186 mg of $H_2PtCl_6.6H_2O$ was used as Pt precursor and dissolved with 60 mL distilled water in a beaker glass to make a Pt solution. 399 mg of PVP was dissolved with 540 mL of methanol in a round-bottom flask. The Pt precursor solution was poured into PVP solution and placed in a reflux system at 80°C for 3 hours. When the reaction is finished, methanol solvent was removed by using rotary evaporator until all the methanol solvent is removed and the remaining solutions (around 60 mL distilled water with Pt nanoparticles) is washed with acetone and diethyl ether with the following procedure.

7.3.1.1 Washing and drying procedure for Pt NPs

Every 5 mL of the remaining solution was poured into a centrifuge tube. A mixture of 10 mL diethyl ether and 25 mL acetone was added, and the mixture was centrifuged for 2 minutes at 7800 rpm. After centrifugation, the solvents were separated from the back sol by decantation. To the same centrifuge tube, another 5 mL of the remaining solution from the round-bottom flask was added and washed with acetone and diethyl ether following the same procedure. The washing procedure was repeated until there is no remaining solution left in the round-bottom flask.

The washing procedure was continued by using ethanol and diethyl ether as the following. To the same centrifuge tube that contains the black sol, 5 mL of ethanol was poured, and the tube was shacked until all the black sol dissolved. Once it is dissolved, 35 mL of diethyl ether was poured into the solution and then centrifuged for 2 minutes at 7800 rpm. After centrifugation, check if there is phase separation (clean transparent solution and black sol). The transparent solvent was then removed, and the same procedure was repeated 5-6 times. If after centrifugation there is no phase separation (the solution is still blurry and dark) that indicates too much ethanol in the mixture, so extra additional ether has to be added, then centrifuge again. Once washing is finished, the solvent was removed, and the wet solid was dried in an open air with nitrogen flow at room temperature. The black powder was collected and put it in the glass tube and place the glass tube in a vacuum chamber to be dried at room temperature overnight. After that, flush the glass chamber with nitrogen or

argon to reduce any possible oxidation of Pt NPs if it is not possible to store them in a glovebox.

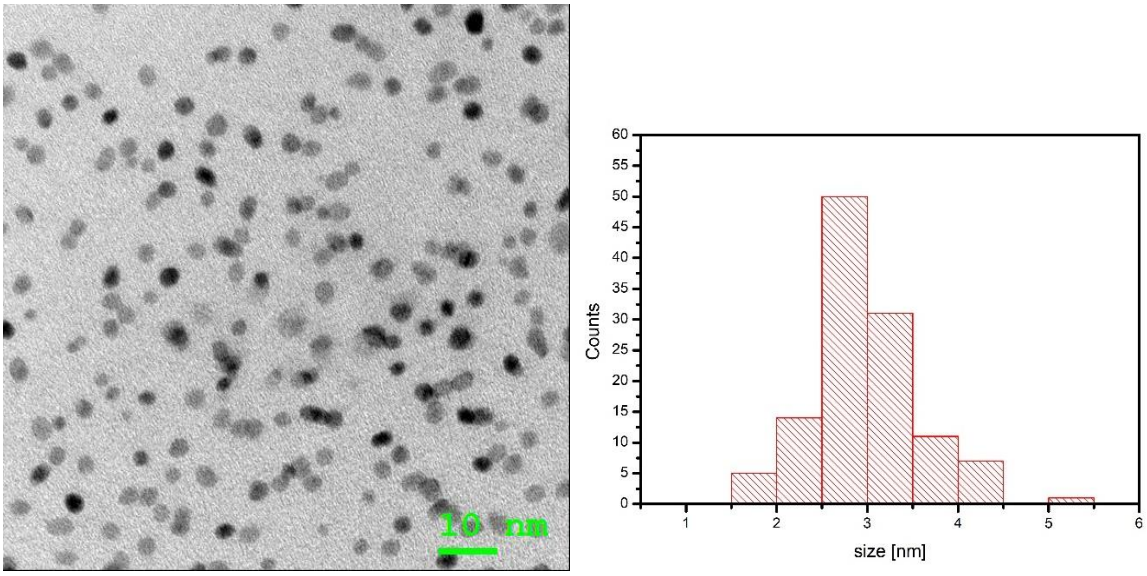

Figure 7.21: left panel representative TEM image of Pt nanoparticles used for the encapsulation inside MOF-808 while on the right panel there is the size distribution graph with an average size of 3 ± 0.6 nm.

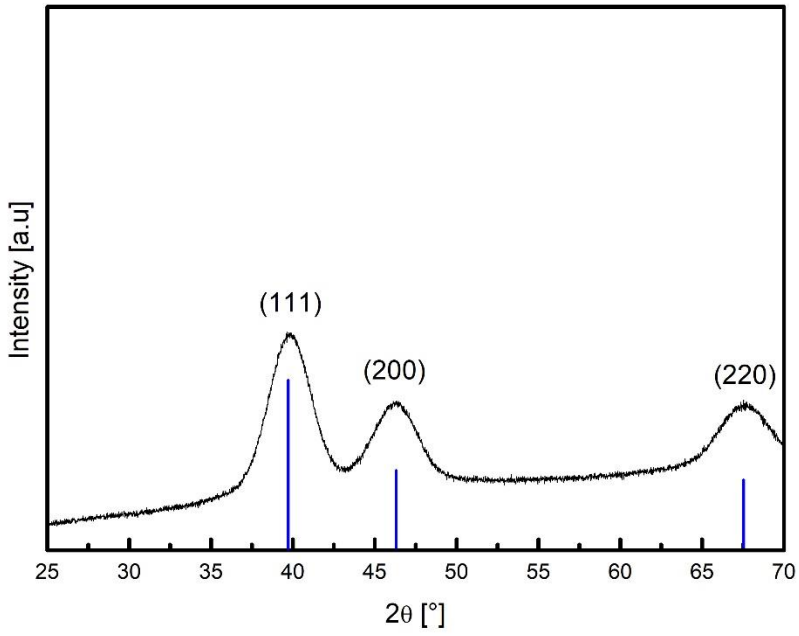

Figure 7.22: PXRD of Pt NPs where the blue lines represent the expected reflection for Pt with exact relative intensities for each reflection. Size distribution calculated by TEM (≈ 3nm) is in agreement with the average size calculated by the Sherrer equation (3.2 nm) considering the full width half maximum of the (111) reflection.

It is worth mention that the quality of PVP capped Pt NPs is crucial for the future encapsulation inside MOF-808 and UiO-66. Meaning that the degree of polymerization (molecular weight) of the polymer and the concentration during solvo-thermal synthesis play an important role for the final position of NP inside the crystals.[151] Very low PVP concentrations lead primarily in core located NPs while higher quantities result in homogeneously distributed NPs on the crystal.[151] If a certain concentration exceed a certain value uncontrollable deposition on the outer surface is observed. Elemental analysis of the Pt NPs used for the encapsulation inside MOF-808 shows a value of 20% of Pt. In previous experiments with UiO-66 materials was shown that a Pt content around 30% ensured an exclusive core location of the NPs inside UiO-66 crystals.

7.3.2 Synthesis of UiO-66, defective UiO-66, MOF-808 and Pt@MOF-808 composites

7.3.2.1 Synthesis of "defect free" UiO-66

The UiO-66-0eq samples was synthesized with a modified procedure of Shearer et al.[2] Typically, 0,945 g of $ZrCl_4$ 1.34 g of terephthalic acid and 0,715 ml of HCl were mixed in 24,35 ml of DMF. The solution was kept in an oven for 24 h at 180°C in a 50 ml teflon liner autoclave. The white powder was then collected via centrifugation washed 3 times with fresh DMF (3 x 30 ml) and solvent exchange with MeOH (3 x 30 ml). The product was heated under vacuum at 250°C overnight, at 300°C for two/three hours and then stored in a glovebox.

7.3.2.2 Synthesis of defective UiO-66 (TFA modulated samples)

TFA modulated samples were synthetized according to the literature procedure. In particular, 3,5 g of $ZrCl_4$ as well as 2,5 g of terephthalic acid with 1,5 ml of HCl were mixed in 155 ml of DMF, with 1 eq (1,15 ml) and 10 eq (11,5 ml) of trifuoro acetic acid (TFA) respect to the amount of zirconium. The resulted materials were collected by centrifugation, washed three times with DMF (3 x 30 ml) and solvent exchange with MeOH (3 x 30 ml) in three days. Then the samples were activated at 150°C for 3 h, 250°C for 12 h and at 320°C for another 12 h under dynamic vacuum. All the samples were stored inside a glovebox.

7.3.2.3 Synthesis of defective UiO-66 (AA modulated samples)

Briefly, for AA modulated samples, 169 mg of $ZrCl_4$ (0,73 mmol) and either 121 mg of terephthalic acid (0,73mmol) were dissolved in 38ml of DMF. For each sample 16AA, 32AA, 64AA, 100AA, 200AA we added a different amount of acetic acid: 0.7, 1.4, 2.8, 4,2 and 8,4 ml, respectively. All the samples were kept in a glass jar in the oven at 120°C for 24h. The resulted materials were collected by centrifugation, washed three times with DMF (3 x 30 ml) and solvent exchange with MeOH (3 x 30 ml) in three days. Finally, the solids were activated at 250°C overnight under dynamic vacuum ($\approx 10^{-3}$ mbar) and stored in a glovebox.

7.3.2.4 Synthesis of MOF-808

The synthesis procedure is: 960 mg $ZrOCl_2.8H_2O$ and 660 mg H_3BTC were diluted in 60 mL DMF and 60 DMF, respectively, and then both solutions are mixed. After that, 120 mL of FA was added into the solution. All the solutions were mixed and put in an oven at 100°C for seven days to produce M7. White powder will now be precipitated, and the remaining solution must be removed by centrifugation. Wash the separated white powder with 25 mL DMF and centrifuge again. DMF washing is performed 3-4 times per day for 2 days. The washing procedure was continued by replacing DMF with methanol for 4 times per day for 2 days. The washed powder was then dried in atmospheric condition and then activated at 100°C under vacuum overnight.

Another pristine MOF-808 (named M3) was synthesized following the similar procedure, however, the reaction time was reduced to 3 days in an oven at 100°C.

7.3.2.5 Synthesis of defective MOF-808

The reagents used in the synthesis of defective MOF-808 (MD) are similar to the production of pristine MOF-808. However, the stoichiometric molar ratio between zirconium salt and BTC is made to be 3:1. Typically, 970 mg $ZrOCl_2.8H_2O$ and 210 mg H_3BTC were diluted in 33 mL DMF and 20 DMF, respectively. After that, 45 mL of FA was added into the solution. All the solutions were mixed and put in an oven at 130°C for two days. The precipitated white powder is separated from the remaining solution. Wash the separated white powder with 25 mL DMF and centrifuge again. DMF washing is performed 3-4 times per day for 2 days. The washing procedure was continued by replacing DMF with methanol for 4 times per day for 2 days. The washed powder was then dried in atmospheric condition and then activated at 100°C under vacuum overnight.

7.3.2.6 Synthesis of Pt@MOF-808

The pristine MOF-808 and the defective MOF-808 synthesis procedure can both be used to produce this composite material. The only difference is the adding of a Pt NPs solution prior the insertion of the glass jar into the oven. In particular 60 mg Pt NPs powder was diluted in 8 mL DMF and then put the solution in the glass jar. Also the washing and activation procedure remain the same. STEM images of three different samples namely Pt@M7, Pt@MD and Pt@MOF-808 are shown below in order to prove the reproducibility of the

encapsulation method. The main difference is the quantity of Pt incorporated inside the crystals.

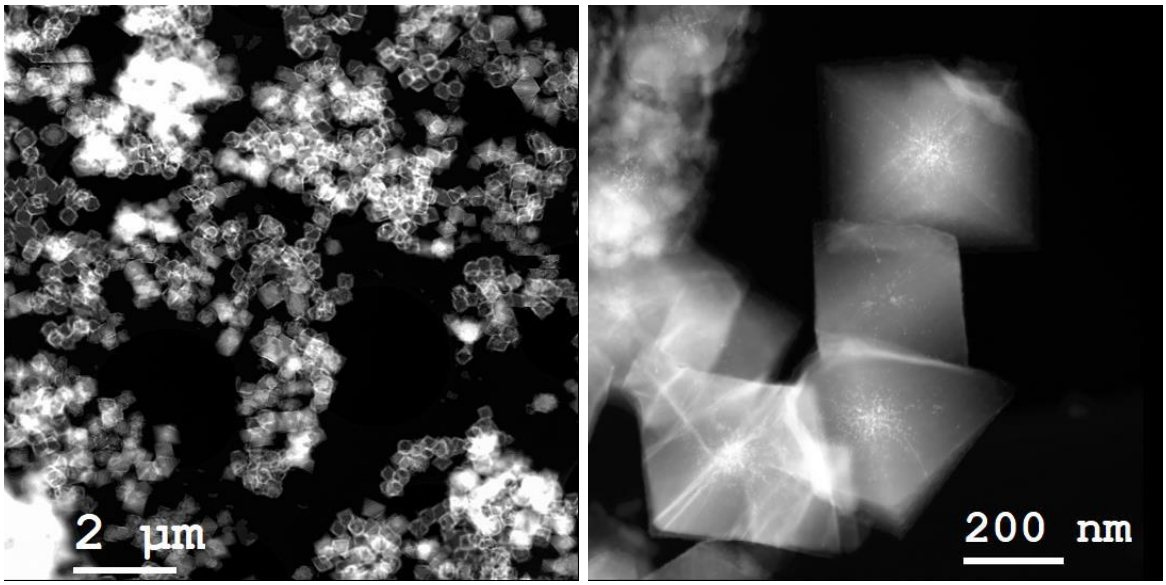

Figure 7.23: Left panel shows an overview STEM picture of the sample Pt@MD. Where the ratio between hollow crystals and filled crystals is 60/40 in favour of the hollow crystals. The red circle represent the area where the picture in the right panel was taken. Right panel shows a series of crystals with several Pt NPs in the center of the framework. The average size distribution of the Pt NPs after the encapsulation is 3.6 ± 0.7 nm meaning that only a partial agglomeration of Pt NPs is occurred during the solvothermal synthesis of MOF-808. Pt amount is 0.04 wt. % and was calculated via ICP measurement. Size distribution of the NPs were determined over 100 particles and measured with the software ImageJ.

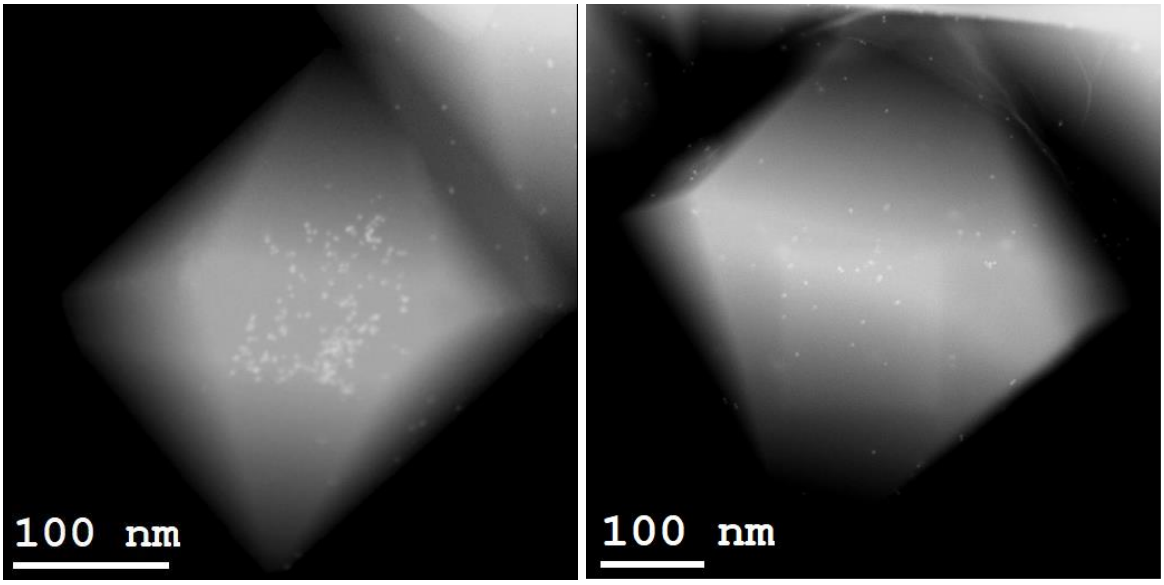

Figure 7.24: Left panel shows a STEM picture of the sample Pt@M7. Where the Pt NPs are mainly located in the center of the MOF-808 crystal. Right panel shows a STEM picture of a MOF-808 crystals with several Pt NPs randomly distributed on the framework. These two pictures are representative images of the sample

where the majority of the crystals have Pt NPS located in center of the framework. The average size distribution of the Pt NPs after the encapsulation is 3.5 ± 0.8 nm meaning that only a partial agglomeration of Pt NPs is occurred during the solvo-thermal synthesis of MOF-808. Pt amount is 0.1 wt. % and was calculated via ICP measurement. Size distribution of the NPs were determined over 100 particles and measured with the software ImageJ.

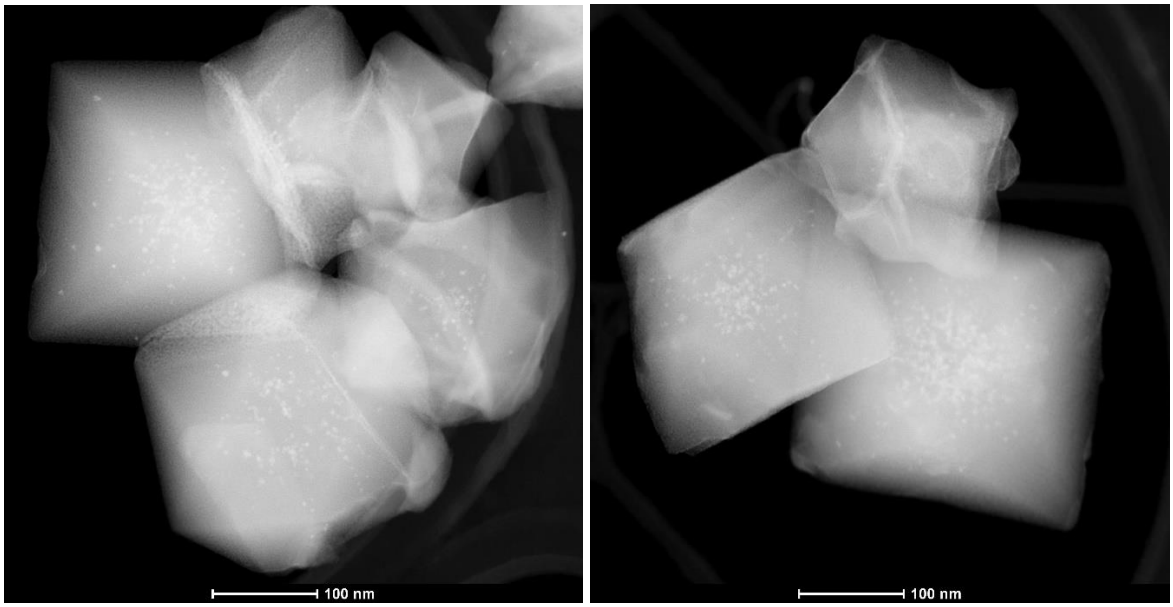

Figure 7.25: STEM pictures of the sample Pt@MOF-808. Where the Pt NPs are mainly located in the center of the MOF-808 crystal. These two pictures are representative images of the sample where the majority of the crystals have Pt NPS located in center of the framework with some of them located at the peripheries of the crystals. The average size distribution of the Pt NPs after the encapsulation is 3.5 ± 0.8 nm meaning that only a partial agglomeration of Pt NPs is occurred during the solvo-thermal synthesis of MOF-808. Pt amount is 0.8 wt. % and was calculated via ICP measurement. Size distribution of the NPs were determined over 100 particles and measured with the software ImageJ.

8 Reference

(1) Tilley, R. J. D., *Defects in Solids*. John Wiley and Sons: Weinheim, Germany, 2008.

(2) Tallon, J. L.; Bernhard, C.; Shaked, H.; Hitterman, R. L.; Jorgensen, J. D., *Phys. Rev. B* **1995,** *51* (18), 12911-12914.

(3) Fang, Z.; Bueken, B.; De Vos, D. E.; Fischer, R. A., *Angew. Chem. Int. Ed.* **2015,** *54* (25), 7234-7254.

(4) Callister, W. D.; Rethwisch, D. G., *Materials Science and Engineering An Introduction*. John Wiley and Sons New York, 2007.

(5) Yaghi, O. M.; Li, H., *J. Am. Chem. Soc.* **1995,** *117* (41), 10401-10402.

(6) Yaghi, O. M.; O'Keeffe, M.; Ockwig, N. W.; Chae, H. K.; Eddaoudi, M.; Kim, J., *Nature* **2003,** *423*, 705-714.

(7) Eddaoudi, M.; Kim, J.; Rosi, N.; Vodak, D.; Wachter, J.; O'Keeffe, M.; Yaghi, O. M., *Science* **2002,** *295* (5554), 469-472.

(8) Kim, H.; Yang, S.; Rao, S. R.; Narayanan, S.; Kapustin, E. A.; Furukawa, H.; Umans, A. S.; Yaghi, O. M.; Wang, E. N., *Science* **2017,** *356* (6336), 430-434.

(9) Jiang, J.; Zhao, Y.; Yaghi, O. M., *J. Am. Chem. Soc.* **2016,** *138* (10), 3255-3265.

(10) Zhou, J.; Li, R.; Fan, X.; Chen, Y.; Han, R.; Li, W.; Zheng, J.; Wang, B.; Li, X., *Energy Environ. Sci.* **2014,** *7* (8), 2715-2724.

(11) Li, J.-R.; Sculley, J.; Zhou, H.-C., *Chem. Rev.* **2012,** *112* (2), 869-932.

(12) Zhu, L.; Liu, X.-Q.; Jiang, H.-L.; Sun, L.-B., *Chem. Rev.* **2017,** *117* (12), 8129-8176.

(13) Epp, K.; Semrau, A. L.; Cokoja, M.; Fischer, R. A., *ChemCatChem 0* (0).

(14) Mautschke, H. H.; Drache, F.; Senkovska, I.; Kaskel, S.; Llabrés i Xamena, F. X., *Catal. Sci. Technol* **2018,** *8* (14), 3610-3616.

(15) DeCoste, J. B.; Peterson, G. W., *Chem. Rev.* **2014,** *114* (11), 5695-5727.

(16) Horcajada, P.; Serre, C.; Vallet-Regí, M.; Sebban, M.; Taulelle, F.; Férey, G., *Angew. Chem. Int. Ed.* **2006,** *45* (36), 5974-5978.

(17) Wharmby, M. T.; Henke, S.; Bennett, T. D.; Bajpe, S. R.; Schwedler, I.; Thompson, S. P.; Gozzo, F.; Simoncic, P.; Mellot-Draznieks, C.; Tao, H.; Yue, Y.; Cheetham, A. K., *Angew. Chem. Int. Ed.* **2015,** *54* (22), 6447-6451.

(18) Coudert, F.-X., *Chem. Mater.* **2015,** *27* (6), 1905-1916.

(19) Loiseau, T.; Serre, C.; Huguenard, C.; Fink, G.; Taulelle, F.; Henry, M.; Bataille, T.; Férey, G., *Chem. Eur. J* **2004,** *10* (6), 1373-1382.

(20) Henke, S.; Schmid, R.; Grunwaldt, J.-D.; Fischer, R. A., *Chem. Eur. J* **2010,** *16* (48), 14296-14306.

(21) Bosch, M.; Zhang, M.; Zhou, H.-C., *Adv. Chem.* **2014,** *2014*, 8.

(22) Cavka, J. H.; Jakobsen, S.; Olsbye, U.; Guillou, N.; Lamberti, C.; Bordiga, S.; Lillerud, K. P., *J. Am. Chem. Soc.* **2008,** *130* (42), 13850-13851.

(23) Valenzano, L.; Civalleri, B.; Chavan, S.; Bordiga, S.; Nilsen, M. H.; Jakobsen, S.; Lillerud, K. P.; Lamberti, C., *Chem. Mater.* **2011,** *23* (7), 1700-1718.

(24) Shearer, G. C.; Forselv, S.; Chavan, S.; Bordiga, S.; Mathisen, K.; Bjørgen, M.; Svelle, S.; Lillerud, K. P., *Top. Catal.* **2013,** *56* (9), 770-782.

(25) Shearer, G. C.; Chavan, S.; Ethiraj, J.; Vitillo, J. G.; Svelle, S.; Olsbye, U.; Lamberti, C.; Bordiga, S.; Lillerud, K. P., *Chem. Mater.* **2014,** *26* (14), 4068-4071.

(26) Wiersum, A. D.; Soubeyrand-Lenoir, E.; Yang, Q.; Moulin, B.; Guillerm, V.; Yahia, M. B.; Bourrelly, S.; Vimont, A.; Miller, S.; Vagner, C.; Daturi, M.; Clet, G.; Serre, C.; Maurin, G.; Llewellyn, P. L., *Chem. Asian J.* **2011,** *6* (12), 3270-3280.

(27) Bai, Y.; Dou, Y.; Xie, L.-H.; Rutledge, W.; Li, J.-R.; Zhou, H.-C., *Chem. Soc. Rev.* **2016,** *45* (8), 2327-2367.

(28) Bon, V.; Senkovskyy, V.; Senkovska, I.; Kaskel, S., *ChemComm.* **2012,** *48* (67), 8407-8409.

(29) Feng, D.; Gu, Z.-Y.; Li, J.-R.; Jiang, H.-L.; Wei, Z.; Zhou, H.-C., *Angew. Chem. Int. Ed.* **2012,** *51* (41), 10307-10310.

(30) Mondloch, J. E.; Bury, W.; Fairen-Jimenez, D.; Kwon, S.; DeMarco, E. J.; Weston, M. H.; Sarjeant, A. A.; Nguyen, S. T.; Stair, P. C.; Snurr, R. Q.; Farha, O. K.; Hupp, J. T., *J. Am. Chem. Soc.* **2013,** *135* (28), 10294-10297.

(31) Furukawa, H.; Gándara, F.; Zhang, Y.-B.; Jiang, J.; Queen, W. L.; Hudson, M. R.; Yaghi, O. M., *J. Am. Chem. Soc.* **2014,** *136* (11), 4369-4381.

(32) Li, P.; Klet, R. C.; Moon, S.-Y.; Wang, T. C.; Deria, P.; Peters, A. W.; Klahr, B. M.; Park, H.-J.; Al-Juaid, S. S.; Hupp, J. T.; Farha, O. K., *ChemComm.* **2015,** *51* (54), 10925-10928.

(33) Canivet, J.; Aguado, S.; Schuurman, Y.; Farrusseng, D., *J. Am. Chem. Soc.* **2013,** *135* (11), 4195-4198.

(34) Dissegna, S.; Hardian, R.; Epp, K.; Kieslich, G.; Coulet, M.-V.; Llewellyn, P.; Fischer, R. A., *CrystEngComm.* **2017,** *19*, 4137-4141.

(35) Plessers, E.; Fu, G.; Tan, C.; De Vos, D.; Roeffaers, M., *Catalysts* **2016,** *6* (7), 104.

(36) Schlögl, R., *Angew. Chem. Int. Ed.* **2015,** *54* (11), 3465-3520.

(37) Xia, Q.; Li, Z.; Tan, C.; Liu, Y.; Gong, W.; Cui, Y., *J. Am. Chem. Soc.* **2017,** *139* (24), 8259-8266.

(38) Islamoglu, T.; Goswami, S.; Li, Z.; Howarth, A. J.; Farha, O. K.; Hupp, J. T., *Acc. Chem. Res.* **2017,** *50* (4), 805-813.

(39) Rogge, S. M. J.; Wieme, J.; Vanduyfhuys, L.; Vandenbrande, S.; Maurin, G.; Verstraelen, T.; Waroquier, M.; Van Speybroeck, V., *Chem. Mater.* **2016,** *28* (16), 5721-5732.

(40) Dissegna, S.; Epp, K.; Heinz, W. R.; Kieslich, G.; Fischer, R. A., *Adv. Mater.* **2018,** *0* (0), 1704501.

(41) Ravon, U.; Savonnet, M.; Aguado, S.; Domine, M. E.; Janneau, E.; Farrusseng, D., *Microporous Mesoporous Mater.* **2010,** *129* (3), 319-329.

(42) Shearer, G. C.; Chavan, S.; Bordiga, S.; Svelle, S.; Olsbye, U.; Lillerud, K. P., *Chem. Mater.* **2016,** *28* (11), 3749-3761.

(43) Kozachuk, O.; Luz, I.; Llabrés i Xamena, F. X.; Noei, H.; Kauer, M.; Albada, H. B.; Bloch, E. D.; Marler, B.; Wang, Y.; Muhler, M.; Fischer, R. A., *Angew. Chem. Int. Ed.* **2014,** *53* (27), 7058-7062.

(44) Vermoortele, F.; Bueken, B.; Le Bars, G.; Van de Voorde, B.; Vandichel, M.; Houthoofd, K.; Vimont, A.; Daturi, M.; Waroquier, M.; Van Speybroeck, V.; Kirschhock, C.; De Vos, D. E., *J. Am. Chem. Soc.* **2013,** *135* (31), 11465-11468.

(45) Marx, S.; Kleist, W.; Baiker, A., *J. Catal.* **2011,** *281* (1), 76-87.

(46) Llabrés i Xamena, F. X.; Cirujano, F. G.; Corma, A., *Microporous Mesoporous Mater.* **2012,** *157*, 112-117.

(47) Vermoortele, F.; Ameloot, R.; Alaerts, L.; Matthessen, R.; Carlier, B.; Fernandez, E. V. R.; Gascon, J.; Kapteijn, F.; De Vos, D. E., *J. Mater. Chem.* **2012,** *22* (20), 10313-10321.

(48) Marshall, R. J.; Forgan, R. S., *Eur. J. Inorg. Chem.* **2016,** *2016* (27), 4310-4331.

(49) Karagiaridi, O.; Lalonde, M. B.; Bury, W.; Sarjeant, A. A.; Farha, O. K.; Hupp, J. T., *J. Am. Chem. Soc.* **2012,** *134* (45), 18790-18796.

(50) Karagiaridi, O.; Vermeulen, N. A.; Klet, R. C.; Wang, T. C.; Moghadam, P. Z.; Al-Juaid, S. S.; Stoddart, J. F.; Hupp, J. T.; Farha, O. K., *Inorg. Chem.* **2015,** *54* (4), 1785-1790.

(51) Jiang, J.-Q.; Yang, C.-X.; Yan, X.-P., *ChemComm.* **2015,** *51* (30), 6540-6543.

(52) Lee, S. J.; Doussot, C.; Baux, A.; Liu, L.; Jameson, G. B.; Richardson, C.; Pak, J. J.; Trousselet, F.; Coudert, F.-X.; Telfer, S. G., *Chem. Mater.* **2016,** *28* (1), 368-375.

(53) Deria, P.; Mondloch, J. E.; Tylianakis, E.; Ghosh, P.; Bury, W.; Snurr, R. Q.; Hupp, J. T.; Farha, O. K., *J. Am. Chem. Soc.* **2013,** *135* (45), 16801-16804.

(54) Gadipelli, S.; Guo, Z., *Chem. Mater.* **2014,** *26* (22), 6333-6338.

(55) Bennett, T. D.; Todorova, T. K.; Baxter, E. F.; Reid, D. G.; Gervais, C.; Bueken, B.; Van de Voorde, B.; De Vos, D.; Keen, D. A.; Mellot-Draznieks, C., *Phys. Chem. Chem. Phys.* **2016,** *18* (3), 2192-201.

(56) Thornton, A. W.; Babarao, R.; Jain, A.; Trousselet, F.; Coudert, F. X., *Dalton Trans.* **2016,** *45* (10), 4352-4359.

(57) Dürholt, J. P.; Julian, K.; Rochus, S., *Eur. J. Inorg. Chem.* **2016,** *2016* (27), 4517-4523.

(58) Semino, R.; Ramsahye, N. A.; Ghoufi, A.; Maurin, G., *Microporous Mesoporous Mater.* **2017,** *254*, 184-191.

(59) Mondal, S. S.; Dey, S.; Attallah, A. G.; Krause-Rehberg, R.; Janiak, C.; Holdt, H.-J., *Dalton Trans.* **2017,** *46* (14), 4824-4833.

(60) Mondal, S. S.; Dey, S.; Attallah, A. G.; Bhunia, A.; Kelling, A.; Schilde, U.; Krause-Rehberg, R.; Janiak, C.; Holdt, H.-J., *ChemistrySelect* **2016,** *1* (14), 4320-4325.

(61) Klet, R. C.; Liu, Y.; Wang, T. C.; Hupp, J. T.; Farha, O. K., *J. Mater. Chem. A* **2016,** *4* (4), 1479-1485.

(62) Liu, M.; Wong-Foy, A. G.; Vallery, R. S.; Frieze, W. E.; Schnobrich, J. K.; Gidley, D. W.; Matzger, A. J., *Adv. Mater.* **2010,** *22* (14), 1598-1601.

(63) Liu, Y.; Klet, R. C.; Hupp, J. T.; Farha, O., *ChemComm.* **2016,** *52* (50), 7806-7809.

(64) Mendt, M.; Gutt, F.; Kavoosi, N.; Bon, V.; Senkovska, I.; Kaskel, S.; Pöppl, A., *J. Phys. Chem. C* **2016,** *120* (26), 14246-14259.

(65) Lu, A. X.; McEntee, M.; Browe, M. A.; Hall, M. G.; DeCoste, J. B.; Peterson, G. W., *ACS Appl. Mater. Interfaces* **2017,** *9* (15), 13632-13636.

(66) Plonka, A. M.; Wang, Q.; Gordon, W. O.; Balboa, A.; Troya, D.; Guo, W.; Sharp, C. H.; Senanayake, S. D.; Morris, J. R.; Hill, C. L.; Frenkel, A. I., *J. Am. Chem. Soc.* **2017,** *139* (2), 599-602.

(67) Li, B.; Zhu, X.; Hu, K.; Li, Y.; Feng, J.; Shi, J.; Gu, J., *J. Hazard. Mater.* **2016,** *302*, 57-64.

(68) Fan, K.; Nie, W.-X.; Wang, L.-P.; Liao, C.-H.; Bao, S.-S.; Zheng, L.-M., *Chem. Eur. J* **2017,** *23* (27), 6615-6624.

(69) Fernandez, C. A.; Nune, S. K.; Annapureddy, H. V.; Dang, L. X.; McGrail, B. P.; Zheng, F.; Polikarpov, E.; King, D. L.; Freeman, C.; Brooks, K. P., *Dalton Trans.* **2015,** *44* (30), 13490-13497.

(70) Stassen, I.; Burtch, N.; Talin, A.; Falcaro, P.; Allendorf, M.; Ameloot, R., *Chem. Soc. Rev.* **2017,** *46* (11), 3185-3241.

(71) Sun, L.; Campbell, M. G.; Dincă, M., *Angew. Chem. Int. Ed.* **2016,** *55* (11), 3566-3579.

(72) Zhang, W.; Kauer, M.; Halbherr, O.; Epp, K.; Guo, P.; Gonzalez, M. I.; Xiao, D. J.; Wiktor, C.; Liabrés i Xamena, F. X.; Wöll, C.; Wang, Y.; Muhler, M.; Fischer, R. A., *Chem. Eur. J* **2016,** *22* (40), 14297-14307.

(73) Cirujano, F. G.; Corma, A.; Llabrés i Xamena, F. X., *Chem. Eng. Sci.* **2015,** *124*, 52-60.

(74) Szilágyi, P. Á.; Serra-Crespo, P.; Gascon, J.; Geerlings, H.; Dam, B., *Front. Energy* **2016,** *4* (9).

(75) Behrens, K.; Mondal, S. S.; Nöske, R.; Baburin, I. A.; Leoni, S.; Günter, C.; Weber, J.; Holdt, H.-J., *Inorg. Chem.* **2015,** *54* (20), 10073-10080.

(76) Cortinas, I.; Field, J. A.; Kopplin, M.; Garbarino, J. R.; Gandolfi, A. J.; Sierra-Alvarez, R., *Environ. Sci. Technol.* **2006,** *40* (9), 2951-2957.

(77) Rösler, C.; Fischer, R. A., *CrystEngComm.* **2015,** *17* (2), 199-217.

(78) Corma, A.; García, H.; Llabrés i Xamena, F. X., *Chem. Rev.* **2010,** *110* (8), 4606-4655.

(79) Kitagawa, S.; Kitaura, R.; Noro, S.-i., *Angew. Chem. Int. Ed.* **2004,** *43* (18), 2334-2375.

(80) Nasalevich, M. A.; Van der Veen, M.; Kapteijn, F.; Gascon, J., *CrystEngComm.* **2014,** *16* (23), 4919-4926.

(81) Vandichel, M.; Hajek, J.; Vermoortele, F.; Waroquier, M.; De Vos, D. E.; Van Speybroeck, V., *CrystEngComm.* **2015,** *17* (2), 395-406.

(82) Lu, W.; Wei, Z.; Gu, Z.-Y.; Liu, T.-F.; Park, J.; Park, J.; Tian, J.; Zhang, M.; Zhang, Q.; Gentle Iii, T.; Bosch, M.; Zhou, H.-C., *Chem. Soc. Rev.* **2014,** *43* (16), 5561-5593.

(83) Kandiah, M.; Nilsen, M. H.; Usseglio, S.; Jakobsen, S.; Olsbye, U.; Tilset, M.; Larabi, C.; Quadrelli, E. A.; Bonino, F.; Lillerud, K. P., *Chem. Mater.* **2010,** *22* (24), 6632-6640.

(84) DeCoste, J. B.; Peterson, G. W.; Jasuja, H.; Glover, T. G.; Huang, Y.-g.; Walton, K. S., *J. Mater. Chem. A* **2013,** *1* (18), 5642-5650.

(85) Fang, Z.; Dürholt, J. P.; Kauer, M.; Zhang, W.; Lochenie, C.; Jee, B.; Albada, B.; Metzler-Nolte, N.; Pöppl, A.; Weber, B.; Muhler, M.; Wang, Y.; Schmid, R.; Fischer, R. A., *J. Am. Chem. Soc.* **2014,** *136* (27), 9627-9636.

(86) Vermoortele, F.; Vandichel, M.; Van de Voorde, B.; Ameloot, R.; Waroquier, M.; Van Speybroeck, V.; De Vos, D. E., *Angew. Chem. Int. Ed.* **2012,** *51* (20), 4887-4890.

(87) Canivet, J.; Vandichel, M.; Farrusseng, D., *Dalton Trans.* **2016,** *45* (10), 4090-4099.

(88) Rasero-Almansa, A. M.; Corma, A.; Iglesias, M.; Sánchez, F., *Green Chem.* **2014,** *16* (7), 3522-3527.

(89) Wu, H.; Chua, Y. S.; Krungleviciute, V.; Tyagi, M.; Chen, P.; Yildirim, T.; Zhou, W., *J. Am. Chem. Soc.* **2013,** *135* (28), 10525-10532.

(90) Rouquerol, F.; Rouquerol, J.; Sing, K. S. W., *Adsorption by powders and porous solids: Principles, Methodology and Applications*. Academic Press: London, UK, 1999.

(91) Canivet, J.; Bonnefoy, J.; Daniel, C.; Legrand, A.; Coasne, B.; Farrusseng, D., *New J. Chem.* **2014,** *38* (7), 3102-3111.

(92) Jeremias, F.; Lozan, V.; Henninger, S. K.; Janiak, C., *Dalton Trans.* **2013,** *42* (45), 15967-15973.

(93) Ghosh, P.; Colon, Y. J.; Snurr, R. Q., *ChemComm.* **2014,** *50* (77), 11329-11331.

(94) Jasuja, H.; Walton, K. S., *J. Phys. Chem. C* **2013,** *117* (14), 7062-7068.

(95) Schoenecker, P. M.; Carson, C. G.; Jasuja, H.; Flemming, C. J. J.; Walton, K. S., *Ind. Eng. Chem. Res.* **2012,** *51* (18), 6513-6519.

(96) Ling, S.; Slater, B., *Chem. Sci.* **2016,** *7* (7), 4706-4712.

(97) Trickett, C. A.; Gagnon, K. J.; Lee, S.; Gándara, F.; Bürgi, H.-B.; Yaghi, O. M., *Angew. Chem. Int. Ed.* **2015,** *54* (38), 11162-11167.

(98) de Oliveira, A.; Mavrandonakis, A.; de Lima, G. F.; De Abreu, H. A., *ChemistrySelect* **2017,** *2* (26), 7813-7820.

(99) Busch, G., *Eur. J. Phys.* **1989,** *10* (4), 254.

(100) Rimoldi, M.; Howarth, A. J.; DeStefano, M. R.; Lin, L.; Goswami, S.; Li, P.; Hupp, J. T.; Farha, O. K., *ACS Catal.* **2017,** *7* (2), 997-1014.

(101) Kreno, L. E.; Leong, K.; Farha, O. K.; Allendorf, M.; Van Duyne, R. P.; Hupp, J. T., *Chem. Rev.* **2012,** *112* (2), 1105-1125.

(102) Zhang, Y.; Yuan, S.; Feng, X.; Li, H.; Zhou, J.; Wang, B., *J. Am. Chem. Soc.* **2016,** *138* (18), 5785-5788.

(103) Rieth, A. J.; Yang, S.; Wang, E. N.; Dincă, M., *ACS Cent. Sci.* **2017,** *3* (6), 668-672.

(104) Cliffe, M. J.; Hill, J. A.; Murray, C. A.; Coudert, F.-X.; Goodwin, A. L., *Phys. Chem. Chem. Phys.* **2015,** *17* (17), 11586-11592.

(105) Bennett, T. D.; Cheetham, A. K., *Acc. Chem. Res.* **2014,** *47* (5), 1555-1562.

(106) Thornton, A. W.; Jelfs, K. E.; Konstas, K.; Doherty, C. M.; Hill, A. J.; Cheetham, A. K.; Bennett, T. D., *ChemComm.* **2016,** *52* (19), 3750-3753.

(107) Cliffe, M. J.; Wan, W.; Zou, X.; Chater, P. A.; Kleppe, A. K.; Tucker, M. G.; Wilhelm, H.; Funnell, N. P.; Coudert, F.-X.; Goodwin, A. L., *Nat. Commun.* **2014,** *5*, 4176.

(108) Tan, J. C.; Cheetham, A. K., *Chem. Soc. Rev.* **2011,** *40* (2), 1059-1080.

(109) McKellar, S. C.; Moggach, S. A., *Acta Crystallogr. B* **2015,** *71* (6), 587-607.

(110) Yot, P. G.; Vanduyfhuys, L.; Alvarez, E.; Rodriguez, J.; Itie, J.-P.; Fabry, P.; Guillou, N.; Devic, T.; Beurroies, I.; Llewellyn, P. L.; Van Speybroeck, V.; Serre, C.; Maurin, G., *Chem. Sci.* **2016,** *7* (1), 446-450.

(111) Henke, S.; Wharmby, M. T.; Kieslich, G.; Hante, I.; Schneemann, A.; Wu, Y.; Daisenberger, D.; Cheetham, A. K., *Chem. Sci.* **2018,** *9* (6), 1654-1660.

(112) Ferey, G.; Serre, C., *Chem. Soc. Rev.* **2009,** *38* (5), 1380-1399.

(113) Hu, Y. H.; Zhang, L., *Phys. Rev. B* **2010,** *81* (17), 174103.

(114) Chapman, K. W.; Halder, G. J.; Chupas, P. J., *J. Am. Chem. Soc.* **2009,** *131* (48), 17546-17547.

(115) Gascon, J.; Corma, A.; Kapteijn, F.; Llabrés i Xamena, F. X., *ACS Catal.* **2014,** *4* (2), 361-378.

(116) Coudert, F.-X.; Fuchs, A. H., *Coordin. Chem. Rev.* **2016,** *307, Part 2*, 211-236.

(117) Sarkisov, L., *Dalton Trans.* **2016,** *45* (10), 4203-4212.

(118) Brooks, N. J.; Gauthe, B. L.; Terrill, N. J.; Rogers, S. E.; Templer, R. H.; Ces, O.; Seddon, J. M., *Rev. Sci. Instrum.* **2010,** *81* (6), 064103.

(119) Hobday, C. L.; Marshall, R. J.; Murphie, C. F.; Sotelo, J.; Richards, T.; Allan, D. R.; Düren, T.; Coudert, F. X.; Forgan, R. S.; Morrison, C. A.; Moggach, S. A.; Bennett, T. D., *Angew. Chem. Int. Ed.* **2016,** *55* (7), 2401-2405.

(120) Birch, F., *Phys. Rev.* **1947,** *71* (11), 809-824.

(121) Yot, P. G.; Yang, K.; Ragon, F.; Dmitriev, V.; Devic, T.; Horcajada, P.; Serre, C.; Maurin, G., *Dalton Trans.* **2016,** *45* (10), 4283-4288.

(122) Chapman, K. W.; Halder, G. J.; Chupas, P. J., *J. Am. Chem. Soc.* **2008,** *130* (32), 10524-10526.

(123) Yang, K.; Zhou, G.; Xu, Q., *RSC Adv.* **2016,** *6* (44), 37506-37514.

(124) Jaffe, A.; Lin, Y.; Beavers, C. M.; Voss, J.; Mao, W. L.; Karunadasa, H. I., *ACS Cent. Sci.* **2016,** *2* (4), 201-209.

(125) Kieslich, G.; Forse, A. C.; Sun, S.; Butler, K. T.; Kumagai, S.; Wu, Y.; Warren, M. R.; Walsh, A.; Grey, C. P.; Cheetham, A. K., *Chem. Mater.* **2016,** *28* (1), 312-317.

(126) Ardila-Suárez, C.; Perez-Beltran, S.; Ramírez-Caballero, G. E.; Balbuena, P. B., *Catal. Sci. Technol* **2018,** *8* (3), 847-857.

(127) Wang, T. C.; Vermeulen, N. A.; Kim, I. S.; Martinson, A. B. F.; Stoddart, J. F.; Hupp, J. T.; Farha, O. K., *Nat. Protoc.* **2015,** *11*, 149.

(128) Moon, S.-Y.; Liu, Y.; Hupp, J. T.; Farha, O. K., *Angew. Chem. Int. Ed.* **2015,** *54* (23), 6795-6799.

(129) Huang, Y.-B.; Liang, J.; Wang, X.-S.; Cao, R., *Chem. Soc. Rev.* **2017,** *46* (1), 126-157.

(130) Cirujano, F. G.; Llabrés i Xamena, F. X.; Corma, A., *Dalton Trans.* **2012,** *41* (14), 4249-4254.

(131) Li, X.; Guo, Z.; Xiao, C.; Goh, T. W.; Tesfagaber, D.; Huang, W., *ACS Catal.* **2014,** *4* (10), 3490-3497.

(132) Jiang, J.; Gándara, F.; Zhang, Y.-B.; Na, K.; Yaghi, O. M.; Klemperer, W. G., *J. Am. Chem. Soc.* **2014,** *136* (37), 12844-12847.

(133) Healey, K.; Liang, W.; Southon, P. D.; Church, T. L.; D'Alessandro, D. M., *J. Mater. Chem. A* **2016,** *4* (28), 10816-10819.

(134) Ji, W.; Qi, W.; Tang, S.; Peng, H.; Li, S., *Nanomaterials* **2015,** *5* (4), 2203.

(135) Teranishi, T.; Hosoe, M.; Tanaka, T.; Miyake, M., *J. Phys. Chem. B* **1999,** *103* (19), 3818-3827.

(136) Rösler, C.; Aijaz, A.; Turner, S.; Filippousi, M.; Shahabi, A.; Xia, W.; Van Tendeloo, G.; Muhler, M.; Fischer, R. A., *Chem. Eur. J* **2016,** *22* (10), 3304-3311.

(137) Chatterji, T.; Hansen, T. C.; Brunelli, M.; Henry, P. F., *Appl. Phys. Lett.* **2009,** *94* (24), 241902.

(138) Greve, B. K.; Martin, K. L.; Lee, P. L.; Chupas, P. J.; Chapman, K. W.; Wilkinson, A. P., *J. Am. Chem. Soc.* **2010,** *132* (44), 15496-15498.

(139) Goodwin, A. L.; Chapman, K. W.; Kepert, C. J., *J. Am. Chem. Soc.* **2005,** *127* (51), 17980-17981.

(140) Chapman, K. W.; Chupas, P. J.; Kepert, C. J., *J. Am. Chem. Soc.* **2006,** *128* (21), 7009-7014.

(141) Martinek, C.; Hummel, F. A., *J. Am. Ceram. Soc.* **1968,** *51* (4), 227-228.

(142) Miller, W.; Smith, C. W.; Mackenzie, D. S.; Evans, K. E., *J. Mater. Sci.* **2009,** *44* (20), 5441-5451.

(143) Wu, Y.; Kobayashi, A.; Halder, G. J.; Peterson, V. K.; Chapman, K. W.; Lock, N.; Southon, P. D.; Kepert, C. J., *Angew. Chem. Int. Ed.* **2008,** *47* (46), 8929-8932.

(144) Bu, Y.; Chang, Z.; Du, J.; Liu, D., *RSC Adv.* **2017,** *7* (46), 29240-29254.

(145) Alabarse, F. G.; Silly, G.; Brubach, J.-B.; Roy, P.; Haidoux, A.; Levelut, C.; Bantignies, J.-L.; Kohara, S.; Le Floch, S.; Cambon, O.; Haines, J., *J. Phys. Chem. C* **2017,** *121* (12), 6852-6863.

(146) Liu, H.; A. Secco, R.; Huang, Y., *PhysChemComm* **2001,** *4* (8), 37-39.

(147) Chan Hwang, G.; Joo Shin, T.; Blom, D. A.; Vogt, T.; Lee, Y., *Sci. Rep.* **2015,** *5*, 15056.

(148) Alabarse, F. G.; Brubach, J.-B.; Roy, P.; Haidoux, A.; Levelut, C.; Bantignies, J.-L.; Cambon, O.; Haines, J., *J. Phys. Chem. C* **2015,** *119* (14), 7771-7779.

(149) Alabarse, F. G.; Silly, G.; Haidoux, A.; Levelut, C.; Bourgogne, D.; Flank, A.-M.; Lagarde, P.; Pereira, A. S.; Bantignies, J.-L.; Cambon, O.; Haines, J., *J. Phys. Chem. C* **2014,** *118* (7), 3651-3663.

(150) Betti, C.; Fois, E.; Mazzucato, E.; Medici, C.; Quartieri, S.; Tabacchi, G.; Vezzalini, G.; Dmitriev, V., *Microporous Mesoporous Mater.* **2007,** *103* (1), 190-209.

(151) Li, S.; Huo, F., *Small* **2014,** *10* (21), 4371-4378.

9 Appendix

9.1 List of Publications

Peer-reviewed journal publications on which this thesis is based:

1. Dissegna, S.; Epp, K.; Heinz, W. R.; Kieslich, G.; Fischer, R. A., *Adv. Mater.* **2018**, 0 (0), 1704501. (Selected for the inside back cover of the journal issue)
Title: "Defective Metal-Organic Frameworks"

2. Dissegna, S.; Hardian, R.; Epp, K.; Kieslich, G.; Coulet, M.-V.; Llewellyn, P.; Fischer, R. A., *CrystEngComm* **2017**, 19 (29), 4137-4141. (Selected for the front-cover of the journal issue)
Title: "Using water adsorption measurements to access the chemistry of defects in the metal–organic framework UiO-66"[¥]

[¥] SD contribution on this work was the synthesis and characterization and data interpretations of all materials. The catalytic testing was performed by Konstantin Epp and water adsorption measurement and subsequent analysis were performed by Rifan Hardian in the context of the European project DEFNET.

3. Dissegna, S.; Vervoorts, P.; Hobday, C. L.; Düren, T.; Daisenberger, D.; Fischer, Roland A.; Kieslich, G., *J. Am. Chem. Soc.* **2018**, 140 (37), 11581- 11584.
Title: "Tuning the mechanical response of defective metal-organic frameworks" [§]

[§]SD contribution on this work was the synthesis, characterization and data interpretation of all samples. Pia Vervoorts and Claire Hobday performed the experiments at Diamond Light Source synchrotron under the supervision of Dr. Gregor Kieslich.

Manuscript in preparation:

4. Hardian, R.; Dissegna, S.; Schäfer, M.; Ullrich A.; Coulet, M-V.; Henning A. Höppe, Fischer, Roland. A.; Llewellyn, Philip L., *Chem. Eur. J.*, **2018**, manuscript in preparation.

Peer-reviewed journal publications outside the scope of this thesis:

5. Rösler, C.; Dissegna, S.; Rechac, V. L.; Kauer, M.; Guo, P.; Turner, S.; Ollegott, K.; Kobayashi, H.; Yamamoto, T.; Peeters, D.; Wang, Y.; Matsumura, S.; Van Tendeloo, G.; Kitagawa, H.; Muhler, M.; Llabrés i Xamena, F. X.; Fischer, R. A., *Chem. Eur. J.* **2017**, 23 (15). (Selected for the front cover of the journal issue)

9.2 List of selected presentations

Proper reports on the topic of this thesis were presented at the following workshops, symposium or conferences:

1. Dissegna, S.; Fischer, R. A.

DEFNET Workshop 3, University of Ghent, Ghent, Belgium, **March 2016** (poster presentation)

2. Dissegna, S.; Rösler, C.; Rechac, V. L.; Kauer, M.; Guo, P.; Turner, S.; Ollegott, K.; Kobayashi, H.; Yamamoto, T.; Peeters, D.; Wang, Y.; Matsumura, S.; Van Tendeloo, G.; Kitagawa, H.; Muhler, M.; Llabrés i Xamena, F. X.; Fischer, R. A.

4th International Conference on Metal –Organic Frameworks & Open Framework Compounds, Long Beach, California, USA, **September 2016**. (poster presentation)

3. Dissegna, S.; Fischer, R. A.

Summer school within the European project named DEFNET, Universitat Politecnica de Valencia, Istituto de tecnologia Quimica (ITQ), Valencia, Spain, **June 2016**. (oral presentation)

4. Dissegna, S.; Fischer, R. A.

Group Seminar, Instituto de Tecnologia Quimica (ITQ), Univeristat Politecnica de Valencia. Valencia, Spain, **October 2016**. (oral presentation)

5. Dissegna, S.; Fischer, R. A.

DEFNET Workshop 5, Aix-Marseille University, Saint Jerome Campus, Marseille, France, **November 2016**. (oral presentation

“A l'alta fantasia qui mancò possa;
ma già volgeva il mio disio e 'l velle,
sì come rota ch'igualmente è mossa,

l'amor che move il sole e l'altre stele.”

Dante Alighieri, Divina Commedia, Canto XXXIII, Paradiso